



TECHNISCHE  
UNIVERSITÄT  
WIEN

Vienna University of Technology

---

Unterschrift des Betreuers

DIPLOMARBEIT  
Performance Studies on Stacked Silicon  
Strip Sensors

ausgeführt am

Institut für Hochenergiephysik  
der Österreichischen Akademie der Wissenschaften

und am

Atominstitut der Österreichischen Universitäten

unter Anleitung von

Univ.Doz. Dipl.-Ing. Dr.techn. Manfred KRAMMER

durch

Erik Huemer

Matrikelnummer: 0147029

Kaiserstr. 8/18

1070 Wien

Wien, am 1. September 2013

---

Unterschrift



# Contents

<b>1. Introduction</b>	<b>1</b>
<b>2. The LHC and the CMS Experiment</b>	<b>3</b>
2.1. Physics Objectives . . . . .	3
2.1.1. The Standard Model (SM) . . . . .	3
2.1.2. The LHC Goals . . . . .	4
2.2. The Large Hadron Collider (LHC) . . . . .	5
2.2.1. Introduction . . . . .	5
2.2.2. Technical Design Features . . . . .	6
2.3. The Compact Muon Solenoid (CMS) . . . . .	8
2.3.1. Detector Specifications . . . . .	9
2.3.2. Detector Design . . . . .	10
2.3.3. The Tracking System . . . . .	11
2.3.4. The Calorimeter System . . . . .	13
2.3.5. The Magnet System . . . . .	15
2.3.6. The Muon System . . . . .	16
2.3.7. The Trigger System . . . . .	17
<b>3. Plans for the Upgrade of the CMS Experiment</b>	<b>19</b>
3.1. Physics Motivations for an Upgrade . . . . .	19
3.2. The High-Luminosity LHC (HL-LHC) . . . . .	20
3.2.1. sLHC-PP (Phase 1) - Ultimate Luminosity . . . . .	21
3.2.2. HiLumi LHC (Phase 2) - Beyond Ultimate Luminosity . . . . .	21
3.3. The CMS Upgrade . . . . .	23
3.3.1. Phase 1 . . . . .	23
3.3.2. Phase 2 . . . . .	24
3.3.3. The Phase 2 Tracker System - Track-Trigger modules . . . . .	25
<b>4. The Silicon Strip Detector</b>	<b>29</b>
4.1. Charged Particles in Matter . . . . .	29
4.1.1. Light Particles - Electrons and Positrons . . . . .	29
4.1.2. Other Particles . . . . .	29
4.1.3. Energy Loss Distribution . . . . .	30
4.2. Construction of Silicon Strip Detectors . . . . .	33
4.2.1. Working Principle . . . . .	33
4.2.2. Design Basics of Silicon Strip Detectors . . . . .	34

4.3. Noise . . . . .	36
<b>5. Beam Test Setup</b>	<b>39</b>
5.1. Sensor Layout . . . . .	39
5.2. Construction of the Modules . . . . .	40
5.3. Read-out Electronics . . . . .	42
5.3.1. The Read-out Chip - APV25 . . . . .	42
5.3.2. The Data Acquisition System - APVDAQ . . . . .	43
5.4. Mounting at the SPS . . . . .	43
<b>6. Software Development</b>	<b>47</b>
6.1. The Hephy Analysis Tool (HAT) . . . . .	47
6.2. Analysis Procedure . . . . .	47
6.2.1. Preprocessing of Data . . . . .	47
6.2.2. Signal to Noise Processing . . . . .	50
6.3. Development Process . . . . .	53
6.3.1. Flexibility - The Virtual Frontend Chip (VFC) . . . . .	53
6.3.2. Extensibility - The Plugin System . . . . .	53
6.3.3. Architecture Independence . . . . .	54
6.4. Proof of Concept . . . . .	54
6.4.1. Standard Modules - Consistency Test . . . . .	54
6.4.2. CNM Modules - Concept Test . . . . .	55
<b>7. Data Analysis &amp; Results</b>	<b>59</b>
7.1. Basic Sensor Properties . . . . .	59
7.1.1. Signal & Noise . . . . .	59
7.1.2. Charge Sharing & Capacitive Coupling . . . . .	62
7.2. Angle Resolution Properties . . . . .	65
7.2.1. Full Analogue Calculation Angle Resolution . . . . .	65
7.2.2. Digital Angle Resolution . . . . .	67
7.3. Conclusion . . . . .	69
<b>8. Acknowledgements</b>	<b>71</b>
<b>A. Convolved Landau and Gaussian Fitting Function</b>	<b>73</b>
<b>Bibliography</b>	<b>79</b>



# 1. Introduction

Today's high energy physics experiments already utilise very sophisticated detector technologies that enable precise reconstruction of the structure and kinematics of particle collision thus allowing to draw conclusions about the constitution of matter. Demands on detector systems, concerning precision, speed and material budget, are increasing as new colliding beam experiments like ILC (International Linear Collider) or upgrades to current ones like LHC (Large Hadron Collider) arise.

Beginning with a short description of the LHC and the CMS (Compact Muon Solenoid) concept followed by a preview of the plans for an upgrade, this diploma thesis will also give an overview of the functionality of silicon strip detectors and some insight in the testing of sensors at CERN with the main topics being the analysis of stacked silicon strip sensors for incident angle resolution and the development of software for the processing of raw sensor data.

To gain information on the momentum of charged particles after their production in the central interaction point, a detector module with two stacked strip sensors was designed at the Institute of High Energy Physics which allows the estimation of transversal momentums through the measurement of incident angles. This information is mandatory for the timely selection of interesting events in the so-called first level trigger system (L1-Trigger). Such track-trigger modules will be an important component of a future CMS upgrade. The concept intends to use the displacement of the track after some millimetres to infer the particles incidence angle, which is directly related to the particles transverse momentum. A restriction on small displacements therefore directly leads to a rejection of particles with a small transverse momentum. Since the strip displacement can be determined on module level this method doesn't require communication between modules. Currently, the second level of the trigger system, the so-called High Level Trigger (HLT) uses the full information of the tracking system to reconstruct tracks. This cannot be achieved in the small time frame available for the L1 trigger while the above described method is potentially quick enough. A prototype module was tested with 120 GeV pions at the SPS beam line at CERN. The data analysis aimed to quantify the functionality of the module, geometry and readout logic.

Because of the more complex design of this module, parts of the existent analysis procedures were not feasible any more. Therefore a new software was developed which is able to deal with various geometries and readout logics utilising modern programming paradigms and improved data types which furthermore eases extensions and flexibility. The correctness of the basic software algorithms was tested against a well established software framework using standard strip modules.



## 2. The LHC and the CMS Experiment

### 2.1. Physics Objectives

Throughout the last century there have been major breakthroughs regarding the understanding of elementary particles and their interaction. All the combined knowledge is unified in one big theory, the so called Standard Model of Elementary Particles (SM), which has been tested extensively and shows an excellent agreement with experimental results. Nevertheless, the SM does not incorporate gravitation and shows other inconsistencies with reality. The latter could possibly be rectified by supersymmetric (SUSY) extensions to this theory. Regarding gravitation there are theories under development (String-Theories, Quantum-Loop, ...) which should grow into a Grand Unified Theory, that combines all forces, but fail to produce satisfying results up to now.

#### 2.1.1. The Standard Model (SM)

The Standard Model distinguishes between the constituents of matter, fermions, and the mediators of the known forces, (gauge) bosons, as shown in figure 2.1.

- Fermions: The building blocks of all matter, are spin  $1/2$  particles which can be further divided into subgroups, the Leptons and the Quarks. Every subgroup has 3 generations of particles, which mainly differ in mass. Normal matter is entirely made up of first generation fermions. Every type of fermion has its anti-particle with opposite charge, possibly only the neutrino could be a majorana particle, meaning that it is its own anti-particle [1]. Leptons and Quarks differ in their interaction forces. Leptons are fundamental particles which interact via the weak force and, if charged, via the electromagnetic force. Each generation consists of a particle of charge 1 (electron, muon, tau) and a particle of charge 0, which is the corresponding neutrino (electron neutrino, muon neutrino, tau neutrino). Quarks interact via the strong force and, under normal conditions, cannot exist separated as free quarks but are confined in hadrons. This confinement can have different quark configurations dividing the hadrons into baryons and mesons. Baryons are made of three valence quarks. Mesons are composed of a quark-antiquark pair. Each generation consists of two quarks with different charge:  $+2/3$  and  $-1/3$ . The quarks are called up and down (first generation), strange and charm (second generation) and bottom and top (third generation).
- Gauge bosons: The force mediators, are Spin 1 particles which allow fermions to interact with each other via the electromagnetic, the weak, the strong or even the gravitational force, whereas the particle for the last force, the graviton, with a possible Spin of 2, is yet to be found and is not covered by the SM. The photon is the exchange-particle of the electromagnetic force. The W and Z bosons are the ones for the weak force and the gluons transmit the strong force.

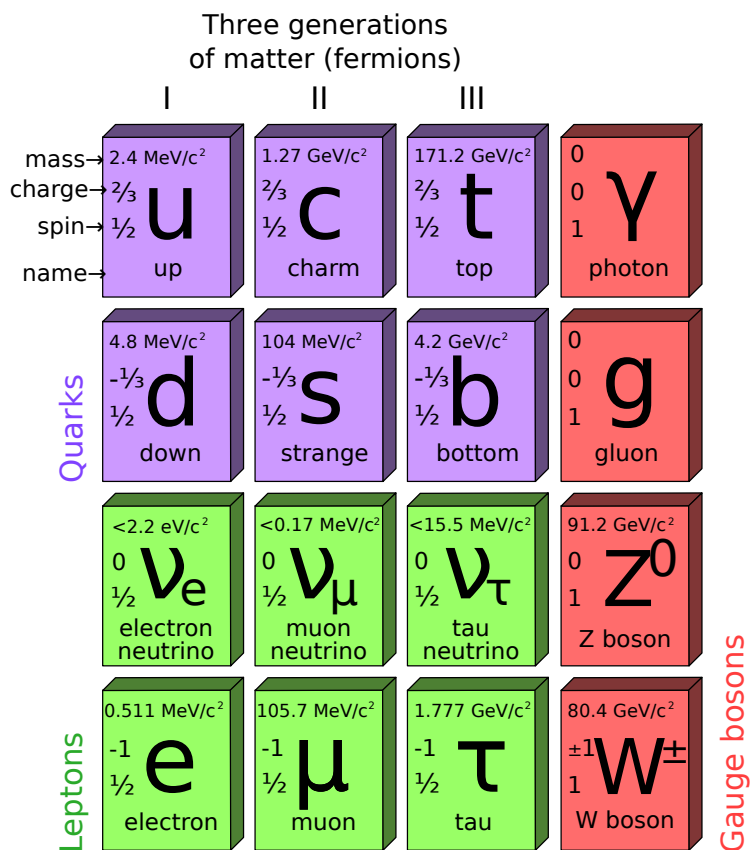


Figure 2.1.: The particles of the Standard Model ([2]).

### 2.1.2. The LHC Goals

Besides other fundamental physics questions the LHC and its experiments were planned to find answers to the following.

- The Higgs-Mechanism and the Higgs-Boson: The SM incorporates, among other things, the electroweak interaction [3] which is a unified description of the electromagnetic and the weak force. This unification is only possible at very high energies e.g. temperatures, like present shortly after the Big-Bang. This theory was first described by Abdus Salam, Sheldon Glashow and Steven Weinberg who were awarded the Nobel Prize in Physics for it in 1979. The electroweak principal is formulated as a symmetric gauge theory based on the gauge group  $SU(2)_L \otimes U(1)_Y$  (the weak isospin and the weak hypercharge) and, because of the Goldstone theorem, should not yield masses for bosons after symmetry breaking, which occurs if the energy level decreases. Symmetry breaking is the process where the state of a system changes from disordered to ordered. As experiments show that the Z and W Bosons have masses different from zero, the Brout-Englert-Higgs mechanism [4] was integrated in the electroweak theorem. Besides Peter Higgs, also François Englert and Robert Brout, as well as, Carl R. Hagen, Gerald Guralnik and Tom Kibble postulated this theory in 1964, concurrently. In

principal the Higgs-Mechanism deals with the non-vanishing masses problem by introducing a new field, the Higgs-Field, which interacts with the other fields in the theory, thereby producing the mass terms for all bosons. All interactions have to be mediated by bosonic particles which in this case has to be the so called Higgs-Boson. The two multi-purpose experiments ATLAS and CMS at CERN were designed to be able to detect this boson in an energy range from 100 GeV to 1 TeV. Recent observations and analysis of data state the existence of the Higgs-Boson at an energy of approximately 125 GeV.

- CP-violation : CP-violation [5] is the combined violation of charge conjugation and parity symmetry. Charge conjugation symmetry is the symmetry between matter and anti-matter. The parity symmetry is symmetry describing invariance under mirroring of a system. The latter was long believed to be maintained for physical systems but was shown to be broken in weak interactions. To explain that, charge conjugation symmetry was introduced. But it was discovered that also this combined symmetries are broken which could explain why our universe consist of matter but not anti-matter. The only problem is that this violation is only true for weak interactions and therefore the effect to small to explain a universe which is devoid of anti-matter. The LHCb experiment at CERN is specifically equipped to find evidence that CP-violation is not restricted to weak interactions by measuring decays based on the strong force.
- Quark-gluon plasma: Quark-gluon plasma [6] is a phase state of matter where quarks are no longer confined in hadrons but exist, together with the interaction particles of the strong force, the gluons, as a kind of free gas. This state is only possible at very high temperatures and pressure, like existent a short time after the Big Bang. By colliding heavy ions the LHC is able to recreate a situation very comparable to the former mentioned and therefore it is possible to study key issues of QCD (Quantum chromodynamics), the theory describing the strong force, like chiral symmetries or the quark confinement itself. CERN's ALICE experiment is specially built to deal with this kind of physics.

## 2.2. The Large Hadron Collider (LHC)

### 2.2.1. Introduction

The Large Hadron Collider (LHC) [7], the largest, most powerful and advanced particle accelerator of the world, was built between 2001 and 2008 in CERN near Geneva (Swiss-French boarder). It is the latest addition to this complex, replacing the Large Electron Positron Collider (LEP), which ended operation in 2000. The LHC's accelerator ring resides in a subterranean tunnel with a circumference of 26.7 km at a depth between 45 m to 170 m.

The idea for the construction of the LHC was mainly motivated by the necessity to prove the existence of the Higgs-Boson (see chapter 2.1.2). It is predicted as an integral part of the extension of the Standard Model of Elementary Particles (SM). This extension allowed to explain why some particles have mass while others are massless (The Brout-Englert-Higgs-mechanism). Hints of it were found by the LEP and the Tevatron, a circular particle accelerator at the Fermi National Accelerator Laboratory in the United States, but with a confidence level of only 95% [8] [9], much less than the

confidence expected to claim a discovery. The project was anything but certain to be realised because of an earlier plan for an even bigger accelerator. This accelerator, called Superconducting Super Collider (SSC), which construction was started in 1991 in the vicinity of Waxahachie, Texas, was cancelled because it well exceeded the original cost projection. Mainly because of Carlo Rubbia, who shared the 1984 Nobel Prize in physics for the discovery of the W and Z bosons, the project really came to life. He argued that even if the LHC with a center-of-mass energy (which is the combined energy the particles collide) of 14 TeV would never be able to achieve a comparable energy of 40 TeV, which the SSC would have had, it would be more versatile because it would not only be able to accelerate protons but also heavy (lead) ions and it would achieve a higher luminosity.

### 2.2.2. Technical Design Features

The event rate  $R$  in a collider is proportional to the interaction cross section  $\sigma_{int}$  and the factor of proportionality is called the luminosity  $\mathcal{L}$ .

$$R = \mathcal{L} \sigma_{int}, \quad (2.1)$$

The luminosity for a beam with a gaussian profile is given by:

$$\mathcal{L} = \left( \frac{\beta_r \gamma_r f_{rev}}{4\pi} \right) \frac{k_b N_p}{\beta^*} \left[ \left( \frac{N_p}{\epsilon_N} \right) F(\Phi_p) \right], \quad (2.2)$$

where  $\beta_r$  and  $\gamma_r$  are the relativistic parameters,  $f_{rev}$  is the revolution frequency,  $k_b$  the number of bunches,  $N_p$  the number of protons per bunch,  $F$  the form factor,  $\beta^*$  the beta function at the interaction point and  $\epsilon_N$  the root mean square (RMS) normalised transverse emittance. Moreover,  $\Phi_p = \theta_c \sigma_z / 2\sigma^*$  represents the *Piwinski angle*,  $\sigma^* = \sqrt{\beta^* \epsilon_N / \beta_r \gamma_r}$  the RMS beam size at the interaction point,  $d^* = \sqrt{\epsilon_N / \beta_r \gamma_r \beta^*}$  the RMS divergence at the interaction point and  $\theta_c \approx ad^* \left( 0.7 + 0.3b \sqrt{\tilde{k}_b \tilde{N}_p / \tilde{\epsilon}_N} \right)$ . The values for  $a$  and  $b$ , in the last equation for  $\theta_c$ , are calculated by simulations [10] and the factors with tilde are normalised to the nominal values.

Particles are pre-accelerated before entering the LHC through a complex of several older accelerators, which are the Linear Accelerator (LINAC2) where 50 MeV protons are generated, the Proton Synchrotron Booster (PSB) which speeds them up to 1.4 GeV followed by the Proton Synchrotron (PS) to further increase the energy to 26 GeV and finally the Super Proton Synchrotron (SPS) which allows the protons to reach their injection energy of 450 GeV. Concerning heavy ions, the acceleration procedure follows a slightly different line. The ions are produced at a different Linear Collider (LINAC3) at an energy of 4.3 MeV and are transferred to the Low Energy Antiproton Ring (LEAR). Their energy is increased to 14.8 MeV and they are injected directly into the PS to be accelerated to 6.15 GeV. The ions are passed to the SPS and without any further increase in velocity fed to the LHC.

The LHC does not provide a continuous particle beam. It is organised in bunches, which are clouds of particles, which enables the precise timing of collisions. In the main accelerator rings of the LHC the energy of those bunches is boosted to the design energy of 7 TeV per beam to be collided at the experiments which are located in underground caverns at certain points, which are shown in figure 2.2, along the LHC tunnel. [11]

Four experiments were built at the LHC, where two large multi-purpose experiments called ATLAS (A Toroidal LHC Apparatus) [12] and CMS (Compact Muon Solenoid) [12] are complemented by two smaller experiments with more dedicated intentions: LHCb [13] to study the CP violation of B-mesons and ALICE (A Large Ion Collider Experiment) [14]. While ATLAS, CMS and LHCb use p-p interactions, ALICE is an experiment which uses the heavy ion operational mode of LHC to study the physics of strongly interacting matter at extreme densities where the formation of quark-gluon plasma is expected.

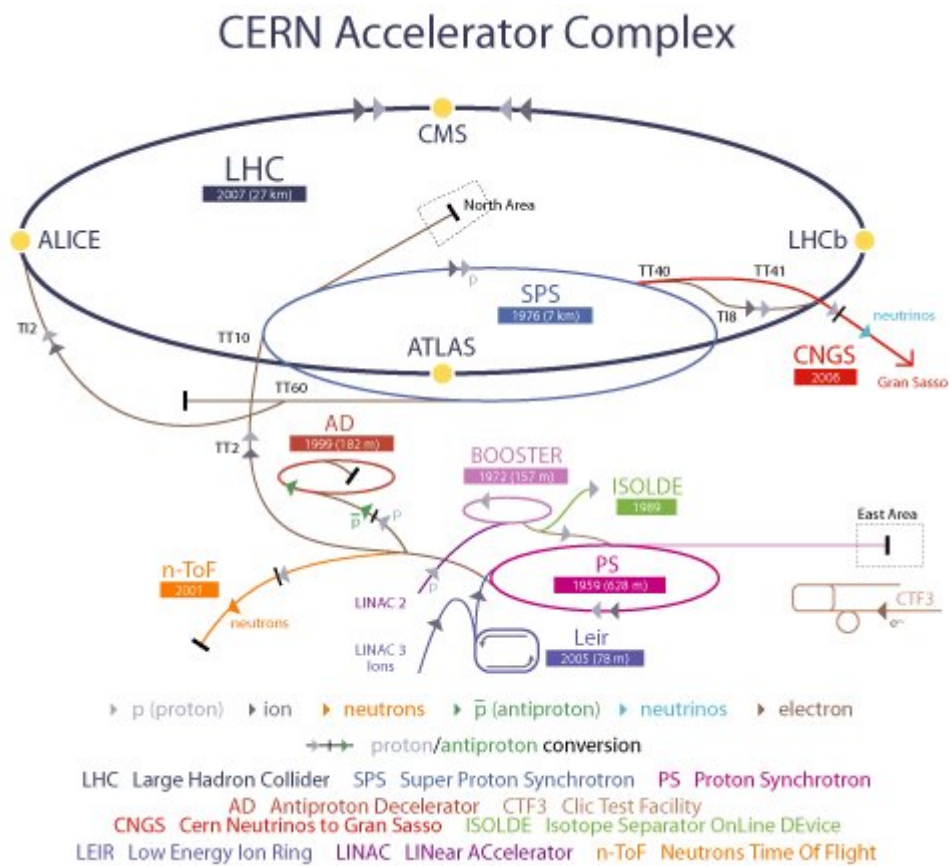


Figure 2.2.: The CERN accelerator complex.

### 2.3. The Compact Muon Solenoid (CMS)

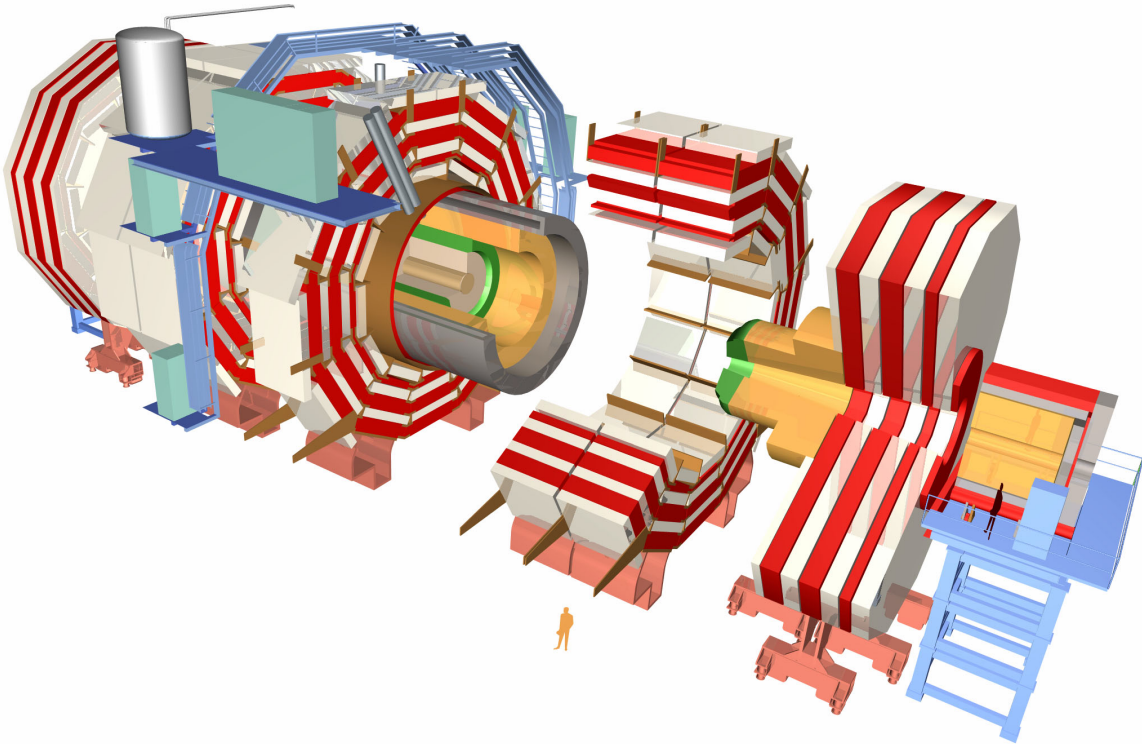


Figure 2.3.: 3D-view of the CMS experiment showing the location of the detector systems.

The Compact Muon Solenoid (CMS), a sketch can be seen in 2.3, is a large multi-purpose experiment located at the northernmost beam crossing point of the LHC. It is specifically well equipped for Higgs-boson and beyond the Standard Model (SUSY) search. The name was chosen because it well describes the specialities of this experiment. It is compact in comparison to the other general purpose experiment ATLAS which volume is nearly 8 times bigger than the one of CMS. It has a very efficient muon detection system which is necessary to select events which show interesting physics. The magnet system uses a solenoidal coil generating a very high magnetic field of 4 Tesla which is only possible due to the use of superconducting wires. The motivation to have two experiments which have a quite similar physical mission is that systematic errors could lead to false results, if there was only one detector.



## 2.3.1. Detector Specifications

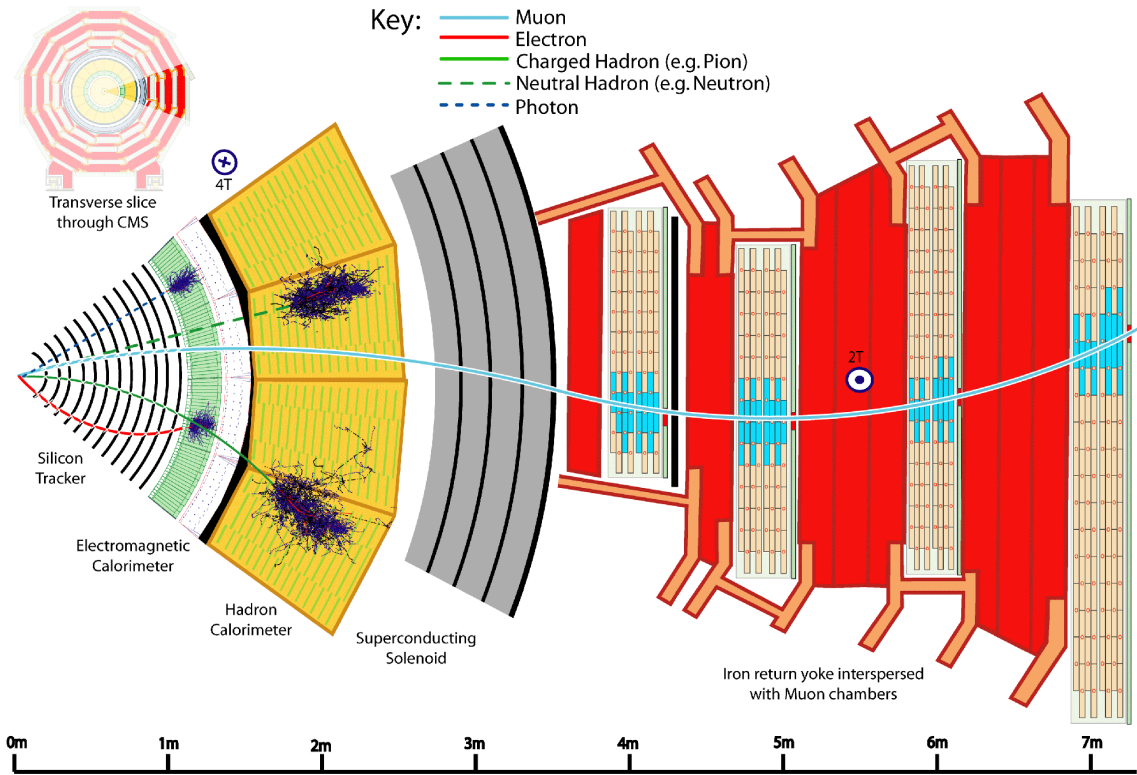


Figure 2.4.: The detector layers of CMS experiment and trajectories of different particles.

At the design center-of-mass energy of  $14 \text{ TeV}$ , the proton-proton cross-section is approximately 100 millibarn, with a luminosity of roughly  $10^{34} \text{ cm}^{-2} \text{ s}^{-1}$ . The proton bunch crossings happen every  $25 \text{ ns}$  which results in approximately 20 inelastic collisions generating 1000 charged particles in this process. This leads to an event rate of about  $40 \text{ MHz}$ , corresponding to  $10^9$  interactions per second. This creates several challenges for the detector system (a picture of the different layers can be seen in 2.4). The online event selection process, called trigger, has to reduce this rate to a maximum of about 400 events/s. This is necessary because any higher rate would render storage and analysis of the data virtually impossible. To deal with the high rate of particle interactions, it is of the utmost importance to use high-granularity detectors with good timing resolution, to keep the occupancy at an acceptable level. Else the products of an interaction under study possibly could get mixed up with those from other interactions in the same bunch crossing. In order to serve its purpose in the LHC physics mission the requirements are following [15]:

- Good muon identification and momentum resolution over a wide range of momenta in the region  $|\eta| < 2.5$ , good dimuon mass resolution ( $\approx 1\%$  at  $100 \text{ GeV}/c^2$ ), and the ability to determine unambiguously the charge of muons with  $p < 1 \text{ TeV}/c$ .

- Good charged particle momentum resolution and reconstruction efficiency in the inner tracker. Efficient triggering and offline tagging of  $\tau$ 's and b-jets, requiring pixel detectors close to the interaction region.
- Good electromagnetic energy resolution, good diphoton and dielectron mass resolution ( $\approx 1\%$  at  $100 \text{ GeV}/c^2$ ), wide geometric coverage ( $|\eta| < 2.5$ ), measurement of the direction of photons and/or correct localization of the primary interaction vertex,  $\pi^0$  rejection and efficient photon and lepton isolation at high luminosities.
- Good  $E_T^{MISS}$  and dijet mass resolution, requiring hadron calorimeters with a large hermetic geometric coverage ( $|\eta| < 5$ ) and with fine lateral segmentation ( $\Delta\eta \times \Delta\phi < 0.1 \times 0.1$ ).

### 2.3.2. Detector Design

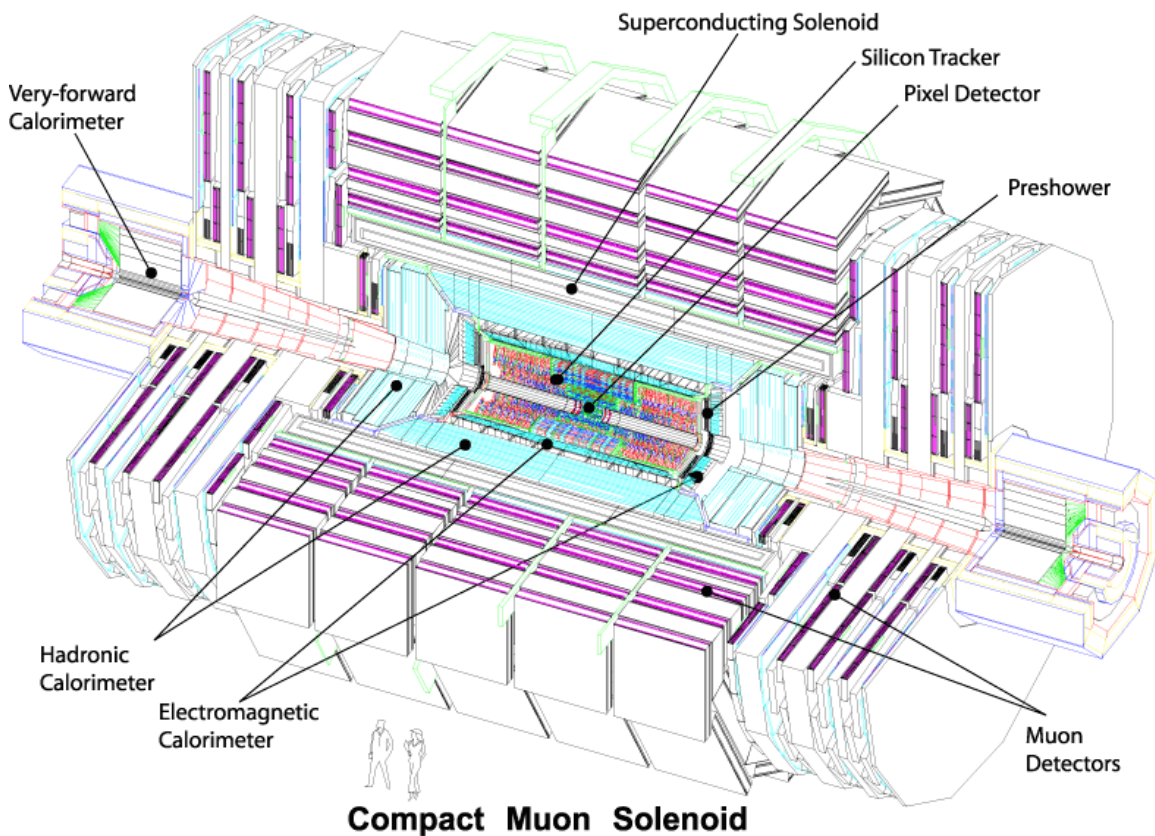


Figure 2.5.: A 3D model of the CMS experiment showing the overall geometry and detector systems.

The overall layout follows a barrel and end-cap geometry, which means that there are several concentric shells which comprise different detection systems (see 2.5) and allow for very good angle coverage. The innermost part is the tracking system. It comprises 3 layers of silicon pixel detectors, which are very close to the interaction region to improve the measurement of the impact parameters of charged particle tracks, as well as the position of secondary vertices, and 10 layers of silicon microstrip detectors, which provide the required granularity and precision. The all silicon tracker has

a length of 5.8 m and a diameter of 2.6 m. The next shell is a EM calorimeter (ECAL) which uses lead tungstate (PbWO<sub>4</sub>) crystals as scintillator material, followed by the brass/scintillator sampling hadron calorimeter (HCAL). All detector systems, described so far, are inside the superconducting solenoid. It is 13-m-long with 5.9 m inner diameter and is able to produce a magnetic field of 4 Tesla, which helped to keep the detector relatively compact. The strength of the return field is sufficient to saturate 1.5 m of iron, allowing 4 muon systems, which are the outer layer of the experiment, integrated in the return yoke of the magnet. All combined the CMS detector has a length of 21.6 m, a diameter of 14.6 m and a total weight of 12 500 tons.

### 2.3.3. The Tracking System

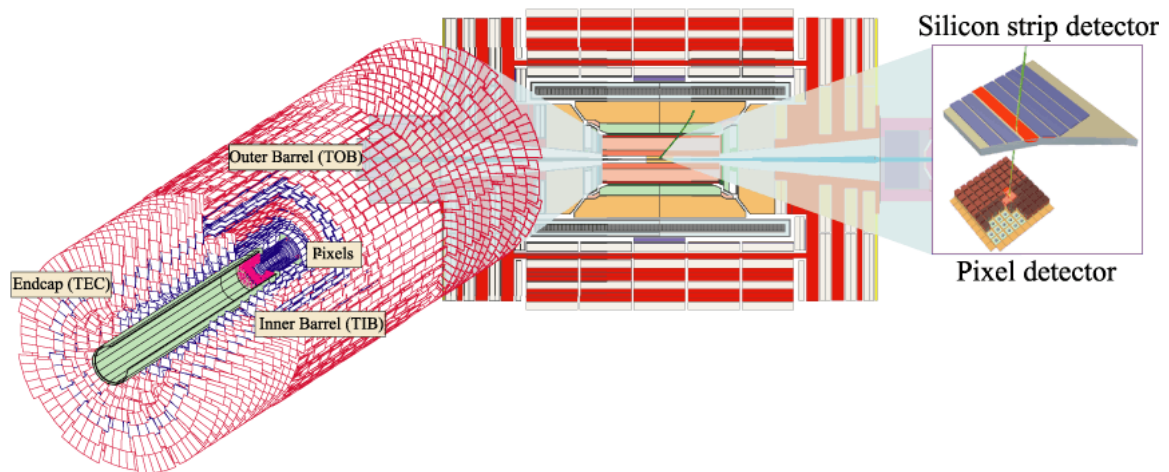


Figure 2.6.: A scetch of the tracking system.

The tracking system or tracker consists of two subdetectors, the strip and the pixel tracker (see 2.6). In short the difference between the systems can be explained with this three requirements [16]:

- Closest to the interaction vertex where the particle flux is the highest ( $\approx 10^7$  /s at  $r \approx 10$  cm), pixel detectors are placed because they offer a high granularity. The size of a pixel is  $\approx 100 \times 150 \mu\text{m}^2$ , giving an occupancy of about  $10^{-4}$  per pixel per bunch crossing at design luminosity.
- In the intermediate region ( $20 < r < 55$  cm), the particle flux is low enough to enable the use of silicon microstrip detectors with a minimum cell size of  $10 \text{ cm} \times 80 \mu\text{m}$ , resulting in an occupancy of  $\approx 2\text{-}3\%$ /bunch crossing at design luminosity.
- In the outermost region ( $r > 55$  cm) of the inner tracker, the particle flux has dropped sufficiently to allow use of larger-pitch silicon microstrips with a maximum cell size of  $25 \text{ cm} \times 180 \mu\text{m}$ , whilst keeping the occupancy at  $\approx 1\%$ .

The pixel tracker consists of three barrel layers with two endcap disks on each side. The three barrel layers which are placed at mean radii of 4.4 cm, 7.3 cm and 10.2 cm, have a length of 53 cm and comprise 768 pixel modules. The two end disks, with a radius from 6 to 15 cm, are located on each side at  $|z| = 34.5$  cm and 46.5 cm and combined are using 672 pixel modules. The measured

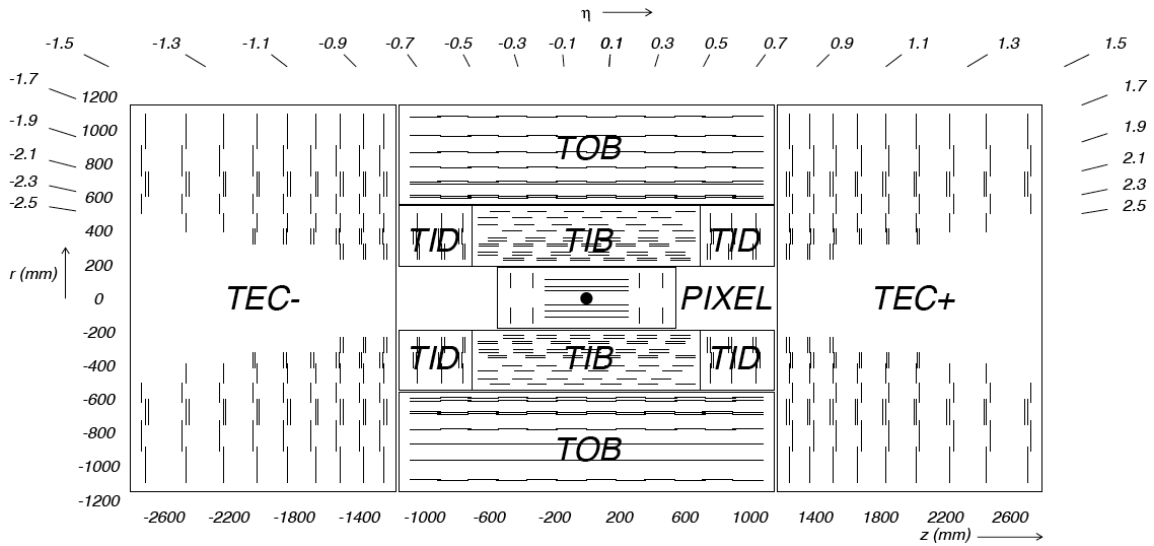


Figure 2.7.: Layout of the CMS tracker. This two-dimensional view is rotationally symmetric with respect to the beam running horizontally through the center. Each single line represents a sensor plane. Layers equipped with stereo modules and therefore providing two-dimensional hit coordinates, are easily spotted by two parallel lines close together.

spatial resolution of the pixel tracker is about  $10 \mu\text{m}$  in the  $r - \phi$  direction and  $20 \mu\text{m}$  for the  $z$ -measurement.

The strip tracker, is divided into four parts, called the tracker inner barrel (TIB) with end disks (TID) and the tracker outer barrel (TOB) where the end discs are called tracker end cap (TEC).

- The TIB consist of 4 layers that are located between  $r = 20 \text{ cm}$  to  $55 \text{ cm}$  and extend to  $|z| = 65 \text{ cm}$  with 2724 sensors which have a thickness of  $320 \mu\text{m}$  and a pitch of 80 and  $120 \mu\text{m}$ .
- The TOB comprises 6 layers that are placed between  $r = 55 \text{ cm}$  to  $110 \text{ cm}$  and extend to  $|z| = 110 \text{ cm}$  with 5208 sensors with a thickness of  $500 \mu\text{m}$  and a pitch of 120 and  $180 \mu\text{m}$ .

To be able to measure the particle position in  $r - \phi$  and  $r - z$  direction two layers in each of this two tracker parts are made with "stereo" modules which are two sensors where one is rotated with respect to the other by  $100 \text{ mrad}$ . The achievable resolution in the TIB is  $23 - 34 \mu\text{m}$  in  $r - \phi$  and  $230 \mu\text{m}$  in  $r - z$ . The TOB has a spatial resolution of  $35 - 52 \mu\text{m}$  in  $r - \phi$  and  $530 \mu\text{m}$  in  $r - z$ .

- The TID has 3 layers, comprising 816 sensors, and is positioned in the gap between the end of the TIB and the end of the TOB.
- The TEC consists of 9 layers, bearing 6400 sensors, extending into the region  $120 \text{ cm} < |z| < 280 \text{ cm}$ .

The sensors of the TID and the TEC are arranged concentric around the beam line with strips pointing to the centre. The first 2 rings of the TID and the innermost 2 rings and the fifth ring of the TEC have "stereo" modules. The thickness of the sensors is  $320 \mu\text{m}$  for the TID and the 3 innermost rings of the TEC and  $500 \mu\text{m}$  for the rest of the TEC.

part	No. detectors	thickness [ $\mu\text{m}$ ]	mean pitch [ $\mu\text{m}$ ]
TIB	2724	320	81/118
TOB	5208	500	81/183
TID	816	320	97/128/143
TEC	2512	320	96/126/128/143
TEC(2)	3888	500	143/158/183

Table 2.1.: Detector types in the silicon tracker. [16]

### 2.3.4. The Calorimeter System

The calorimeter measures the energy of particles. As the interaction of particles in matter is different for hadrons and for light particles which do not interact via the strong force, two specialised systems are needed. First there is the Electromagnetic Calorimeter (ECAL) placed directly after the tracker which measures light particles which interact via the electromagnetic force like electrons, positrons and photons. This system is surrounded by the Hadron Calorimeter (HCAL) which detects the energy of heavy particles which interact through the strong force.

#### Electromagnetic Calorimeter

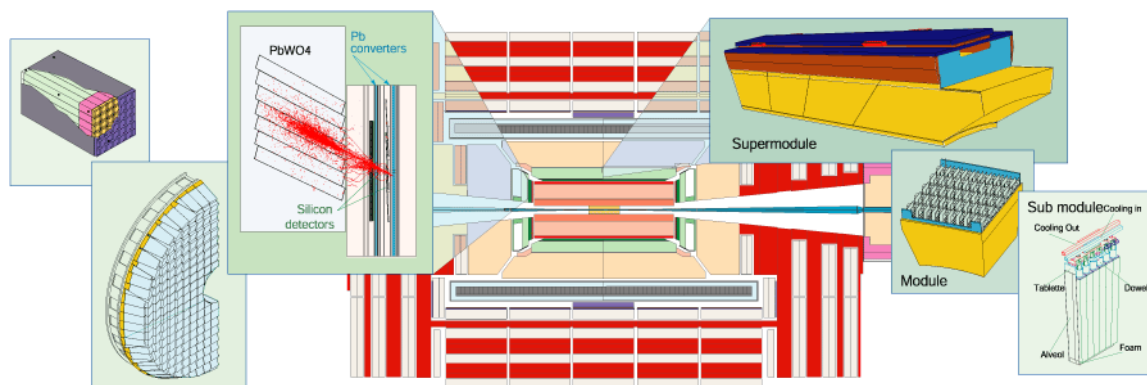


Figure 2.8.: An image of the ECAL.

The ECAL (see 2.8) is a hermetic, homogeneous calorimeter made of lead tungsten scintillating crystals which have short radiation ( $X_0 = 0.89$  cm) and Moliere (2.2 cm) lengths, are fast (80% of the light is emitted within 25 ns) and radiation hard (up to 10 Mrad). 61200 crystals are used in the barrel section and 7324 in every endcap. Because the light yield of this crystals is quite small (30  $\gamma/\text{MeV}$ ), photodetectors with intrinsic gain that can operate in a magnetic field are needed. The barrel section uses Avalanche Photo Diodes (APD) while in the forward parts Vacuum PhotoTriodes (VPT) provide the light measurement. As this systems are sensitive to temperature fluctuations, it is also very important to be able to control the temperature precisely.

## Hadronic Calorimeter

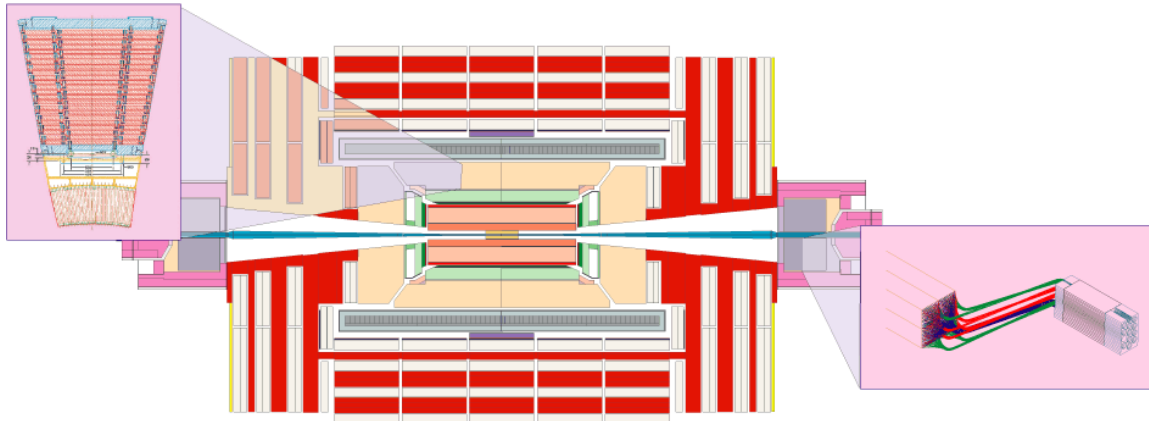


Figure 2.9.: A picture of the HCAL.

The HCAL (see 2.9) is almost completely inside the superconducting coil to minimize the non-Gaussian tails in the energy resolution and to provide good containment and hermeticity for the missing energy ( $E_T^{MISS}$ ) measurement. Therefore it is crucial that its components are non-magnetic. To achieve this, brass was chosen as the absorber material for the major part of the system and plastic scintillators as the active medium. The barrel region and the end caps together cover the pseudorapidity<sup>1</sup> range of  $|\eta| < 3$ . To serve as a tail catcher for penetrating hadron showers leaking through the rear of the calorimeters, there is also a thin layer which is outside the coil, the hadron outer (HO) detector which covers the range between  $3 < |\eta| < 5$  to increase the hermeticity and thus the resolution of the transverse missing energy measurement.

---

<sup>1</sup>Pseudorapidity

$$\eta = -\ln \left[ \tan \left( \frac{\theta}{2} \right) \right], \quad (2.3)$$

is the spatial coordinate describing the angle of a particle relative to the beam axis, where  $\theta$  is the angle between the particle momentum and the latter.



### 2.3.5. The Magnet System

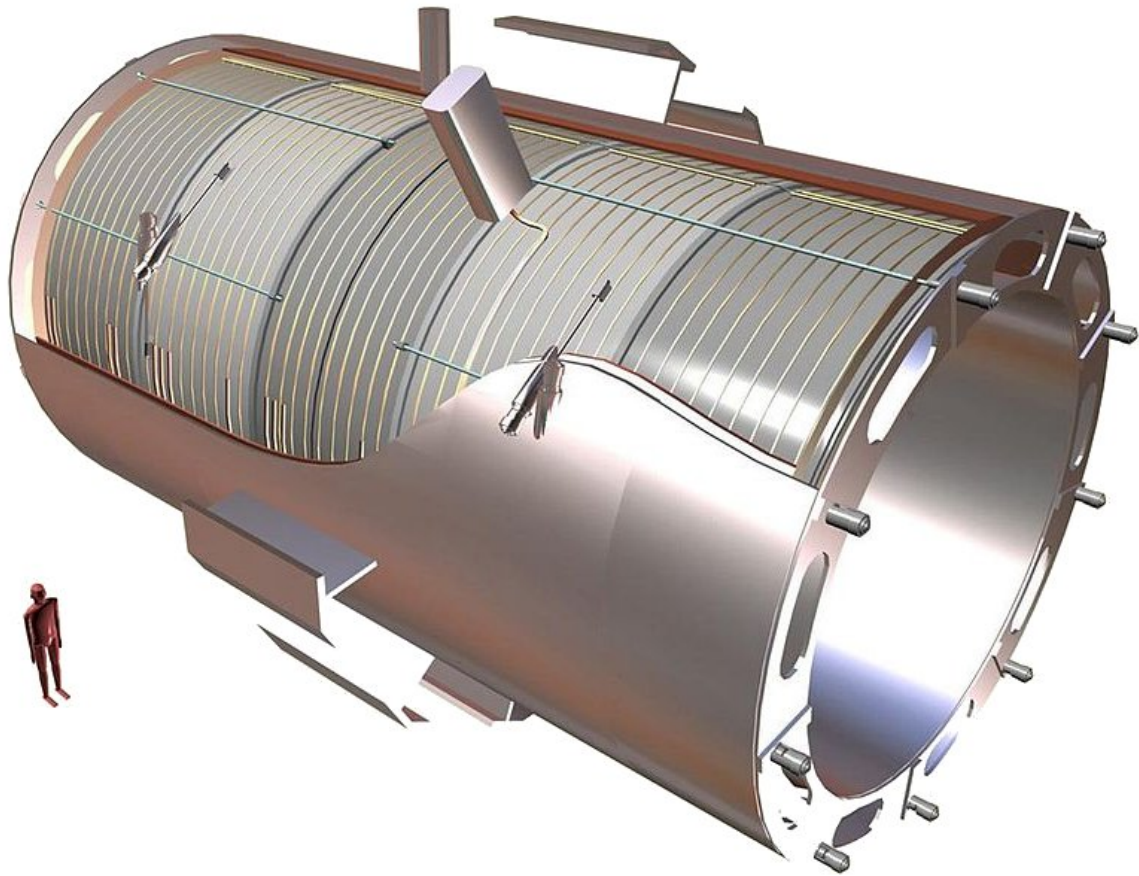


Figure 2.10.: The solenoid magnet of the CMS experiment.

The measurement of charged particle momenta is based on the bending of their trajectories in a magnetic field. Therefore the magnet is a very important component in every high energy physics experiment.

CMS chose a solenoid magnet design (see 2.10) with a length of 13 m and a free inner diameter of 5.9 m which is able to produce a field strength of 4 Tesla. In comparison to a toroidal design it has the advantage that the field lines are parallel to the particle beam. Therefore the muon tracks bend in a plane transverse to the beam. The small transverse dimensions of the beams in this plane allow for a nearly exact determination of the transverse position of the vertex. Furthermore the momentum measurement begins at the interaction center ( $r = 0$ ). To achieve a bending power comparable to a solenoid, a toroid would have to be much bigger. The high strength of the field is also crucial because if the field was weaker it would result in multiple bad influences on the momentum resolution in all systems. In the tracker the resolution would deteriorate as such that the additional running time for the discovery of interesting signals would be 1/3 bigger [17]. See table 2.2 for difference in mass resolution at 4 respectively 3 Tesla.

State	Mass Resolution at 4 T	Mass Resolution at 3 T
$H_{SUSY}(300 \text{ GeV})$	2.1 GeV	2.8 GeV
$H_{SM}(150 \text{ GeV})$	0.8 GeV	1.1 GeV
$B_d^0$	27 MeV	36 MeV
$Y$	36 MeV	48 MeV

Table 2.2.: Mass Resolution for various states at 4 and 3 T [17].

Such a strong magnetic field can only be generated by a superconducting coil which needs a lot of sophisticated supporting systems like cryogenics, power supply, vacuum pumps and quench protection.

### 2.3.6. The Muon System

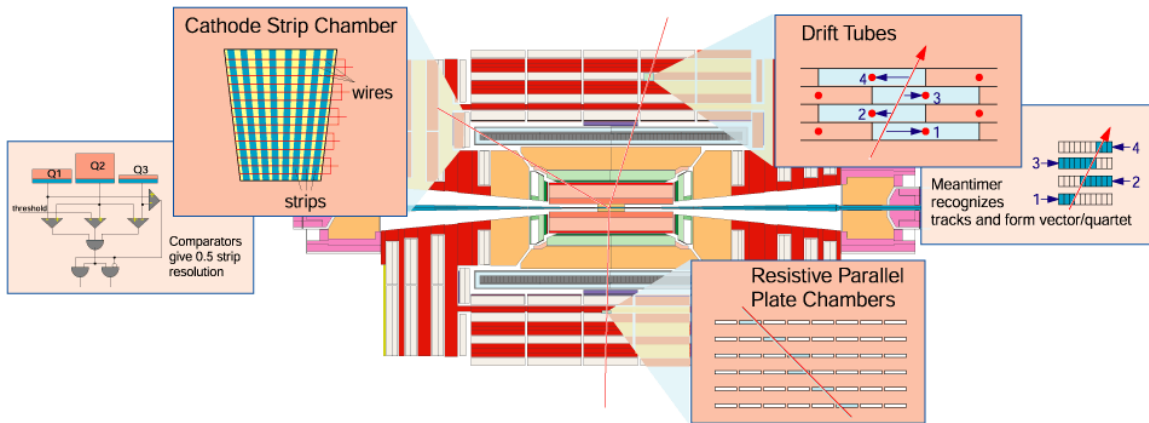


Figure 2.11.: An image of the muon detector.

The muon system (see 2.11) which is embedded in the gaps of the iron return yoke of the magnet consists of three different types of gaseous detectors depending on their position in regard to the neutron background, the muon rate and the residual magnetic field. Together with the tracking system it is used to identify and precisely measure the momentum of muons. In addition it provides fast information to the trigger. The three types are the following:

- **Drift Tubes (DT):** These tubes are filled with gas and contain a single anode wire in the middle of the tube whereas the side of the tube acts as cathode. When the gas is ionised by any charged particle which passes through its volume the measurement of the drift time of the ionization products yields the exact location of the particles. DTs are used in the barrel region of the muon system ( $|\eta| < 1.2$ ) as the return yokes capture most of the magnetic flux resulting in a low magnetic field.
- **Cathode Strip Chambers (CSC):** These chambers are similar to multiwired proportional counters with segmented cathodes. This allows for a position measurement of the particles in two dimensions and, because of the fast response of the closely spaced wires, to provide information



for the trigger. CSCs are used in the end caps ( $|\eta| < 2.4$ ) as they are hardly influenced by a high muon and neutron rate nor the high magnetic field in this region.

- Resistive Plate Chambers (RPC): These chambers consist of two parallel plates, made of high resistive plastic material, which are separated by a gas volume. These two plates act as the anode and the cathode. Because they are made out of plastic, very high electric fields are possible, allowing high amplification of the primary ionisation products generated by permeating particles. The produced currents are collected by a metallisation at the backside of the plastic electrodes. One metallisation is patterned into strips, enabling the RPCs to provide spatial measurements which are used to estimate the muon momentum for the trigger. RPCs are used in both, the barrel and the end caps.

### 2.3.7. The Trigger System

The LHC is designed to generate collisions every 25 ns which is equivalent to a bunch crossing rate of 40 MHz. The bandwidth that would be needed to fully read-out the whole detector at every event is not achievable with today's possibilities. Even after dealing with this issue, the amount of data would be too much to store and to analyse. To handle those problems CMS incorporates two distinct trigger systems which filter interesting events and reduce the data rate.

- The Level-1 Trigger (L1): This system is implemented in hardware utilising custom Field Programmable Gate Arrays (FPGAs). The decision of the L1 trigger, whether to discard an event or keep it, is based on the presence of certain trigger primitives such as photons, electrons, muons and jets above certain  $E_T$  and  $p_T$  thresholds. The information for the L1-Trigger is gathered by the fast systems in the muon detector and calorimeter system. Only if the event is accepted by this trigger the whole data is read out and passed to the High Level Trigger (HLT). The L1 has a time frame of 3.2  $\mu\text{s}$  for its decision which is further reduced to 1  $\mu\text{s}$  because the data buffer is located inside the experiment and the data still has to be transferred. The L1 Trigger can achieve a data reduction in the order of  $1:10^3$  which results in a data rate of 100 kHz for the HLT-Trigger.
- The High Level Trigger (HLT): This system is software based. It applies fast analysis algorithms, comparable to the full reconstruction of the events but with less accuracy, on the data transferred by the L1 further reducing the data rate. A computer grid is used to handle the still massive amount of data.



# 3. Plans for the Upgrade of the CMS Experiment

## 3.1. Physics Motivations for an Upgrade

The LHC accelerator is designed to provide a maximum luminosity of  $1 \times 10^{34} \text{ cm}^{-2} \text{ s}^{-1}$  which leads to an integrated luminosity of approximately  $40 \text{ fb}^{-1}$  per year.

However, after operating the LHC at the nominal design luminosity for some years the statistical errors will only improve marginally, as can be seen in figure 3.1. Increasing the luminosity would help to significantly improve measurements.

The physics potential after finishing the upgrades could be divided into four main topics:

- Improvements of the accuracy in the determination of Standard Model parameters.
- Improvements of the accuracy in the determination of parameters of New Physics which is possibly discovered at the LHC.
- Extensions of the discovery reach in the high-mass region.
- Extension in the sensitivity to rare processes.

A more detailed discussion of this topic can be found in [18].

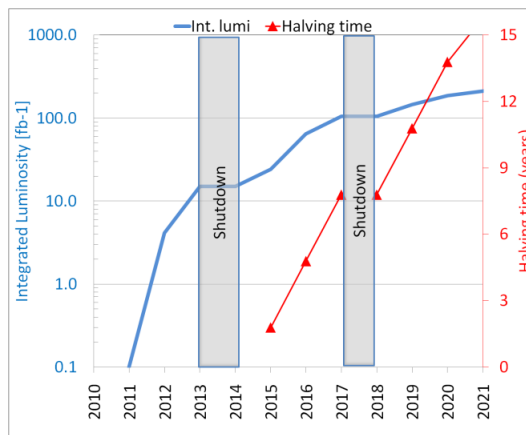


Figure 3.1.: Integrated luminosity (log plot) and time to half the statistical error as a function of years of LHC running.

### 3.2. The High-Luminosity LHC (HL-LHC)

There are two distinct plans for an upgrade of the LHC where the outcome of both was called Super Large Hadron Collider (SLHC). To better distinguish between the different solutions a new naming scheme was introduced, namely the High-Luminosity Large Hadron Collider (HL-LHC) and the High-Energy Large Hadron Collider (HE-LHC).

The first upgrade path is to increase the luminosity. This will be done in two steps during the Longterm Shutdown LS2 with the sLHC-PP project (often called Phase 1) and LS3 with the HiLumi LHC project (often called Phase 2) as can be seen in figure 3.2 and is the topic of this subchapter.

The second path would be to, at least, double the energy of the LHC to 28 TeV center of mass energy. To realise this plan, however, major changes to the existing LHC accelerator ring have to be done. The most challenging and expensive modification is that the main magnets would have to be replaced because the strength of the magnetic field would have to be increased from 8 to approximately 15 Tesla in order to sustain the trajectory of the protons at that energy. As such magnets are still in an early phase of development and their production cost-intensive, the other hypothetical possibility to allow higher energies would be to increase the circumference of the accelerator ring which would only be feasible by digging a new tunnel which is no upgrade anymore but the construction of a new collider.

Because of this problems this scenario is postponed as a possibility after the HL-LHC upgrade.

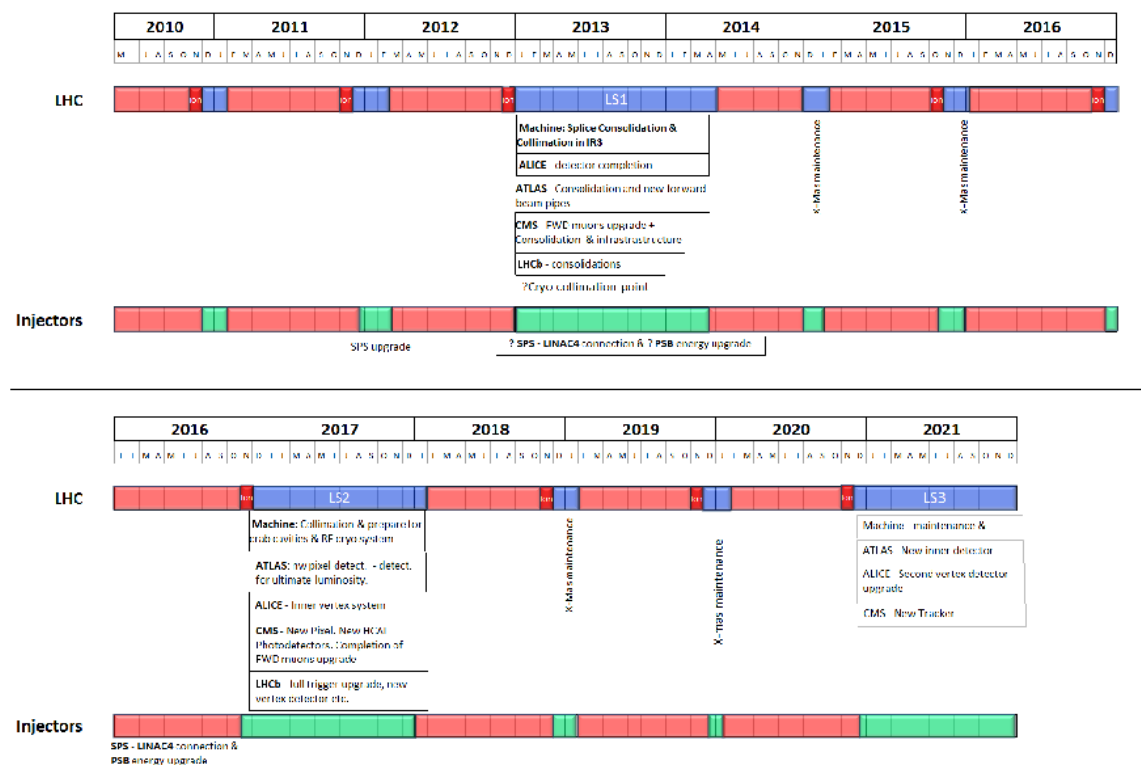


Figure 3.2.: The timescale for Longterm Shutdowns (Draft after Chamomix 2011 LHC Performance Workshop). The blue areas are the shutdown times.

### 3.2.1. sLHC-PP (Phase 1) - Ultimate Luminosity

Before Phase 1, to reach the nominal design luminosity of  $1 \times 10^{34} \text{ cm}^{-2}\text{s}^{-1}$  with a center of mass energy of 14 TeV, there will be a machine stop in 2013 (LS1) which involves the consolidation of the splices at the magnet interconnect (the cause of the incident of September 2008), the consolidation of the collimation system in the warm part, a change of experimental beam pipes to smaller ones (to increase tracking accuracy) and shielding plus relocation of electronic equipment, to avoid detrimental effects from radiation.

Phase 1 focuses on increasing the luminosity to the ultimate luminosity of  $2 \times 10^{34} \text{ cm}^{-2}\text{s}^{-1}$ . For this the beam current has to be increased from 0.58 A to 0.86 A, which is only feasible by increasing the single bunch population from 1.15 to  $1.7 \times 10^{11}$  protons. This is only possible by improving the LHC's injectory chain which increases the beam intensity and its quality, namely switching from LINAC2 to LINAC4, which is under construction. It was also believed that the inner triplets, which consist of 3 quadrupole optical elements and are used for focusing the beam at the interaction regions [19], would have to be exchanged. Because of new estimations of the rate of progress of LHC performance up to nominal, to minimize the machine stops and maximize the productive use of the LHC for physics, the last improvement is delayed for Phase 2. Nevertheless research and development for low- $\beta$  triplets with a larger aperture are ongoing. [20]

In comparison to LINAC2, LINAC4 will produce  $H^-$ -Ions which is preferable to protons because after charge-exchange injection in an accelerator ring through a stripping foil, it is possible to accumulate protons over many turns without blowing up the emittance and it allows for longer pulses in the LINAC with lower peak current reducing the cost on the RF systems. [21]. See table 3.1 for a short parameter comparison.

	LINAC2	LINAC4
Particle species	proton	$H^-$
Output energy	50 MeV	160 MeV
Current	160 mA	70 mA
Beam transverse emittance	$1.00 \times 10^{-7}$ mrad	$4.00 \times 10^{-7}$ mrad

Table 3.1.: Comparison of LINAC2 and LINAC4 [22].

The construction site of LINAC4 is near LINAC2 as can be seen, alongside a schematic of its structure, in figure 3.3.

### 3.2.2. HiLumi LHC (Phase 2) - Beyond Ultimate Luminosity

Phase 2 focuses on increasing the peak luminosity to  $5 \times 10^{34} \text{ cm}^{-2}\text{s}^{-1}$  with levelling which will allow for an integrated luminosity of approximately  $300 \text{ fb}^{-1}$  per year. Luminosity levelling means that by having real time control over the collider parameters, it will be possible to suppress luminosity decay which is caused by protons lost in collision. It also helps avoid an excessive pile-up (multiplicity of events for each proton-proton collision) in the experiments that could partially blind them.

Luminosity depends on several parameters (as described in chapter 2.2.2). An increase in the LHC peak luminosity can be achieved by an improvement of any of this terms but is only feasible

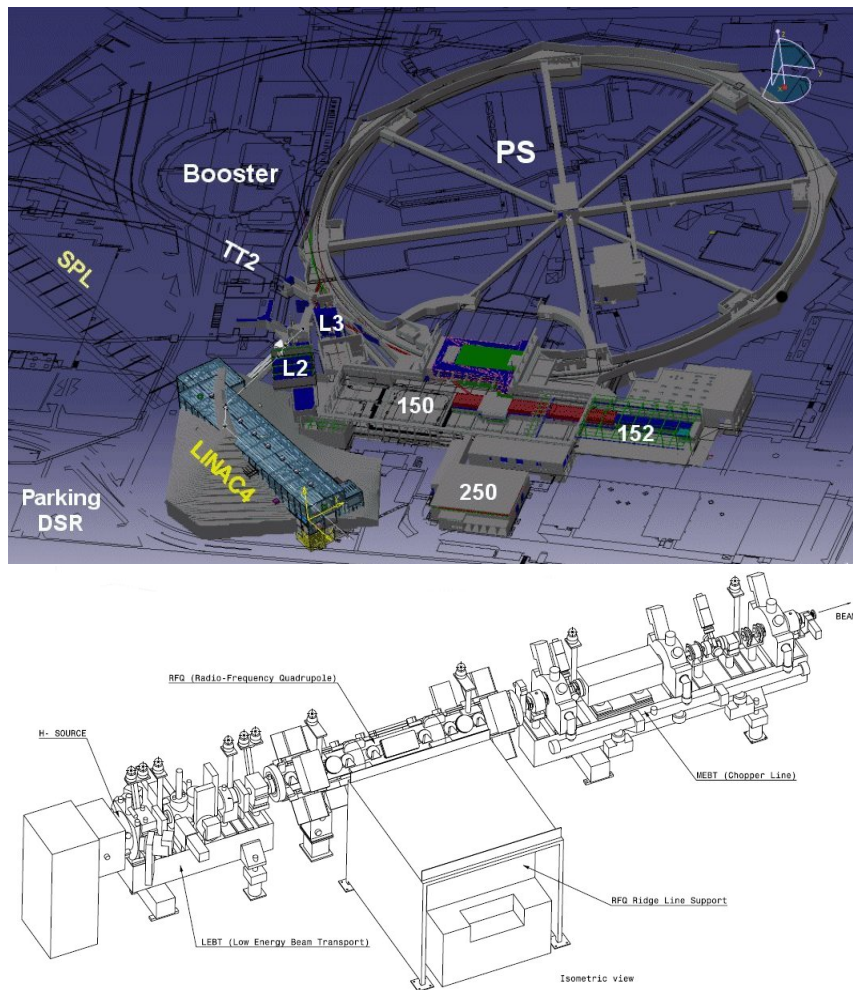


Figure 3.3.: The LINAC4 site (by M. Timmins / CERN) and an illustration of the machine.

with some because of physics principles or hardware limitations. Following are the parameters which can be enhanced [23].

- Bunch spacing: 50 ns bunch spacing is thought of an alternative to the present 25 ns. This could help prevent possible performance degradation produced by the e-cloud or other unforeseen effects. Nevertheless it could prove problematic for the experiments because of a higher pile-up as there will be more interactions in each event. The baseline program therefore still focuses on 25 ns.
- Beam current: Because of the effect of the beam current on almost all systems it will be hard to increase it. Nevertheless, to reach the goal of HL-LHC the "ultimate" value of  $I_{beam} = 0.86$  A has to be raised about 30%, if using 25 ns bunch spacing. Utilising 50 ns spaces between bunches would mitigate the problem as for the same peak luminosity it requires a factor  $\sqrt{2}$  less beam current. However it would shorten levelling time because of the same factor lesser protons are circulating in the machine. To achieve the same integrated luminosity, a higher efficiency would be required.

- **Emittance and bunch population:** To match the HL-LHC goal, the brightness of the beam has to be improved. This can only be achieved at the beginning of the beam generation process and has to be preserved in the injector chain and throughout the whole acceleration of the protons in the LHC rings. Therefore the LHC Injectory Upgrade project (LIU) tries to double the proton number per bunch (proton population) while keeping the emittance at a low level.
- **$\beta^*$  and cancelling form factor F:**  $\beta^*$  describes the beam size at the interaction point. It is a measure of the distance from the interaction point at which the beam is twice the size of that at the interaction point. The lower the beta, the smaller the beam at the interaction point, therefore the better for the physics. LHC machine studies have shown that at present  $\beta^*$  can be reduced to 30-40 cm which is better than the nominal design value of 55 cm. Nevertheless a novel technique called "Achromatic Telescopic Squeeze" (ATS) could lower this parameter even further to 5 cm. 10 cm have been achieved already. A problem is that while lowering  $\beta^*$  the form factor F is growing because a small beta value requires a larger crossing angle. To reduce or even cancel this effect special RF "Crab" cavities are used which are capable to generate a transverse electric field to give the beam a torque. This cancels overlap reduction due to  $\theta_c$  because the crab cavity just rotates each bunch by  $\theta_c/2$ , such as they collide heads on, overlapping perfectly at the collision point.

### 3.3. The CMS Upgrade

#### 3.3.1. Phase 1

Phase 1 of the CMS upgrade focuses on making the detector ready for the increased peak luminosity which is provided by the LHC after LS2 following the sLHC-PP project and prepare it for Phase 2. It has to cope with the higher pile-up to fulfil the LHC integrated luminosity goals and the rising radiation damages. Furthermore the replaceability of components due to falling availability is an issue.

Following is a summary of the planned upgrades.

- **Muon System:** To still trigger efficiently on events with high transverse momentum the CSCs and RPCs will be expanded by a fourth layer of chambers. Also the existing first layer of the CSCs will be enhanced with new electronics so that every strip can be read out separately. The front end trigger primitive chip of the DTs is exchanged for novel ones because they are in short supply due to unexpectedly high mortality.
- **Hadronic Calorimeter System:** The existing photomultipliers of the inner calorimeters will be exchanged with novel ones which will allow for depth segmentation and the use of timing to clear out the backgrounds. Depth segmentation has advantages in coping with higher luminosities and compensating for radiation damage to the scintillators. The forward calorimeters will also be improved by replacing the photomultipliers with ones that have thinner glass windows and metal envelopes to reduce the amount of Cherenkov light generated by charged particles passing through the glass which can lead to false positives for the trigger. The overall improvements provide a better radiation hardness.

- **Tracking System:** The current pixel detector will be replaced by a 4-layer barrel, 3-disk endcap system with ultra-lightweight support and  $CO_2$  cooling. The fourth barrel layer at a radius of 16 cm and the third set of forward disks will maintain the present level of tracking performance in a high occupancy environment. The electronic boards and connections will be moved out of the tracking volume for material reduction. A new readout chip with reduced data loss at higher collision rates, high bandwidth readout electronics and links as well as DC-DC power converters are under development.
- **Trigger System:** It will switch to MicroTCA which is easier to maintain and more flexible with respect to data interconnection. It will allow to take advantage of the full granularity of the data available from the new calorimeter front end and to implement more sophisticated clustering and isolation algorithms.

Furthermore improvements will be made to the Data Acquisition System, the Beam Monitoring System and other common systems as well as some upgrades to the infrastructure and the facility.

A more in-depth discussion on this topic can be found in [24].

### 3.3.2. Phase 2

The second phase of the CMS upgrade will allow the detector to operate in the even higher peak luminosity environment of the HL-LHC after LS3 following the HiLumi LHC project and intends to reach the goal of an integrated luminosity of  $300 \text{ fb}^{-1}$  per year, leading to a total integrated luminosity of about  $3000 \text{ fb}^{-1}$  over the following decade. While some improvements to the detectors achieved during the Phase 1 upgrade will suffice, the demands of Phase 2 require the complete replacement of some detectors and electronic systems. Approximately 100 pileup events per bunch crossing (see figure 3.4), higher radiation damage and material activation have to be handled in order to operate efficiently in the HL-LHC era.

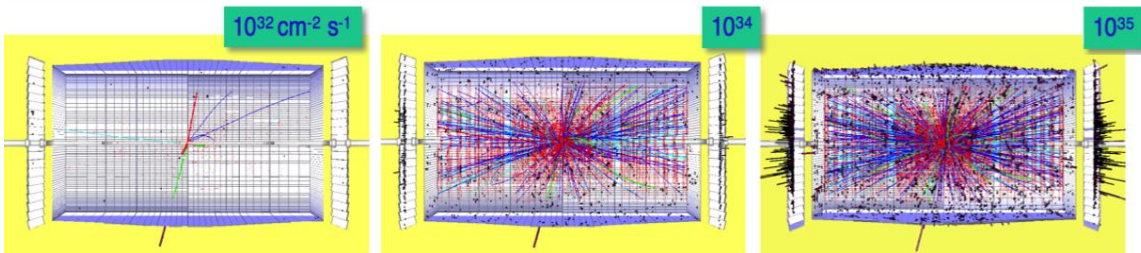


Figure 3.4.: Simulation of bunch crossing and rising pile-up at various luminosities.

Following is a summary of the planned improvements for the Muon System, the Calorimeter System and the Trigger System [24]. The upgrades to the Tracker System will be discussed in more detail in chapter 3.3.3.

- **Muon System:** To cope with the high luminosity and the resulting irradiation levels the electronics of the DTs have to be revised. The CSCs and RPCs face the same problem. There are efforts to allow the fourth RPC station to operate in the high  $|\eta| > 1.6$  region.



Concerning the Level-1 trigger capabilities of these systems, significant improvements in trigger rate control will come from the use of data from the tracker.

- **Calorimeter System:** In the barrel ECAL Anomalous Calorimeter Signals (ACS) are observed which are false signals most probably caused by hadronic interactions in the APDs. As this signals will rise with higher luminosity it is imperative to mitigate their effects. At present the trigger is able to cope with these signals efficiently but will most likely fail in the HL-LHC era. Improvements to the read out electronics will help handling these effects. The components of the forward HCAL and ECAL have to be replaced by more radiation hard technology which is still under development.
- **Trigger System:** To hold the overall trigger rate and performance the suggested approach is to increase the readout bandwidth. This avoids rebuilding front-end and readout electronics as much as possible since these were designed for an average readout time of less than 10 $\mu$ s. It also permits use of front-end buffers for an extension of the Level-1 accept latency rather than more storage before readout. An even more integral part to reach this goal is that the tracker has to provide information for the Level-1 trigger, the Track-Trigger System.

### 3.3.3. The Phase 2 Tracker System - Track-Trigger modules

The new tracker has to be designed with three main aspects in mind: (i) higher radiation resistance, with respect to both instantaneous and integrated levels; (ii) higher readout granularity, to keep the channel occupancy at an adequate level; (iii) ability to contribute information for the Level 1 trigger. This provides CMS with the enhanced discrimination required by the increased pileup. Furthermore existing cables, optics and pipes are likely to be reused as they are routed through other subdetectors and, if exchanged, would add considerable risks and complications, expanding the shutdown time.

Those requirements and constraints lead to following necessary developments:

- Silicon sensors have to maintain adequate performance after accumulated radiation levels approximately 10 times higher than the requirements of the present Tracker. Radiation hard sensors are required everywhere and radically different options may be useful for the innermost pixel layers.
- More advanced ASIC technologies have to be used. The main challenges are to cope with the high instantaneous rates in the inner pixel layers, to limit the power consumption with the higher granularity, and to implement the new trigger functionality.
- Novel powering schemes have to be employed to reduce the cross section of conductors inside the tracking volume and take full advantage of the lower operating voltage of the front-end ASICs, while remaining within the constraint of the existing supply cables.
- More efficient cooling methods have to be used to reduce the mass of cooling pipes and heat exchangers, as well as the mass flow of the coolant, and to cope with the constraints from the existing pipes.
- High-speed data links are required to handle the increased data volume generated by the increased granularity and by the trigger output, and still maintain compatibility with the installed optical fibers.

- Novel module concepts and electronics architectures need to be developed to implement on-detector data reduction, which allows the trigger functionality to be implemented while maintaining the bandwidth at an acceptable level.

This chapter will only focus on the strip  $p_T$  module development. A description on the R&D concerning the other necessary sub-systems can be found in [24].

In the HL-LHC era the tracker not only has to maintain the current tracking performance but also has to provide information for the Level-1 trigger to ensure an output rate of 100 kHz in face of a 10 times higher luminosity. At present tracking data is used only in the High Level trigger achieving a rate reduction of about 100. It is observed that the Level-1 rate is flattening as a function of  $p_T$ . Increasing the threshold would not suffice without including tracking information.

In order to deliver information to the Level-1 trigger the system has to send signals at a rate of 40 MHz, feasible only by reducing the sent data to maintain the overall bandwidth at an acceptable level. This will be achieved by using the strong bending power of the CMS solenoid's magnetic field of approximately 3.8 T in combination with modules that are able to reject, in real time, signals from low- $p_T$  particles.

There are different module designs which could provide this functionality. One of them, the stacked silicon strip sensor approach, is the topic of this thesis. It is following the idea to discriminate high- $p_T$  events from low ones by correlating signals from stacked sensor pairs, as shown in figure 3.5.

A correlated pair of hits in a sensor stack is called a "stub". Dismissing tracks below a given threshold of about 1 GeV or more leads to a data reduction factor of one order of magnitude allowing a data rate of 40 MHz. The full details of the module investigated for this thesis can be found in chapter 5.1 and 5.2.

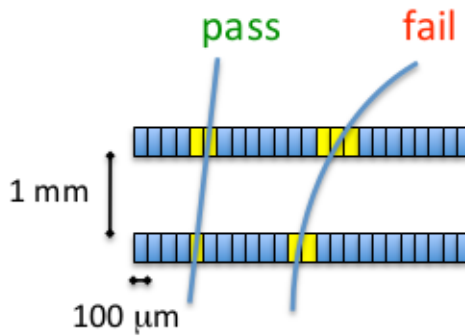


Figure 3.5.: The principle of  $p_T$  discrimination in stacked sensor pairs.

Considering a particle originating from the interaction point which traverses a barrel layer of strip sensors (the strips are parallel to the magnetic field) at a radial distance  $D$ , the projection of the incident angle on the  $r - \phi$  plane can be formulated as

$$\alpha = \sin^{-1}\left(\frac{D}{2R}\right), \quad (3.1)$$

where  $R$  is the radius of the  $r - \phi$  projection of the circular particle track (see 3.6). Calculating  $R$  with

$$R = k \frac{p_t}{qB}, \quad (3.2)$$

with  $k = 0.2998$ , the conversion factor from SI to high energy units,  $p_t$  the transverse momentum (in units of  $GeV/c$ ) and  $q$  in multiples of the elementary charge. Therefore the transverse momentum can be written as

$$p_t = \frac{kqDB}{2 \sin(\alpha)}, \quad (3.3)$$

which is an analytical function of the incident angle (a plot using this function can be seen in 3.7).

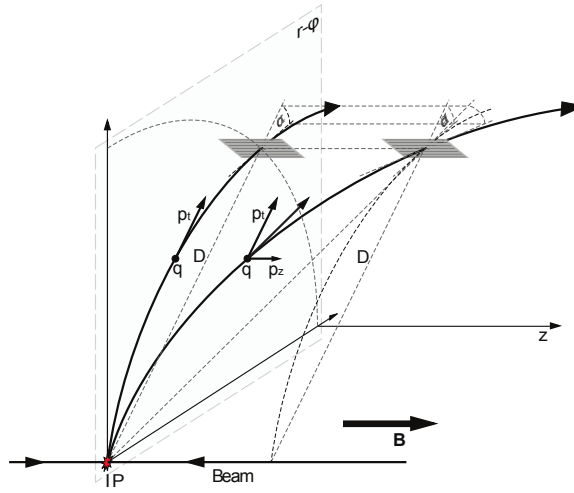


Figure 3.6.: The projection of the intersection angle on the  $r - \phi$  plane has the same size regardless of the momentum in  $z$ -direction ( $p_z$ ).

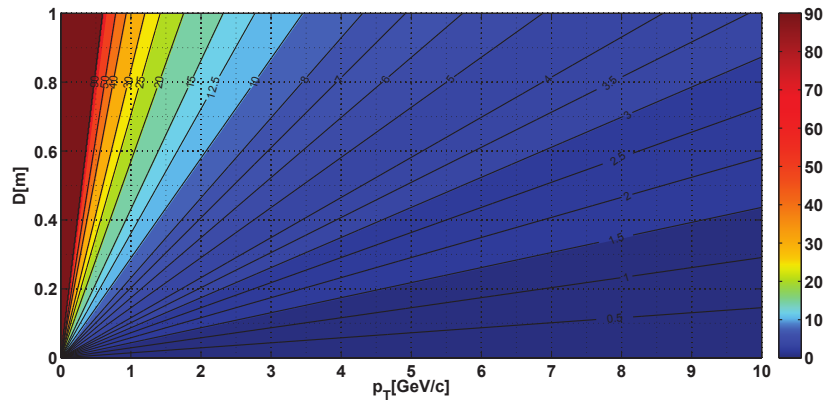


Figure 3.7.: Intersection angle  $\alpha(p_t, D)$  of particles with transverse momentum  $p_t$  emanating from the interaction point, hitting the sensors in radial distance  $D$ .



## 4. The Silicon Strip Detector

### 4.1. Charged Particles in Matter

The working principle of silicon detectors is that if charged particles traverse matter they lose part of their kinetic energy by electromagnetic interactions with the nuclei and electrons of the material.

#### 4.1.1. Light Particles - Electrons and Positrons

At high energies, electrons  $e^-$  and positrons  $e^+$  lose their kinetic energy mainly because of bremsstrahlung. In the lower energy regime the main loss is due to ionisation. This can be seen in figure 4.1.

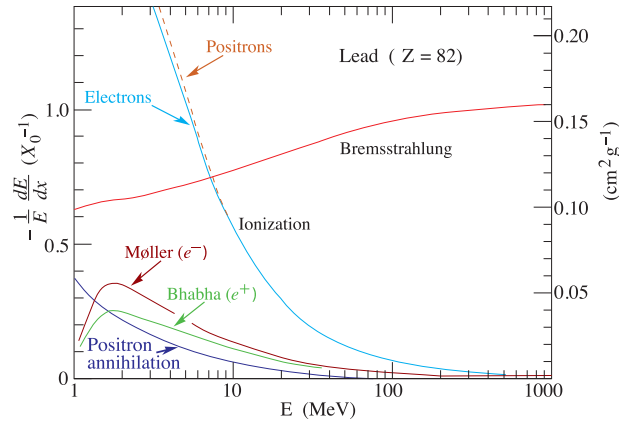


Figure 4.1.: Fractional energy loss per radiation length  $X_0$  in lead as a function of electron or positron energy [25]. In the low energy regime ionisation is the more dominant process. At high energies ( $> 1$  GeV) bremsstrahlung has the most influence.

The overall energy loss of high energy electrons and positrons can be characterised by the radiation length  $X_0$ . It is defined as the average amount of matter that is traversed by the particles while losing  $1/e$  of its kinetic energy by bremsstrahlung. For silicon  $X_0$  is approximately  $9.36 \text{ g/cm}^2$ .

#### 4.1.2. Other Particles

The energy loss of heavy particles (see 4.2) occurs mainly because of ionisation and excitation of the shell electrons. This is described by the Bethe-Bloch equation [25]:

$$-\left\langle \frac{dE}{dx} \right\rangle = K \frac{Z}{A} \frac{z^2}{\beta^2} \left[ \frac{1}{2} \ln \frac{2m_e c^2 \beta^2 \gamma^2 T_{max}}{I^2} - 2\beta^2 - \delta - 2\frac{C}{Z} \right] \quad (4.1)$$

Symbol	Definition	Units or Value
$Z$	atomic number of absorber	
$A$	atomic mass of absorber	
$K$	$4\pi N_A r_e^2 m_e c^2 / A$	$0.307075 \text{ MeV cm}^{-1}$
$ze$	charge of incident particle	
$m_e c^2$	electron mass $\times c^2$	$0.511 \text{ keV}$
$\beta$	particle velocity in units of speed of light	$v/c$
$c$	speed of light	$299792458 \text{ m/s}$
$\gamma$	$(1 - \beta^2)^{-1/2}$	
$T$	kinetic energy	MeV
$I$	mean excitation energy	eV
$T_{max}$	maximum kinetic energy transfer to a free electron	eV
$\delta$	density effect correction	
$C$	shell correction	

The last two factors were not included in the original formula. The density effect correction  $\delta$  is needed to compensate the effect of the polarisation of the material by the electric field of the incident particle at high relativistic energies. The shell correction  $C$  accounts for the non-stationary of the shell electrons during collision at low energies.

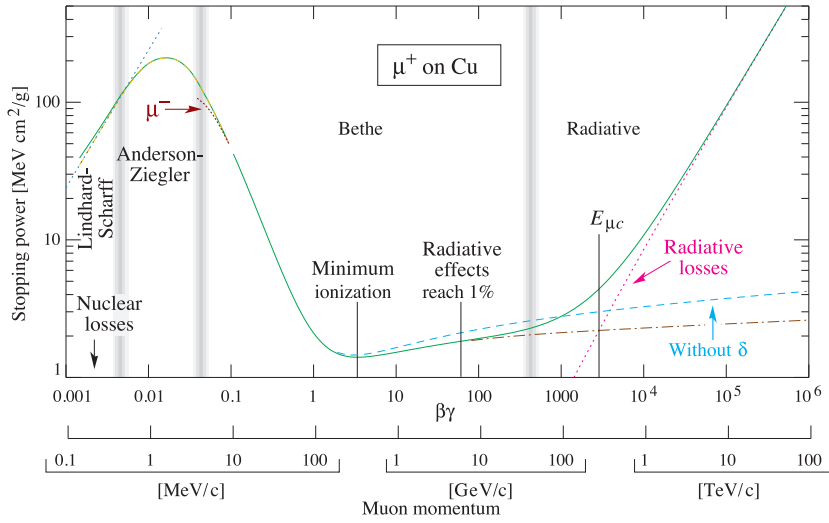


Figure 4.2.: Mean energy loss rate (stopping power) ( $= -\langle dE/dx \rangle$ ) for positive muons in copper as a function of  $\beta\gamma = p/mc$  over nine orders of magnitude in momentum (12 orders of magnitude in kinetic energy) [25]. Solid curves indicate the total stopping power.

### 4.1.3. Energy Loss Distribution

The distribution of the energy loss is highly asymmetric with a long tail towards high energies. As a result the most probable energy loss value  $\Delta_p$  is smaller than the mean energy loss yielded by the Bethe-Bloch formula. This tail mainly evolves from high energetic knock-on electrons, known as  $\delta$ -electrons.

Concerning absorbers with a moderate thickness larger than 2 mm the Landau theory [26] is able to depict the shape of the energy loss distribution accurately. The Landau distribution is given by

$$\phi(\lambda) = 1/2\pi i \int_{c-i\infty}^{c+i\infty} e^{\lambda s + s \ln s} ds \quad (4.2)$$

It has no parameters and its moments are not defined mathematically. The most probable value is located at approximately 0.223. In order to use this definition in energy loss theory 2 parameters have to be introduced. Those are the shifting and the scaling of the distribution. The probability of a particle with velocity  $\beta$  and mass  $m$  to loose the energy  $\Delta$  while traversing a material with thickness  $x$  [ $g/cm^2$ ] is defined as

$$f(\Delta, x) = \frac{1}{\xi} \phi(\lambda) \quad (4.3)$$

where

$$\xi = 2\pi N_A r_e m_e c^2 \frac{Z}{A} \frac{x}{\beta^2} \quad (4.4)$$

and

$$\lambda = \frac{\Delta - {}_L\Delta_{mp}}{\xi} \quad (4.5)$$

while the most probable energy loss is given by

$${}_L\Delta_{mp} = \xi \left[ \ln \frac{2mc^2\beta^2\gamma^2}{I} + \ln \frac{\xi}{I} + j - \beta^2 - \delta(\beta\gamma) \right] \quad (4.6)$$

$I$  denotes the mean excitation energy,  $\delta(\beta\gamma)$  the density effect correction and  $j$  is a constant of the factor 0.2. While this constant is subject to slight variations the most probable loss is not sensitive to its value.

If the absorber material gets thinner the most probable energy resulting from the Landau theory is still correct but the distribution deviates as such that the FWHM is increasingly underestimated [26]. This can be seen in figure 4.3.

There are other energy straggling functions which are better suited to evaluate the energy loss distribution in thin absorbers. All can be derived from a single function, the Shulek function. Following [26] an accurate solution for straggling functions can be derived by utilising the total cross section of a single collision. See figure 4.4 for a comparison of different straggling functions and FWHM for 300  $\mu\text{m}$  silicon.

As the mean energy loss (Bethe-Bloch) is not capable to reproduce experimental data sufficient precisely, it should not be used to estimate the energy deposition in thin absorbers. The most probable value yields a more accurate solution because it is insensitive to statistical fluctuations in the high-energy tail of the distribution and also to possible noise introduced by the measurement.

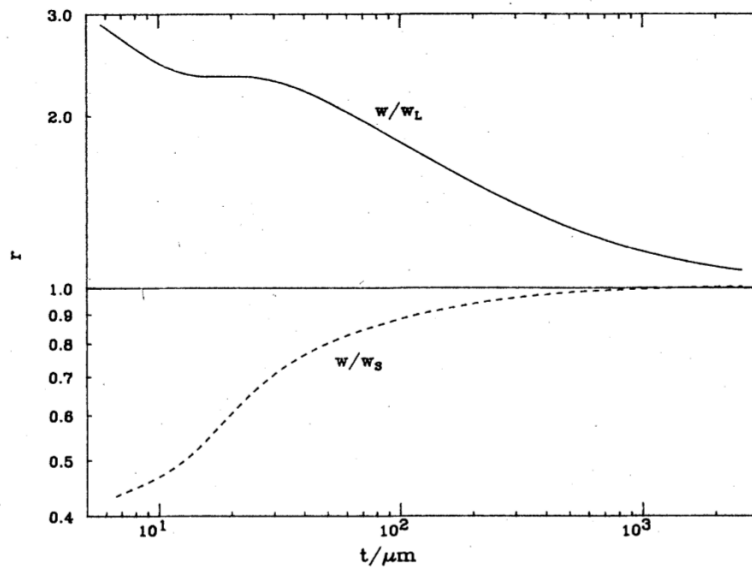


Figure 4.3.: FWHM ratio  $r$  of the straggling function calculated by the single collision cross section. The solid curve represents the Landau function ( $\omega/\omega_L$ ) and the broken line is the Shulek function ( $\omega/\omega_S$ ) over material thickness of passed silicon [26].

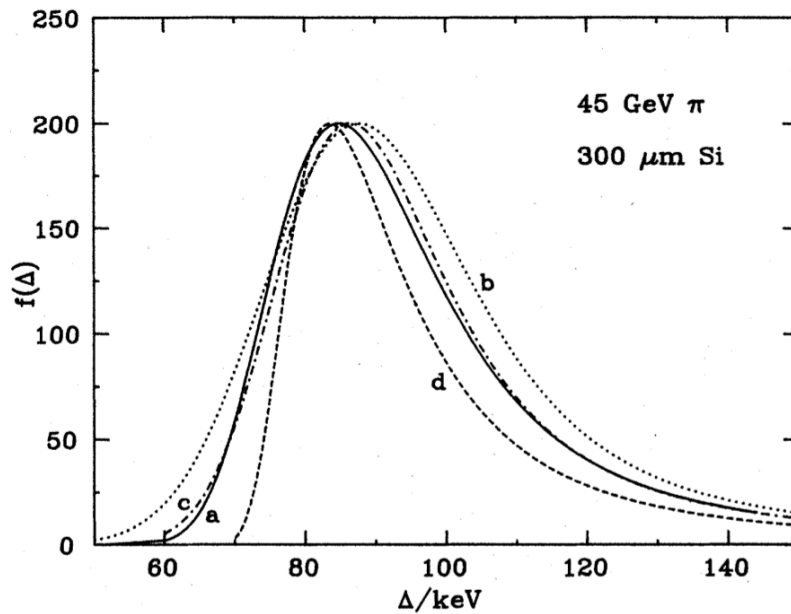


Figure 4.4.: Calculated energy straggling functions for  $45 \text{ GeV}/c$  pions traversing  $300 \mu\text{m}$  silicon. The solid line a shows the accurate calculation using the single collision spectra. The dashed line d shows the Landau distribution. Lines b and c show straggling functions calculated with other approximations explained in [26].



## 4.2. Construction of Silicon Strip Detectors

### 4.2.1. Working Principle

Strip sensors are utilised for the precise spatial tracking of ionising particles. While traversing the sensor the particle interacts with the silicon bulk electromagnetically thereby creating a measurable signal. The underlying process was described in the previous chapter (4.1).

Following the Bethe-Bloch formula 4.1 the mean energy loss of a Minimal Ionising Particle (MIP) results in  $\langle \frac{dE}{dx} \rangle_{MEAN} = 388 \text{ eV}/\mu\text{m}$  and the mean energy of electron-hole creation in silicon  $E_{pair} = 3.63 \text{ eV}$ . The amount of electron-hole pairs generated by a MIP in  $t_{Sensor} = 300 \mu\text{m}$  silicon is

$$\frac{\langle \frac{dE}{dx} \rangle_{MEAN} \times t_{Sensor}}{E_{pair}} = \frac{388 \times 300}{3.63} \simeq 32 \times 10^3 \text{ e}^- \text{h}^+ \text{ pairs} \quad (4.7)$$

In contrast to this, the intrinsic charge generation of silicon at  $T = 300\text{K}$  with  $n_i = 1.45 \times 10^{10}$ , in a  $t_{Sensor} = 300 \mu\text{m}$  thick sensor at an area of  $A_{Sensor} = 1 \text{ cm}^2$  yields,

$$n_i \cdot t_{Sensor} \cdot A_{Sensor} = 1.45 \times 10^{10} \cdot 300 \cdot 1 \times 10^{-4} \simeq 4.4 \times 10^8. \quad (4.8)$$

The intrinsic noise of  $1 \text{ cm}^2$  silicon is four orders of magnitude higher than the signal generated by a MIP. To circumvent this, the sensors could be operated at very low temperatures, which can be practical in certain environments. A more versatile solution is the usage of p-n junctions in reverse bias mode. The basic work principle is shown in figure 4.5.

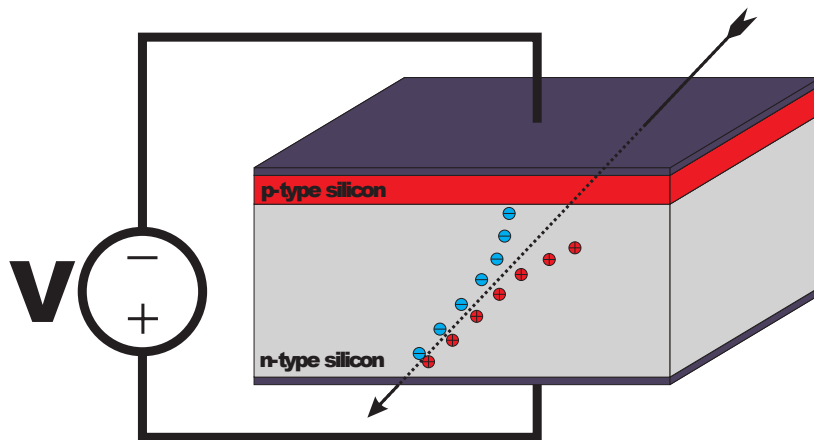


Figure 4.5.: Charge generation of an ionising particle inside the active volume. Due to the electric field the charges drift to the electrodes and induce a measurable current.

For practical reasons, most modern silicon strip detectors (SSDs) are constructed asymmetric with a pre-doped big silicon bulk and a comparable small heavy-doped surface layer. Depending on the preferred application, the type of doping of the two parts can be different. In the case of this study it is implemented as a  $n$ -doped bulk and a  $p^+$ -doped surface. To make the full depth of the bulk sensitive a sufficiently high reverse bias voltage needs to be applied to remove all free charge carriers from the bulk.

Nevertheless thermally generated electron-hole pairs are still present. This leads to a dark current whose fluctuations are a main contributor to the detector noise.

When an ionising particle traverses the active region, it also creates electron-hole pairs. Due to the electric field inside the bulk, the charge carriers start to drift towards the electrodes and thereby induce an electric current which can be measured.

The deposition of energy in thin layers is highly non-deterministic. The statistical fluctuations are considerably asymmetric, following a Landau distribution, as described in 4.1.3. The most probable number of  $e^-h^+$  pairs is,

$$\frac{\langle dE/dx \rangle_{MPV} \times t_{Sensor}}{E_{pair}} = \frac{276 \times 300}{3.63} \simeq 23 \times 10^3 \text{ } e^-h^+ \text{ pairs} \quad (4.9)$$

with  $\langle dE/dx \rangle_{MPV} = 276 \text{ eV}/\mu\text{m}$ . As mentioned before, the most probable value is describing the characteristics more correctly than the mean value.

The  $e^-h^+$  pairs drift towards the electrodes, thereby creating an electric current. Following Ramos's theorem [27] (see equation 4.10) the signal is generated by the movement of the charges in the electromagnetic field and is proportional to the carrier mobilities.

$$J_0 = \frac{q_e}{d} (\sum v_n + \sum v_p), \quad (4.10)$$

where  $q_e$  is the elementary charge,  $d$  the thickness of the detector and  $v_n$  and  $v_p$  the drift velocities for  $e^-$  and  $h^+$ .

The maximum charge that can be collected is calculated by the time integral over the generated current:

$$Q_0 = \int_0^{t_{int}} J_0 dt = \int_0^{t_{int}} \frac{q_e}{d} (\sum v_n + \sum v_p) dt, \quad (4.11)$$

with  $t_{int}$  being the integration time of the amplifier.

#### 4.2.2. Design Basics of Silicon Strip Detectors

Following the principles from the last chapter it is possible to detect a particle traversing a silicon sensor. However it is not possible to gain much other information besides that. As stated before the main purpose of a silicon detector is to give precise spatial resolution to gain information of the trajectory of the particle. In order to get this functionality it is necessary to introduce components that allow for a better determination of the location the particle passes through the sensor. This is accomplished by implementing smaller sensing elements which are electrically isolated but are on the same sensor. There are two distinct designs namely strip sensor and pixel sensor.

##### Pixel Sensors

The name is derived from their geometry. They consist of small quadratic or rectangular sensor elements, called pixel, and provide inherent two dimensional spatial resolution. All elements are read out separately by a dedicated amplifier. The elements have a size in the order of one hundred of microns. This results in a very high pixel density per sensor area.

## Strip Sensors

Strip sensors utilise narrow and long strips which stretch over the whole sensor length. Usually only the upper electrode is segmented. This only yields a one dimensional information of the location of the hit. To gain two dimensional information it is possible to use double sided strip sensors, where also the lower part is segmented and rotated in respect to the upper one. Those, however, involve a more complicated production procedure.

The width of the strips is in the order of tens of microns. The space between the centre of the strips, the pitch, reaches from 50  $\mu\text{m}$  to several hundreds of microns. This influences the spatial resolution and the density of the read-out channels.

Each strip is read out separately by read-out chips. Modern chips can handle up to 128 channels (APV25). The readout chips amplify all channels independently, shape the signal and multiplex them to one output line. In order to provide a sufficient dynamic amplification range for each channel, a fixed bias for the amplifiers is needed. Due to the dark current of a sensor, which introduces offsets in the strip signals, this would not be fulfilled, if the the read-out chips were connected directly to the strips. To resolve this problem the connection to the strips is done via capacitive coupling. This can be done on chip-level or on sensor-level. Usually the capacitors are incorporated into the sensor by an additional strip made of aluminum, separated by a thin layer of silicon-dioxide ( $\text{SiO}_2$ ) as the dielectric. The same material is also used for passivation of the sensor.

The depletion voltage is fed to the implanted strips using a common bias line. Each strip is connected to it using a polysilicon resistor which electrically decouples the strips from each other and can also serve as a current limitation for strips that draw excessive current.

See figure 4.6 for a graphical representation of the described concepts.

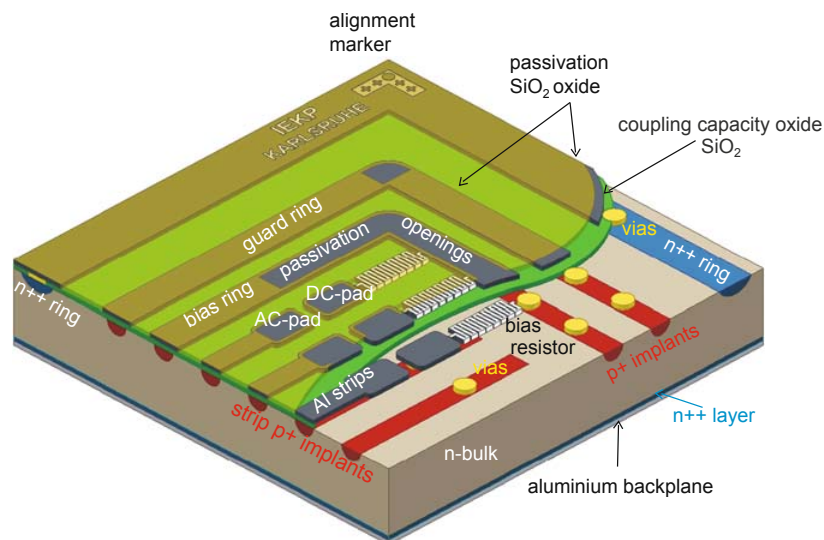


Figure 4.6.: 3D-model of a SSD.

### 4.3. Noise

The noise that is picked up by the readout chip is caused by several sources in the sensor and the chip itself. As the signal is very low, it is essential to deal with all noise contributions effectively. The main contributions of noise will be described in this section. The unit depicting the number of electrons contributing to the total noise is called equivalent noise charge (ENC).

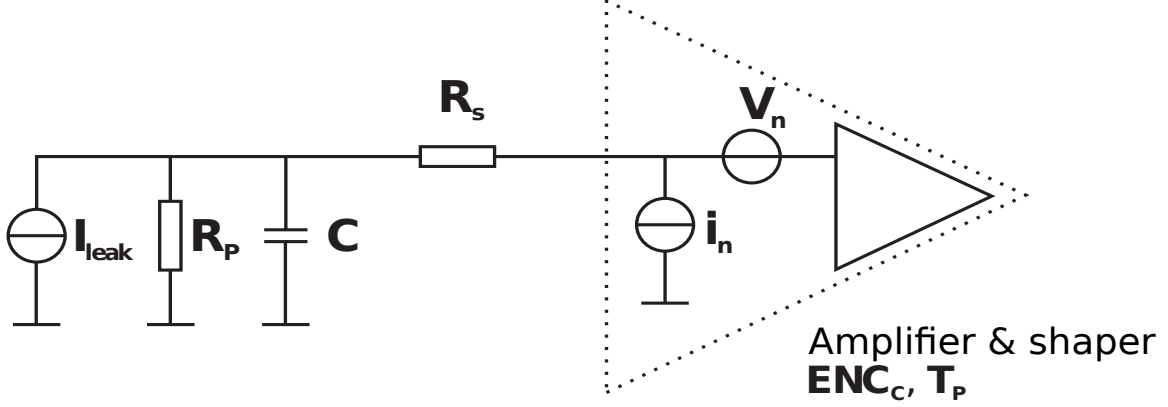


Figure 4.7.: Noise sources of a silicon strip sensor and its amplifier.

Figure 4.7 shows the four main noise sources (leakage current in the bulk  $I_{leak}$ , capacitance of a single channel  $C$ , parallel resistance of the bias line  $R_p$  and serial resistance of the read-out  $R_s$ ) of a common detector system.

All these contributions can be considered independent, leading to a formula for the total noise, reading as

$$ENC_{total} = \sqrt{ENC_C^2 + ENC_{I_{leak}}^2 + ENC_{R_p}^2 + ENC_{R_s}^2} \quad (4.12)$$

A crucial contribution is originating from the capacitance network, which comprises the connections to the amplifier, namely the pitch adapter and the bond wires, and all capacitive couplings of the sensor, the couplings between  $p^+$ -implants, the  $Al$ -read-out strips and the  $Al$  backplane. The total capacitive noise contribution can be defined as

$$ENC_C = a + b \times C \quad (4.13)$$

where  $a$  and  $b$  are amplifier-dependent factors.  $C$  is the capacitance measured for a single channel, which is depending on the geometry of the sensor layout.

Another noise contribution comes from the dark current (leakage current), which can be parameterised as

$$ENC_{I_{leak}} = \frac{e}{2} \sqrt{\frac{I_{leak} \cdot t_p}{q_e}} \quad (4.14)$$

where  $I_{leak}$  is the leakage current induced by one strip.  $t_p$  is the integration time of the CR-RC filter of the read-out chain.  $q_e$  is the elementary charge and  $e$  the Euler constant. As can be seen, a possible reduction of  $ENC_{I_{leak}}$  can be achieved if either the leakage current  $I_{leak}$  or the integration

time  $t_p$  are reduced where latter modification has a bad influence on the  $ENC_{R_s}$ .  $I_{leak}$  depends on the current produced in the active sensor volume and can be expressed as

$$I_{leak} = \frac{q_e n_i}{2 \tau_0} W \quad (4.15)$$

with  $n_i$  being the concentration of intrinsic charge carriers depending, as mentioned in 4.2.1, on the temperature.  $\tau_0$  depicts the generation lifetime of the minority charge carriers.  $W$  is the thickness of the depleted zone. Following equation 4.15 the value of the dark current can be minimised by cooling the substrate to reduce intrinsic charge carriers or by making the the sensor thinner. Lower signal means worse signal-to-noise ratio.

The thermal noise induced by the poly-silicon resistors used to connect the strips to the bias line can be expressed as

$$ENC_{R_p} = \frac{e}{q_e} \sqrt{\frac{k_B \cdot T \cdot t_p}{2 \cdot R_p}} \quad (4.16)$$

where  $T$  is the temperature,  $R_p$  the parallel resistance of each single connection and  $k_B$  the Boltzmann constant. Low temperature, short intergration time and high-impedance resistors help reducing this contribution to the total noise.

Lastly the  $Al$  - read-out strips generate serial resistivity induced thermal noise parameterised as

$$ENC_{R_s} = \frac{e \cdot C}{q_e} \sqrt{\frac{k_B \cdot T \cdot R_s}{6 \cdot t_p}} \quad (4.17)$$

$R_s$  being the serial resistivity of a single strip. In contrast to the the parallel and intrinsic noise, the serial noise decreases if using long integration times. Furthermore the sensors capacitance  $C$  should be kept low.



# 5. Beam Test Setup

## 5.1. Sensor Layout

SSDs can have very different layouts with a wide range of parameters. The choice greatly effects the characteristics, e.g. spatial resolution, radiation hardness, active sensor areas and material budget. It is preferable to have high resolution, predictable stable behaviour towards irradiation and large active areas. The material budget, the amount of material in the detector, should be kept low because every bit of matter that has to be traversed by a particle can lead to multiple scattering which has a bad influence on the outcome of the experiment. Some of these characteristics are contradictory. For example, the thickness of the sensor could be reduced to lower the material budget. This, on the other side, will worsen the signal to noise ratio as less signal is generated. Finding compromises while considering the experimental conditions, requirements and costs, is crucial.

The main goal of this study was to determine the feasibility and performance of stacked silicon strip sensors for incident angle measurement. The two prototypes under test were built of two sensors each with a pitch of 122  $\mu\text{m}$  and a thickness of 500  $\mu\text{m}$ . They were part of the production for the outer barrel of the CMS tracker (OB1) by ST Microelectronics but were not used for this purpose due to potassium pollution of the silicon which led to corrosion of the material [28].

The sensors are single sided, AC coupled and comprise of 768 strips, where only 256 strips were connected to the APVs. All sensors are fully depleted around 160 V. Following

$$\rho = \frac{d^2}{2\epsilon_{Si}\mu_n V_{fd}}, \quad (5.1)$$

whereas  $d$  is the thickness of the sensor,  $\epsilon_{Si}$  the permittivity of silicon,  $\mu_n$  the electron mobility of silicon and  $V_{fd}$  the full depletion voltage. This yields a bulk resistivity  $\rho$  of 5.38  $k\Omega\text{cm}$ , which is well within the specifications of 3.5 to 7.5  $k\Omega\text{cm}$  for OB1 sensors.

The poly-silicon resistors, connecting the bias line to the strips, have a specified resistivity of  $1.5 \pm 0.5 M\Omega$ . Each sensor has a length of 96.4 mm, a width of 94.4 mm and an average active strip length of 91.571 mm [29]. For the  $p_T$ -prototype strips over a length of only 31.5 mm in the center of the sensor were connected to the read-out chip. The aluminium layers of the strips have bond pads on both sides of the sensor. The  $p^+$  layers of the strips can be contacted via probe pads on each side. The dielectric material separating the  $p^+$  implants from the Al read-out layer is composed of Si-Dioxide ( $\text{SiO}_2$ ) and Si-Nitride ( $\text{Si}_3\text{N}_4$ ).

## 5.2. Construction of the Modules

Sensors are delicate devices which have to be operated with much care. To improve robustness during handling and mounting they are built into modules. Modules comprise of the sensor, the frontend electronics and the covering which holds all pieces in place and protects them from the surrounding.

To read out the sensor it has to be connected to the frontend electronics. Those circuit boards which hold the read-out chips, described in chapter 5.3.1, and connect to the data acquisition system are called hybrids. Usually the connection between sensor and read-out chip is made using so-called Pitch Adapters (PA). These are small glass substrates with aluminium lines deposited on top. The PA adapts the pitch of the sensor to the pitch of the input pads of the chip which can be of very different values. Nevertheless for the modules produced for this investigation, this was not the case because the wire-bonding was done in a special manner, described below. Wire bonding is a standard industrial process, using ultra sonic vibrations, to weld a very fine wire to the sensor and the read-out chip.

As described in chapter 3.3.3 the modules investigated in this thesis comprise two sensors which are on top of each other so that the strips are aligned in parallel. It would even be preferable that a particle which traverses the module perpendicular to the sensor surface would hit strips with the same strip number in both sensors. The alignment precision was estimated from previous experiences in module assembly at HEPHY to be in the order of  $100\mu m$  or approximately one strip pitch. Figure 5.2 shows that the strips of each sensor plane of the prototype are not directly superposed. The misalignment is estimated and corrected for in the analysis software 7.2.1.

Another possible problem is that the two sensor planes could be skewed in respect to each other which would lead to different measured strip displacements for the same impact angle of the particle depending on the hit location along the strip. Following the former mentioned alignment precision it can be estimated that even at maximum error, which means that the upper and lower corners of the sensors are displaced about  $100\mu m$  (which of course also means the displacement of the strips), the uncertainty of the displacement of a particle from the lower and the upper part of the pion beam, with a height of approximately  $7\text{ mm}$ , is about  $8\mu m$ . This is much smaller than the pitch of the sensor and therefore can be neglected.

The two sensor planes have a mean distance of  $2350\mu m$  and are wire-bonded such that every odd channel of the APVs is connected to the strips of one sensor plane and every even channel to the others (see figure 5.1). This encouraged the refurbishment of the old data analysis software (see chapter 6) as, amongst other things, it was not able to handle this special geometry efficiently. As the pitch of the sensors is  $122\mu m$  this results in a bonding space of  $61\mu m$  for each read-out channel which therefore is feasible without a pitch-adapter.

Connected to the hybrid, the sensor is glued to a support structure and covered by a cap, both made of Vetronit. To let the particle beam through, the module has openings at both sides. Those are of the size of the sensor area. Finally the openings are shielded with black foil to protect the sensors from light. In figure 5.3 one of the two identical modules that were produced at HEPHY is shown without the foil and the cap.



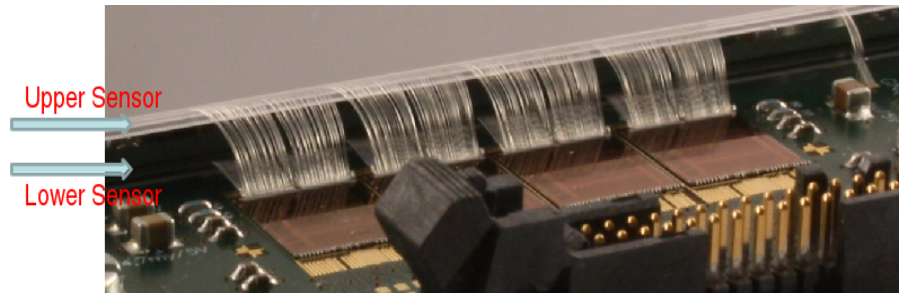


Figure 5.1.: Wire-bonding of the upper and the lower sensor planes of the  $p_T$  prototype.

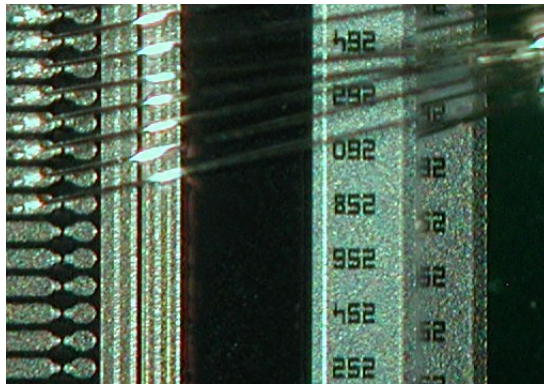


Figure 5.2.: Strip-displacement between the upper and the lower sensor planes. The numbers depict the strip numbers.

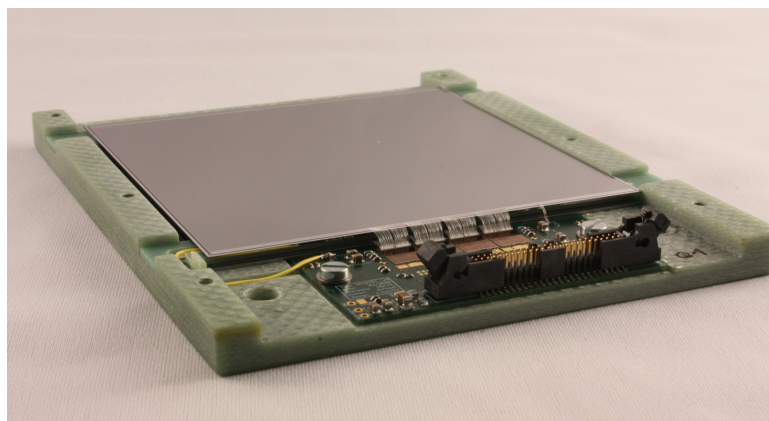


Figure 5.3.: The  $p_T$  module without cover.

## 5.3. Read-out Electronics

### 5.3.1. The Read-out Chip - APV25

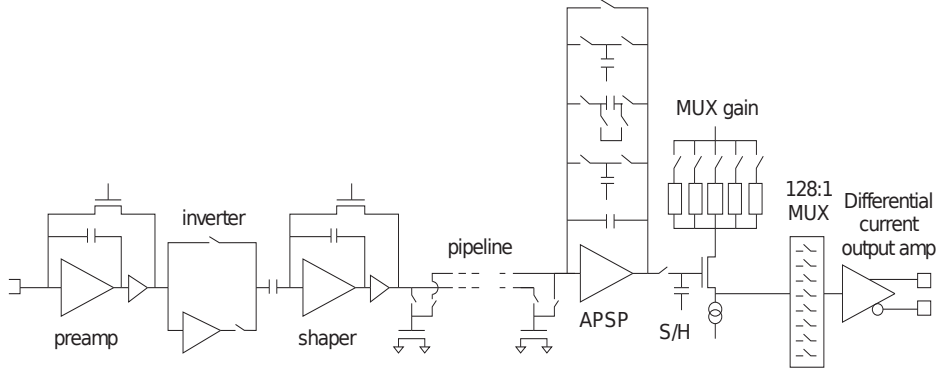


Figure 5.4.: A block diagram of the APV25 read-out chip.

The APV25 read-out chip was originally developed for the silicon tracker of the CMS experiment [30]. It uses standard  $0.25\ \mu\text{m}$  IBM deep sub-micron CMOS technology and is radiation tolerant up to more than  $100\ \text{Mrad}$ . It comprises 128 channels equipped with integrating charge sensitive pre-amplifiers, followed by CR-RC shaper stages with a peaking time of  $50\ \text{ns}$ . The output of the shaper is continuously sampled with the clock frequency of nominally  $40\ \text{MHz}$ , corresponding to  $25\ \text{ns}$  between samples. It is then fed to the analogue pipeline which can store 192 samples that can be extracted upon trigger request. For this reason the maximum time allowed for a trigger decision is about  $4,8\ \mu\text{s}$ . The subsequent data is passed to an analogue pulse shape processor (APSP) and processed depending on the operation mode.

Amplifier:	Charge sensitive pre-amplifier with CR-RC shaper stage.
Input Channels	128
Supply Voltages:	$V_{dd} = +2.5\ \text{V}$ , $V_{ss} = 0\ \text{V}$
Power Dissipation:	$350\ \text{mW}$ nominally
Peaking Time:	$50\ \text{ns}$ nominally
Pipeline:	192 cells
Output:	multiplexed, analog differential current output
Readout:	$40\ \text{MHz}$ nominally
Logical Inputs:	Low Voltage Differential Signals (LVDS)
Chip Size:	$8.055 \times 7.1\ \text{mm}^2$
Manufacturing Process:	$0.25\ \mu\text{m}$ IBM deep sub-micron CMOS
Radiation Tolerance	more than $100\ \text{Mrad}$

Table 5.1.: APV25 parameters.

Besides modes for calibration purposes, there are three data acquisition operating options.

- **Peak Mode:** In peak mode only a single sample of the shaping curve is taken from the pipeline of each channel and passed to the output of the APV25. Hence no further processing by the APSP is necessary. Assuming that the clock and the trigger latency are configured correctly, this sample exactly corresponds to the peak of the shapers output.

- Deconvolution Mode: In deconvolution mode the weighted sum of three consecutive samples is calculated, resulting in a sensitive time window confined to a single bunch crossing. Regarding the CMS experiment this is an important feature, as bunch-crossings happen every  $25\text{ ns}$  which is only half the time the APV25 shaper needs to reach the peak time.
- Multi-Peak Mode: The multi peak mode allows reading multiples of 3 samples from the shaper by sending more than one trigger signal. Again the APSP is not used for processing.

At the test beams, the  $p_T$  prototypes were investigated, the APV25 was operated in multi-peak mode, taking 6 samples.

Following the processing stage the signals of all 128 channels are multiplexed to a different analogue current output.

### 5.3.2. The Data Acquisition System - APVDAQ

To make use of the data provided by the APV25 chip a special read-out electronic and data acquisition software was developed by the Electronics 2 group of the Institute of High Energy Physics at Vienna. The electronics system and the software are steadily improved for testbeams at CERN and other institutes. The system is flexible towards various setups and supports different run modes. A detailed description of the APVDAQ system can be found in [31].

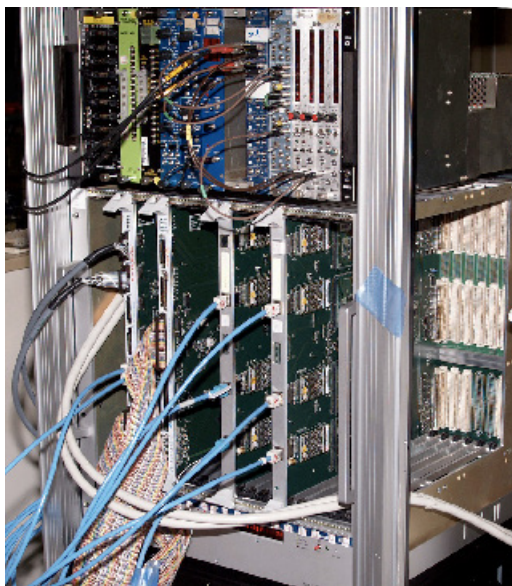


Figure 5.5.: The VME crate.

## 5.4. Mounting at the SPS

The data acquisition for this thesis took place at the H6B area at CERN at the SPS beam line. The stack of the two modules, which henceforth is named device under test (DUT), were mounted on a XYZ-rotation table in between the EUDET telescope (a pixel telescope comprising 6 planes,

developed by DESY Hamburg [32]). Scintillators that were mounted before and after the telescope were used by the trigger logic unit (TLU) to deliver triggers to the APVDAQ and the telescope.

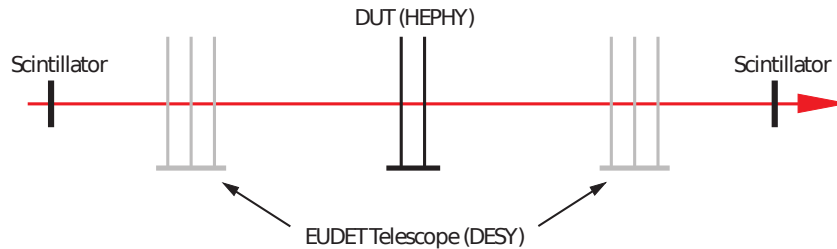


Figure 5.6.: Sketch of the setup showing the scintillators, the telescope and the DUT.

Data was taken over several days using different angles relative to the beam. The first 9 measurements including the angles  $0^\circ$ ,  $1^\circ$ ,  $3^\circ$ ,  $5^\circ$ ,  $7^\circ$ ,  $9^\circ$ ,  $11^\circ$ ,  $13^\circ$ ,  $15^\circ$  were made using angle templates on paper (see figure 5.7) as the XYZ-table rotation stage was not working reliably. On a second occasion 11 measurements comprising the angles  $27^\circ$ ,  $29^\circ$ ,  $31^\circ$ ,  $33^\circ$ ,  $35^\circ$ ,  $37^\circ$ ,  $39^\circ$ ,  $41^\circ$ ,  $43^\circ$ ,  $45^\circ$ ,  $47^\circ$  were done utilising the now fully functioning rotation segment. The first 9 runs were stopped after 20000 events, except the run at  $0^\circ$  where 150000 events were taken. In the 11 later runs 25000 events were recorded for each run but were not used for the analysis in the end because pedestal correction data was not taken and the FIR-filter (see chapter 6.2) was not integrated in the DAQ yet. Both times dry air was used to keep the humidity close to 0 % rHD.

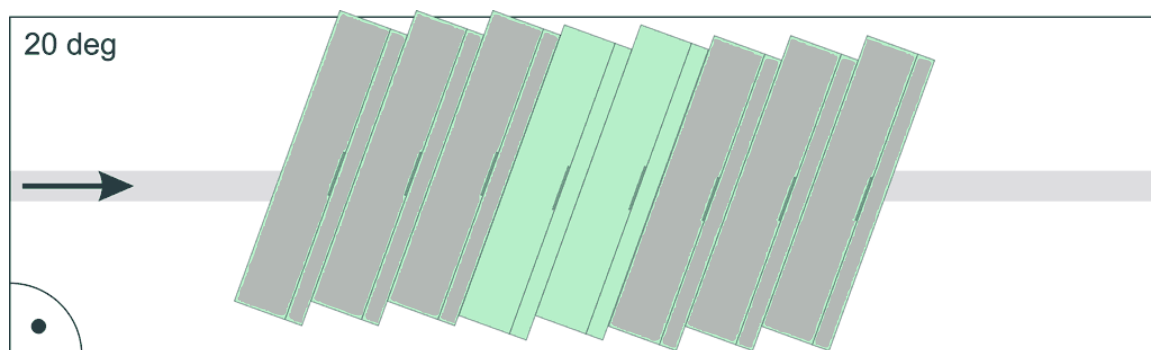


Figure 5.7.: Example of the template that was used to position the modules on the base plate. Only two of the placeholders were used for the  $p_T$  modules.

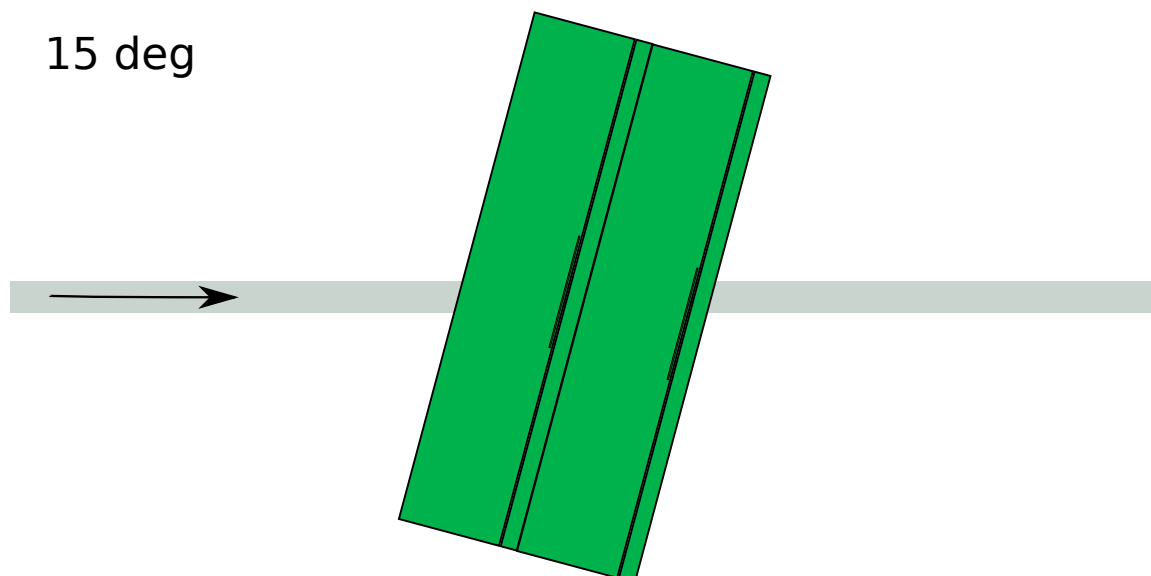


Figure 5.8.: Example for the positioning of the modules in respect to the beam for the last 11 runs.

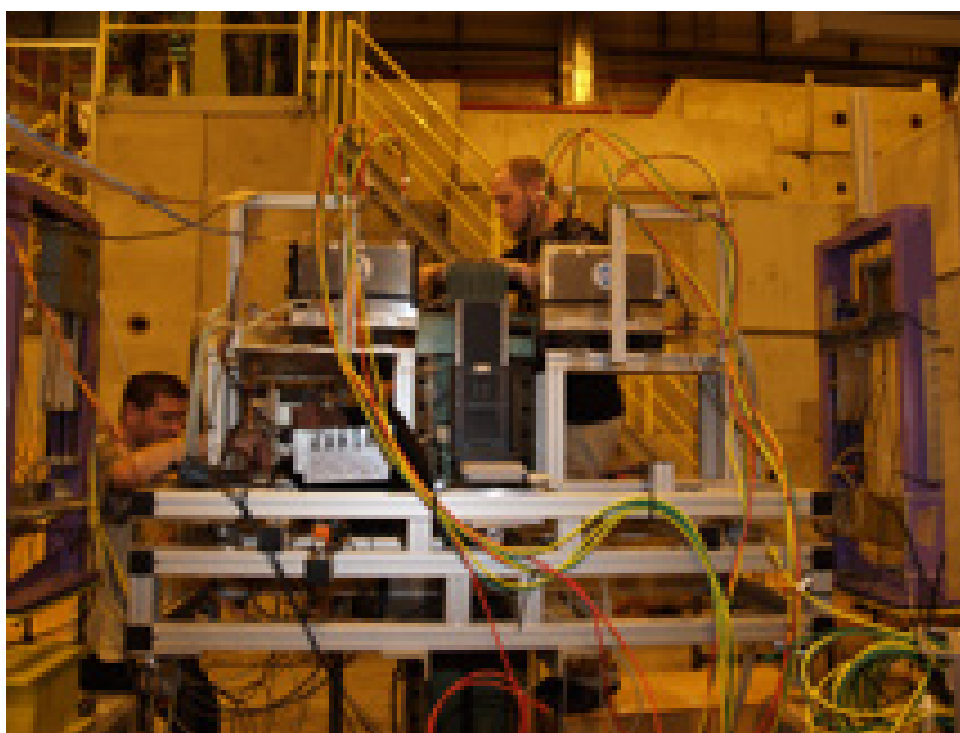


Figure 5.9.: The setup of the experiment at the H6B area.



# 6. Software Development

## 6.1. The Hephy Analysis Tool (HAT)

The "Hephy Analysis Tool", in short HAT, is a newly developed software-suite for Linux-based operating systems, refurbishing the "APVDAQ Analysis" software by the Institute of High Energy Physics [31], for the processing of raw data gained from semi-conductor strip sensors, solely utilising C++11 and the CERN data analysis framework ROOT [33] and therefore completely open source. It is implemented with high modularity in mind to guarantee flexibility towards extensions and exchange of analysis parts where the management of altered or extended functionalities is provided by an included plug-in system. The strictly object-oriented approach allows an easy adoption for parallel computation and eases the development of a graphical user interface. The used data types and structures ensure high independence in regard to the underlying system architecture. All exported data can be browsed by graphical means facilitating the handling of information.

## 6.2. Analysis Procedure

### 6.2.1. Preprocessing of Data

HAT mainly uses two input files, the data file containing the raw strip data and a calibration file comprising the calibration constants of each channel of the APV25 128-channel analogue pipeline chip which is used for the read-out of the silicon strip sensors. Furthermore it is possible to feed pedestal correction data, gained by the APVDAQ system (see 5.3.2, to the software to compensate the influence of long cables. Latter is only necessary if analysing data taken before the introduction of the Finite Impulse Response (FIR) filter [34] which already compensates these effects during data acquisition.

#### Signal Processing

The measured ADC (Analog-to-Digital Converter) value consists of the following parameters, described in [35].

$$S_i^{ADC}(k) = S_i^{part}(k) + P_i + N_i(k) + N_{CM}(k) \quad (6.1)$$

where  $k$  indicates the event and  $i$  the the strip number.  $S_i^{part}$  is the Landau distributed signal of the crossing particle,  $P_i$  the pedestal (the DC offset of the channel output voltage),  $N_i$  the uncorrelated random noise of the particular channel and  $N_{CM}$  the fraction of the noise that influences all channels. While the individual strip noise cannot be removed by software, it is feasible for  $P_i$  and  $N_{CM}$ .

In the standard configuration of the APVDAQ software each recorded data file starts with 600 events, taken with random triggers. The offline analysis uses the first 200 events to calculate the

pedestal of each channel and the remaining 400 are to determine the strip noise. Latter is done chip-wise in two iterations using 200 events respectively.

In the first step the average of the pedestal subtracted signals of the strips ("pedsub"), excluding the five highest and lowest values, is calculated. This avoids the influence of strips with a high noise level on those carrying a genuine signal. Afterwards the resulting common mode noise  $N_{CM}$  is subtracted from the "pedsub" values of each strip yielding the interim pedestal subtracted and common mode corrected signals ("pedsubcmc").

The second iteration determines the  $N_{CM}$  again excluding all strips with a "pedsubcmc" higher than a given threshold (5 times the strip noise, in the standard configuration). This eliminates all strips carrying a hit signal as well as dead ones. Therefore this second stage CMN results in a final "pedsubcmc" comprising only the particle signal and the strip noise (see eq. 6.1). The signals standard deviation of each corrected channel gives the strip noise  $N_i$ .

All following events are recorded with real hardware triggers and processed according to the flow chart which can be seen in figure 6.1.

### Cluster Finding

All steps described so far are processed on chip level, for each APV25 chip. The following hit finding procedure is done for all channels and time samples of a sensor which where read out and is done in a two-dimensional space, spanned by the strips and the time samples of the APV25 chip. Additionally, it is possible to restrict the hit finding to smaller zones of the sensor. This can be used e.g. for multigeometry sensors where only subparts of the sensor share a common geometry. Depending on the incidence angle and the properties of the charge cloud, the charge created by a particle traversing the sensors can be spread over several strips. This is called a cluster. The first part of the cluster analysis scans for such clusters using three different thresholds:

- Seed Threshold (Center of the cluster): To initialise a cluster the signal of a strip has to be over this threshold. In the standard configuration a value of  $5 \times N_i$  is chosen.
- Neighbouring Threshold: If a strip next to a cluster exceeds this threshold it is added to the cluster. The standard value is  $3 \times N_i$ .
- Cluster Threshold: A cluster is valid if the combined signal of all strips in the cluster is over this threshold. The standard configuration uses  $5 \times N_{CLUSTER}$ , where  $N_{CLUSTER} = \sqrt{\sum N_i^2}$ .

While this thresholds yield good results for beams at a low incident angle it can be necessary to adjust the values at high angles because the signal is shared by more strips and thereby can fall below the neighbouring threshold which then leads to a splitting of the cluster.

The results of the first step are stored in a two-dimensional (strip number, sample number) array.

In the second step contiguous areas of entries (clumps) are identified and the rectangular outlines of these fields are calculated, widening each clump to the smallest surrounding rectangle. This is needed as it is possible that a strip carrying only a small amount of the cluster signal lies above the threshold for some samples but below for the remaining hit. To receive the correct cluster signal and noise values the contributions of all strips associated with the particle hit have to be considered



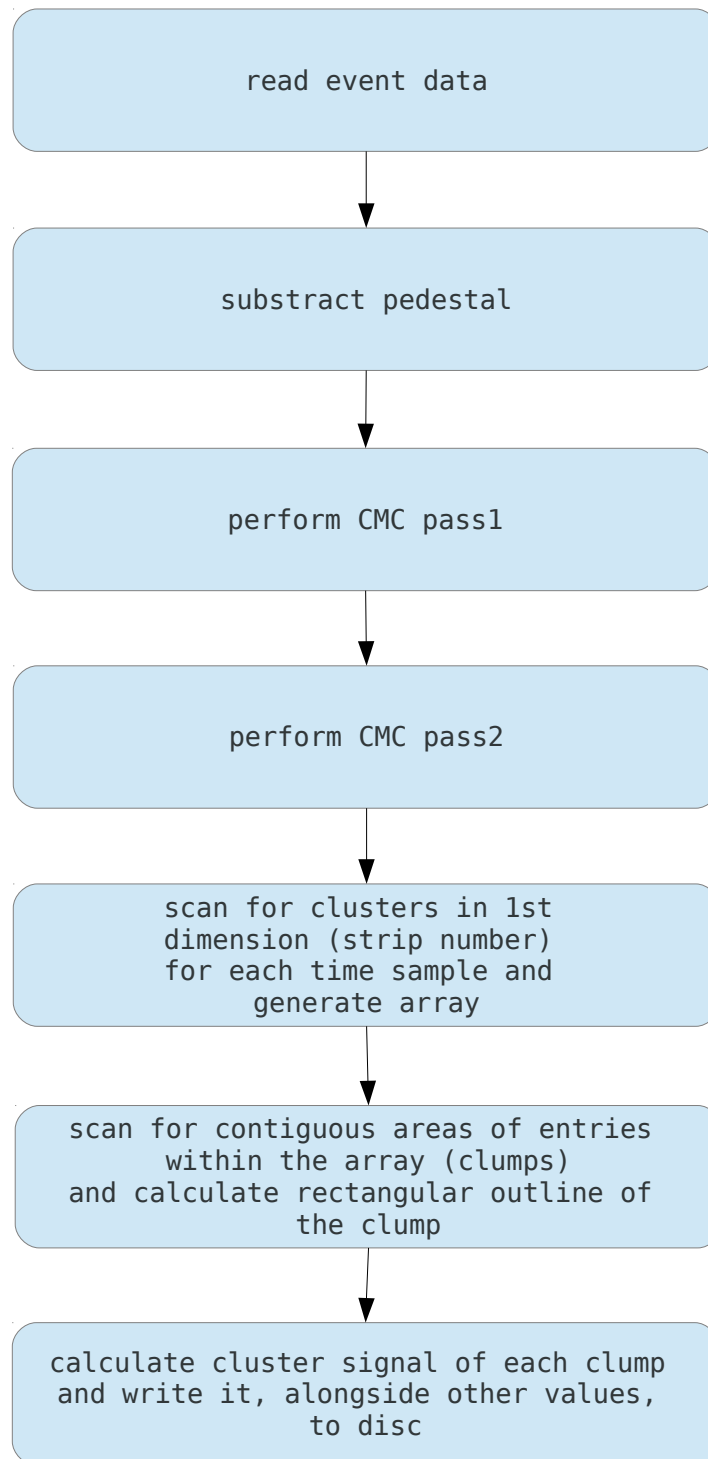


Figure 6.1.: Flow chart of the analysis steps for each event

equally for each sample. For the cluster signal the sum of the strip signals  $S_{CLUSTER}$  is calculated for each sample.

$$S_{CLUSTER} = \sum S_i , \quad (6.2)$$

where  $S_i$  are the signals of the strips that contribute to the cluster. Clumps with a cluster signal below the cluster threshold ( $5 \times N_{CLUSTER}$ ) are rejected thus only valid hits are recorded. In figure 6.2 an example of the outcome of this algorithm can be seen. The hits found in the first step are marked with an  $X$  and the clumps are given by the surrounding rectangles.

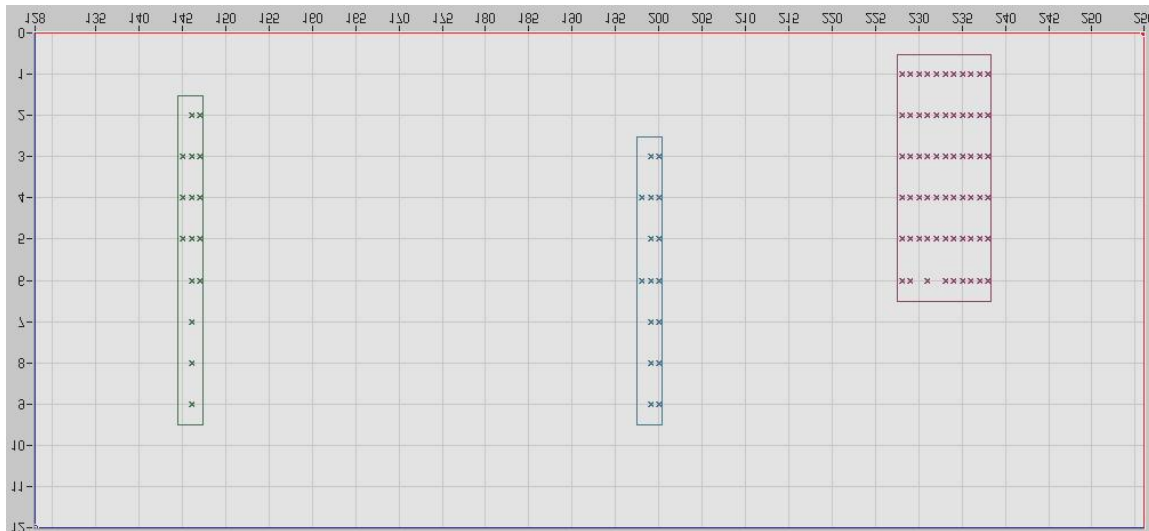


Figure 6.2.: 2-dimensional array used for the cluster analysis. The hits above the threshold are marked with an  $X$ . The surrounding rectangles show the outlines of clumps.

Finally the results, alongside additional information as event number, location in space and time, cluster width, zone number and Time-To-Digital converter (TDC) value, are filled into ROOT specific data structures and stored on disc.

### 6.2.2. Signal to Noise Processing

In order to determine the signal to noise ratio, the cluster signal  $S_{CLUSTER}$  is divided by the cluster noise  $N_{CLUSTER}$ . A typical cluster noise distribution can be seen in figure 6.3. In contrast the cluster signal, which is nevertheless composed of the discrete amount of electrons produced by a hit, is more distributed over the whole scope as can be seen in figure 6.4. The cluster signal is recorded for six time samples. For the signal to noise plots done in this thesis the highest cluster signal in all time samples is used. The ratio can be calculated for each strip or sensor-wide. First can be used to determine the behaviour in certain areas of the sensor. Latter describes the overall performance. After calculating the ratio the most probable S/N value is determined. The functions that correctly describe the signal loss distribution, which where detailed in chapter 4.1.3, are not very practical to use for this purpose. A convenient method to deal with the deviation of the signal from the Landau distribution is to convolute it with a Gaussian. Figure 6.5 depicts a fitted signal to noise histogram for a complete sensor. Regarding the strip-wise signal to noise analysis, an example can be seen in

figure 6.6. In this case the most probable value is plotted for each valid strip. Valid means that the strip comprises enough entries, meaning that it provides sufficient statistics, is not marked as bad and is under a certain noise value (The last two indicators are defined in the configuration files of the software).

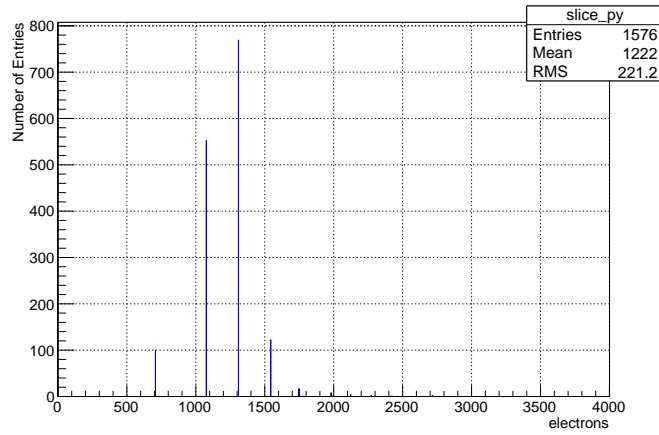


Figure 6.3.: Histogram of the cluster noise.

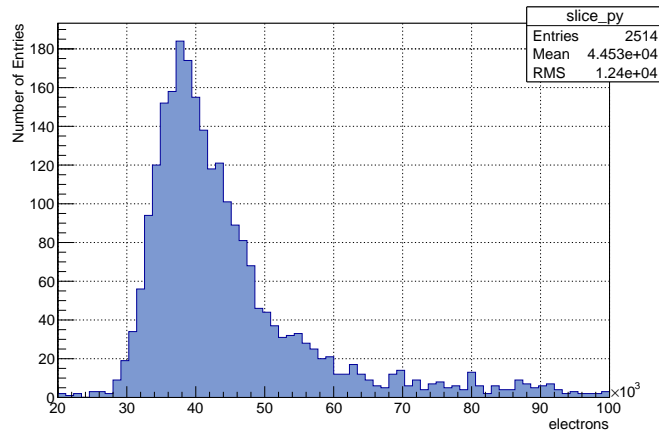


Figure 6.4.: Histogram of the cluster signal.

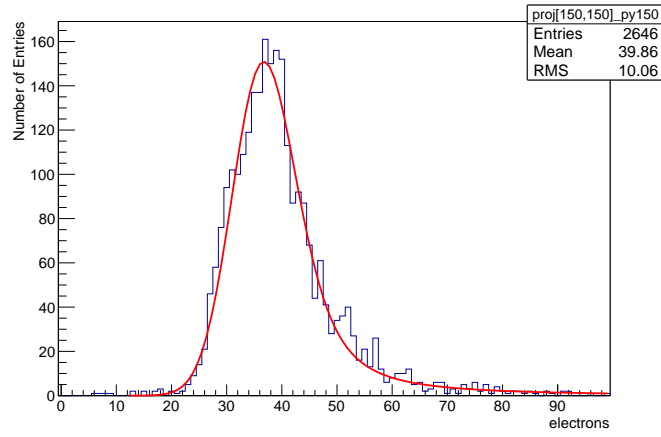


Figure 6.5.: Histogram of a sensor-wide signal to noise distribution with a Landau-Gauss fit.

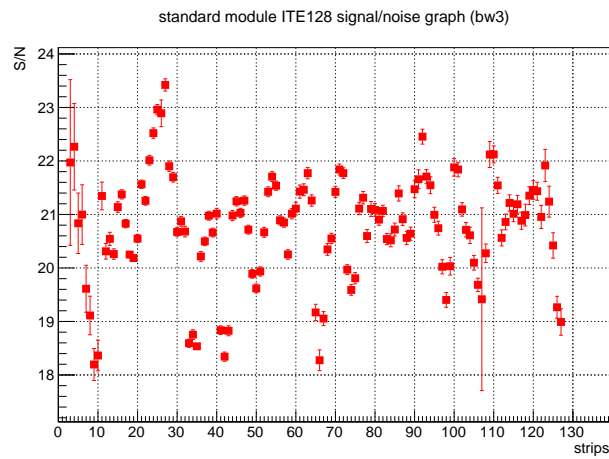


Figure 6.6.: Plot of a strip-wise signal to noise distribution.

## 6.3. Development Process

The first steps were to identify the demands on the new software and resulted in following key requirements:

- Flexibility: Analysis of modules with special geometries and layouts (e.g. non-linear connections between strips and APV25 read-out chips).
- Extensibility: Easing the addition of new functionalities.
- Architecture Independence: Compatibility with x86\_64 or i686 system architectures.
- Linux based: Ability to run on multi core Linux based systems.
- Open source: Full control over every algorithm and functions.

Those requirements are in complete contrast to the specifications of the previously used Software Analysis Framework called "APVDAQ Analysis" which was developed on MS Windows based systems.

To fulfill those demands it was decided to base "HAT" on C++ and the CERN data analysis framework ROOT [33].

After designing the overall concept of the new software, the first steps towards implementing the new framework were to identify the algorithms in the old procedural software and porting them to classes in object oriented C++ to be more flexible. This was followed by the implementation of the improved features and specifications of the new framework. The proprietary, closed source functions of LabWindows which were used in the APVDAQ Software have been reimplemented as well. All hard-coded data values of the APVDAQ Analysis were reimplemented so that they are changeable at runtime. If applicable the ANSI C data types were altered to fit the C++ style and redefined in separate headers for convenience.

### 6.3.1. Flexibility - The Virtual Frontend Chip (VFC)

As the APVDAQ Analysis was not designed to handle more complex sensor read-out geometries the smallest logical item it uses is a functional representation of the APV25 chip. This restriction fixes channel order and number which prohibits the flexible processing of data. To utilise the key advantage of dynamic software over comparably unflexible hardware a novel concept was introduced in HAT, namely the Virtual Frontend Chip (VFC). In contrast to the APV25 this virtual chip allows a complete customisation of the channel order and number. This eases the mapping of the real sensor geometry to its representation in the software.

### 6.3.2. Extensibility - The Plugin System

The plugin system is based on a common object-oriented creational design pattern for software called "factory method". The concept provides a way to encapsulate a group of individual objects without specifying the exact class of the objects by defining an interface for creating an object and let the classes that implements the interface decide which class to instantiate. In short a factory is an object for creating other objects.

The interface used for the classes of HAT has two methods:

- `configure()`: This is where all the configuration of the class takes place (Data from the configuration files is processed.).
- `analyse()`: Here resides the functional core of each class.

There are two distinct types of classes, the analysers and the configuration file readers. Both are handled separately by the plugin system according to the parameters in the main configuration file of type `.hat`. As long as each newly introduced class (e.g. functionality or configuration file handling) uses the above mentioned interface it can be incorporated easily into HAT using this plugin system.

### 6.3.3. Architecture Independence

Regarding the `x86_64` or `i686` system architectures there are differences in how many bits are allocated to certain data types, the so called data width (see table 6.1), which leads to problems if reading binary files from one platform on the other. As the APVDAQ software is running on an `i686` system, the produced binary data files were inaccessible on a `x86_64` based architecture. To account for that, an extension (`stdint.h`), introduced in the new C++11 standard, was used which forces data types to be of a well defined size, therefore enabling the readability of binary data produced on varying system architectures.

	32 bit	64 bit
Integer	4 bytes	8 bytes
Pointer types	4 bytes	8 bytes

Table 6.1.: Difference in data width regarding 32 bit and 64 bit system architectures.

## 6.4. Proof of Concept

To test the functionality of the new framework, raw data from standard and special geometry sensors were processed with HAT. Testing the consistency of the new framework, the results from the standard modules were compared to the ones of the APVDAQ Analysis (see chapter 6.4.1). To prove the overall concept of the refurbished software, non standard geometry sensors from Centro Nacional de Microelectrónica of Spain (CNM) were analysed. The results were then compared to the output of a well known software which is used at the test area of CERN (see chapter 6.4.2).

### 6.4.1. Standard Modules - Consistency Test

The standard geometry sensors used for the consistency test were produced by ITE Warsaw. They have 128 AC coupled strips with polysilicon resistor biasing specified at  $10\text{ M}\Omega$ . The strips are  $40.1\text{ mm}$  long and  $20\text{ }\mu\text{m}$  wide with a pitch of  $80\text{ }\mu\text{m}$ . The metal overhang is  $5\text{ }\mu\text{m}$  at each side and the strip area is surrounded by a bias and a guard ring with an asymmetric metal overhang. A  $500\text{ }\mu\text{m}$  wide  $n+$  implant protects the edge of the sensor. In figure 6.7 the design of the sensor is depicted.

After feeding the data to the APVDAQ Analysis and HAT a signal to noise plot was calculated by fitting the histogram of the signal and noise ratio of each strip with a gauss-landau convoluted

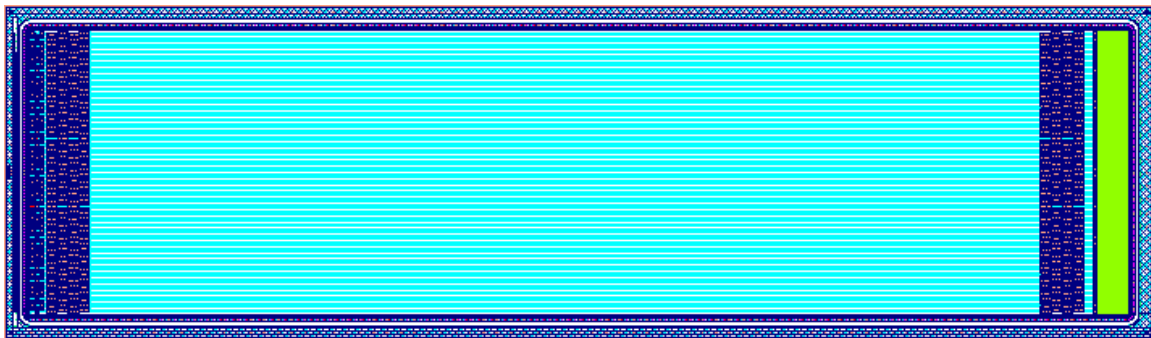


Figure 6.7.: The design of the standard sensor.

distribution function (for details see chapter 6.2.2). In figure 6.8 it can be seen that the results yielded by HAT are sufficiently consistent with the ones of the APVDAQ Analysis.

### 6.4.2. CNM Modules - Concept Test

The CNM modules of interest are 2D position-sensitive silicon strip sensor modules which gain their functionality by a special routing between the strips and the read-out chip (the module can be seen in figure 6.9). The prototype consists of 384  $p^+$  strips ( $20 \mu m$  wide) with a pitch of  $80 \mu m$  on a  $285 \mu m$  thick n-type substrate. The resistive electrodes have a total length of  $2 cm$  with linear resistance  $R/\mu m = 12.2 \Omega/\mu m$ . The prototype is constructed as such that every single strip is connected to two read-out channels. One channel is connected to the chip facing end of the strip the next one to the rear side of the strip (see figure 6.10). This allows the charge, generated by an incidence particle, to be measured on both ends of the strips. The idea of this special configuration is to be able to distinguish the location of the hit along the strip merely by measuring the charge distribution on the strip. The strip acts as voltage divider. Depending where the charge is generated, the different lengths of the strip, in regard to the read-out chip, create different resistivities. The signal is distributed correspondingly. So if the strip is hit more at the upper position a bigger amount of the charge is measured on the read-out channel on the rear side and vice versa. For a more detailed description of the concept see [36].

After designing the plugins for this special module the analysed data was used to depict the actual beam profile (gained by the CERN software) only using the information from the sensor. The 2D hitmap was produced by plotting the Center of Gravity (CoG) (see equation 7.3) of the cluster signal of each hit against the ratio of the normalised raw signal  $S_{nrs}$  (yielded by both readout channels) of the corresponding strip.

$$S_{nrs} = \frac{S_u}{S_u + S_l}, \quad (6.3)$$

where  $S_u$  is the raw signal measured at the upper read-out chip and  $S_l$  the raw signal on the lower chip. As can be seen in figure 6.11 the results nicely reproduce the beam profile measured by the wire chambers of the beam line instrumentation and prove the modularity and flexibility of HAT.

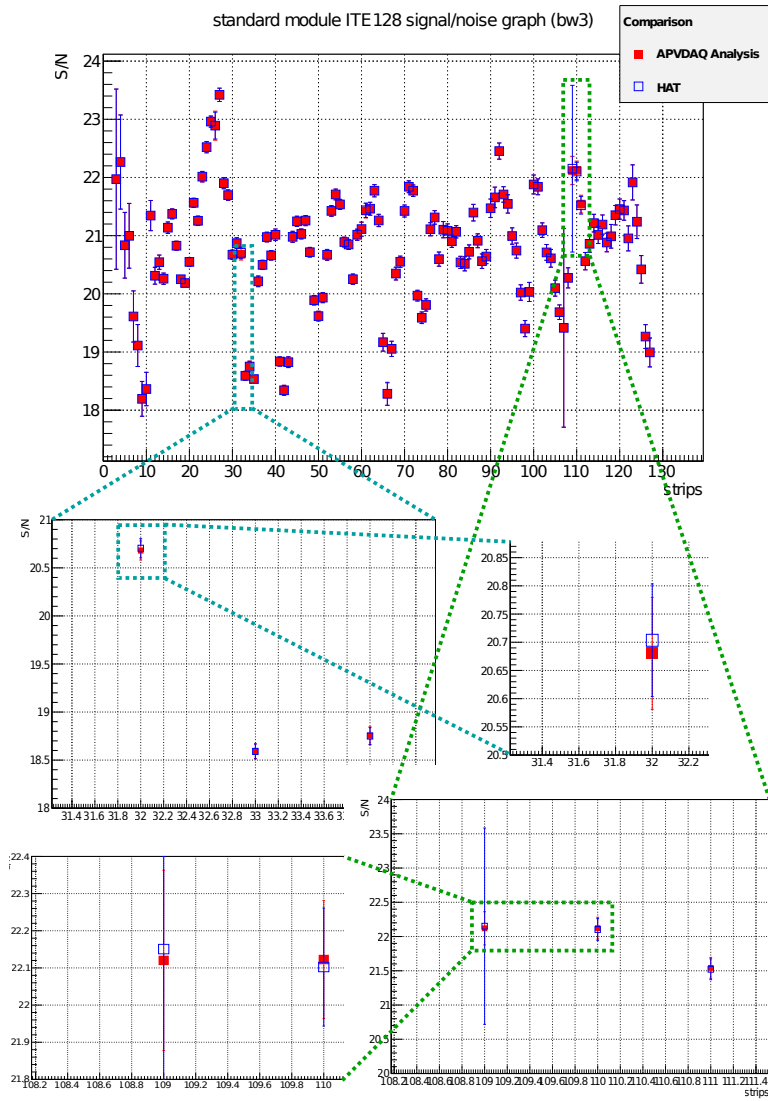


Figure 6.8.: Comparison of the S/N ratio gained by the APVDAQ Analysis and HAT.





Figure 6.9.: The CNM 2D position-sensitive module.

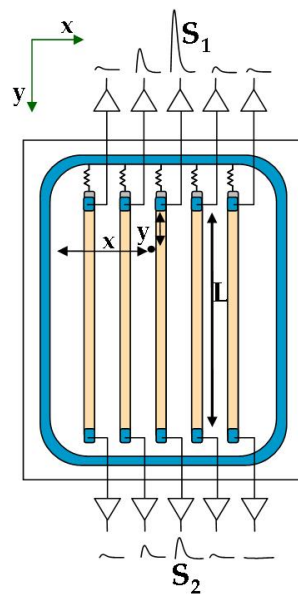


Figure 6.10.: The CNM 2D position-sensitive chip's readout logic. [36]

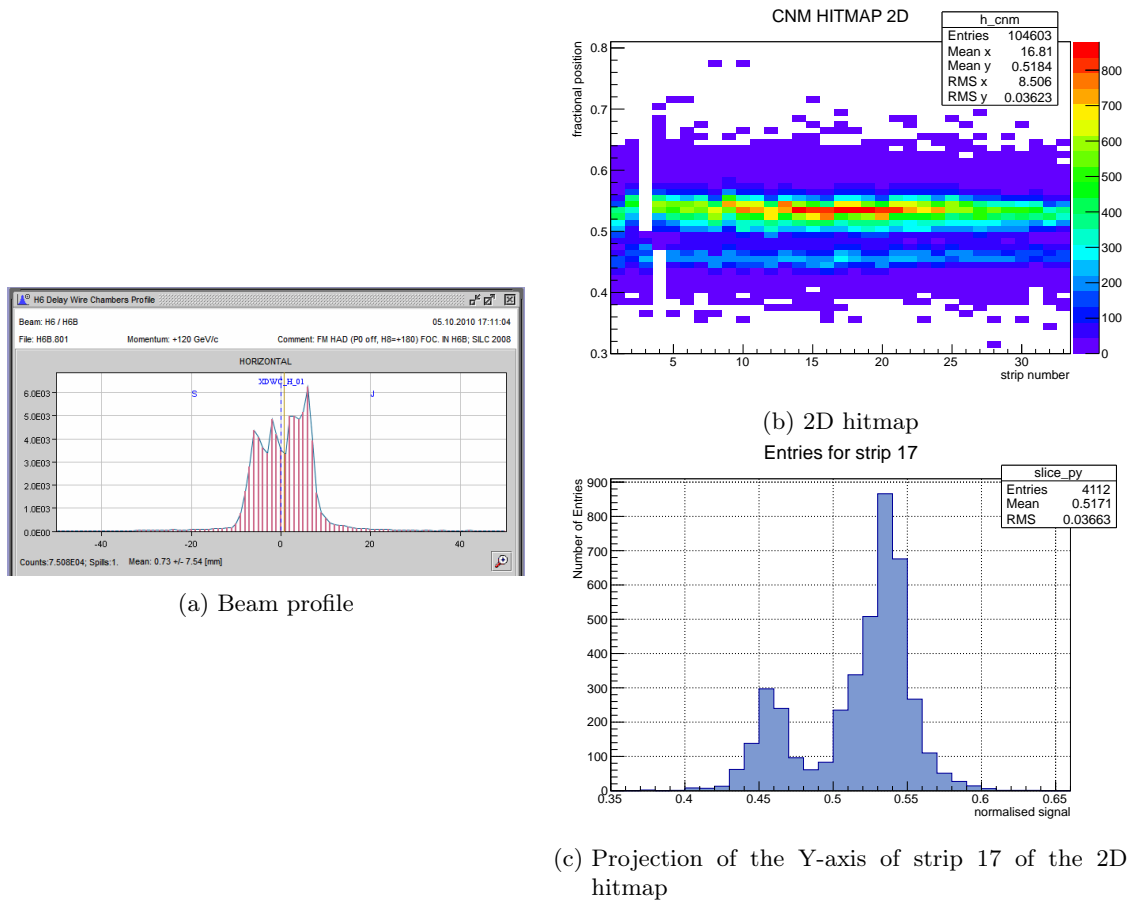


Figure 6.11.: Comparison between the actual beam profile (a) and profile generated by HAT (b,c).

# 7. Data Analysis & Results

## 7.1. Basic Sensor Properties

### 7.1.1. Signal & Noise

As described in chapter 4.3, the total noise has various sources emanating from the sensor as well as from the DAQ system. The signal depends on the material, the thickness and the depleted volume of the sensor.

In figure 7.1 the noise for every strip of module 0 and module 1 is depicted. Looking at the

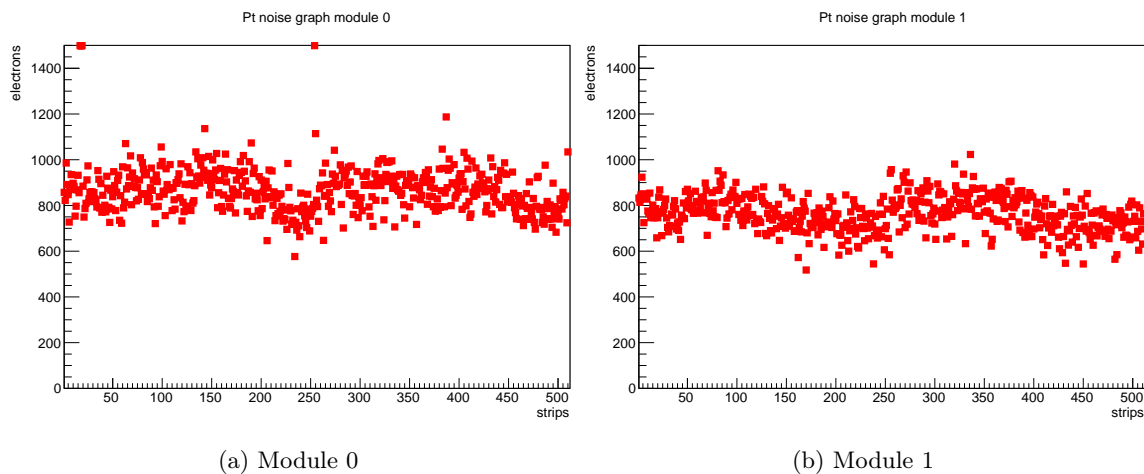


Figure 7.1.: Noise of strips. Strip 1 to 256 represent the upper sensor plane and 257 to 512 the lower one.

noise values it can be seen that module 0 has some bad strips. The overall noise is well within the specifications for this sensors.

The function 4.6 describing the energy loss distribution mentioned in chapter 4.1.3 can be used to determine the most probable signal and S/N ratio. To deal with the deviation of the signal from the Landau distribution it is convoluted with a Gaussian (the algorithms used can be seen in appendix A). All fits of the signal distribution henceforth use this approach. The signal used for the plots is the cluster signal  $S_{CLUSTER}$  and the noise the cluster noise  $N_{CLUSTER}$ . Both are determined corresponding to 6.2.1 and from now on defined as  $S$  and  $N$ , respectively.

In figure 7.2 the histogram of the signal distributions is plotted for both sensors. The sensor performs nicely. The shape of the signals for the different clusterwidths follows a landau-gauss distribution.

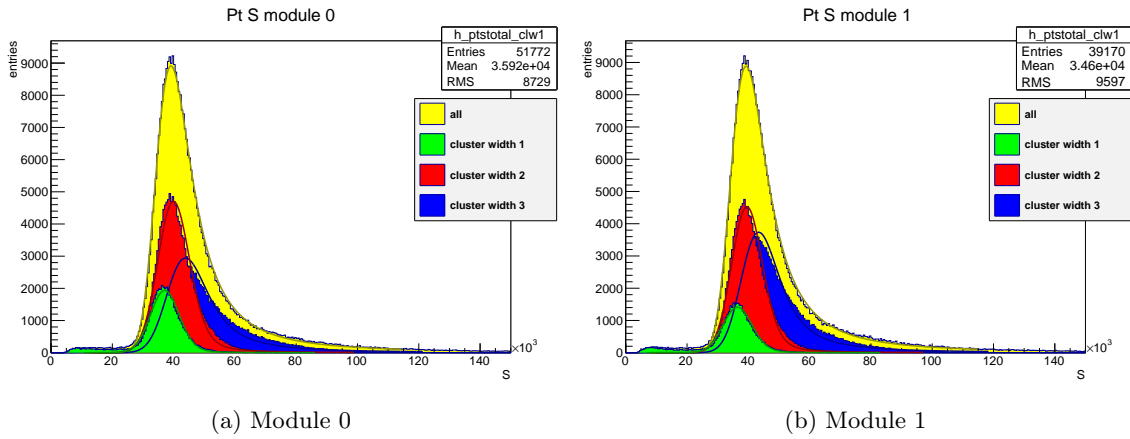


Figure 7.2.: The total signal distribution for various cluster widths, fitted with a landau-gauss function.

Plots of the S/N ratio for both modules can be seen in figure 7.3. The distributions are again landau-gauss shaped.

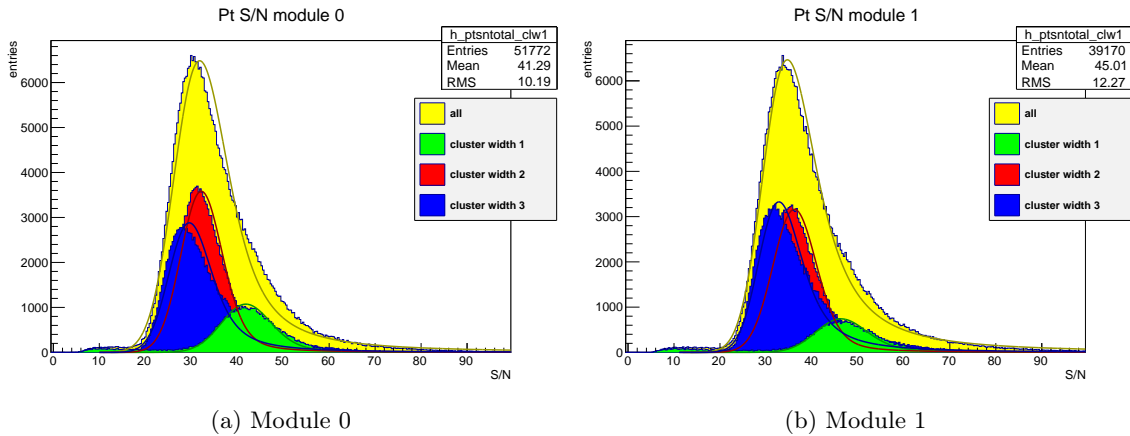


Figure 7.3.: The total S/N distribution for various cluster widths, fitted with a landau-gauss function.

The most probable S/N value over all strips of module 0 is 31 and 35 for module 1. This is within the expected values as indicated in [37].

The most probable S/N value can also be plotted for each cluster width separately (see figure 7.4a). It can be seen that the S/N ratio decreases up to a cluster width of 3 and raises afterwards. In contrast figure 7.4b shows that the signal is steadily increasing for growing cluster widths. This diverging behaviour can be explained following the definition of the cluster signal and the cluster noise. For growing cluster widths the signal is spread over more and more strips. The noise is calculated via the square sum of the constant noise of the strips in the cluster. The cluster noise is getting less and less influence. The signal is more and more dominated by high energetic  $\delta$ -electrons (see chapter 4.1.3).

In figure 7.5 the clusterwidth probability is shown for both modules at incident angle 0. It nicely depicts the fact that even a perpendicular beam triggers cluster sizes bigger than one. This happens

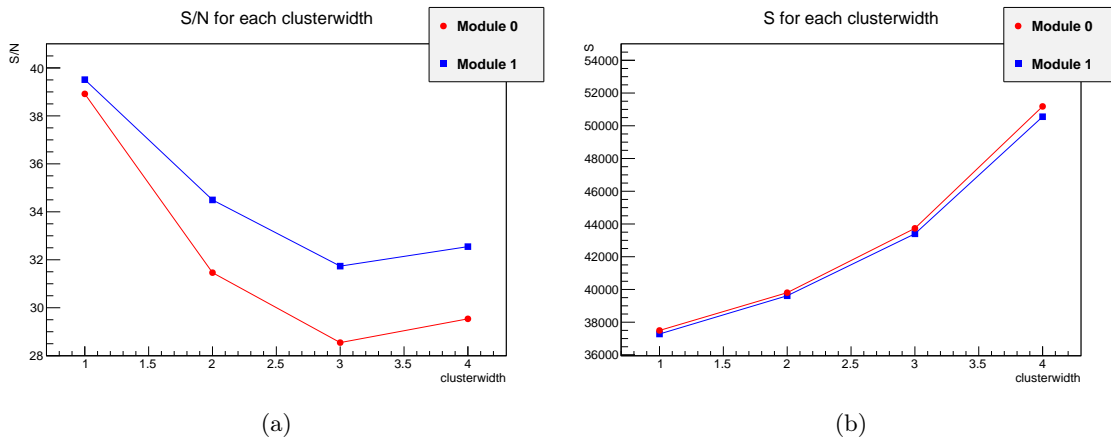


Figure 7.4.: S/N ratio (a) and signal (b) for different cluster widths.

because of the spread of the charge cloud in the material over time due to diffusion. The size of the root mean square after a drift time  $t$  is given by:

$$\sigma_D = \sqrt{2Dt}, \quad (7.1)$$

with  $D$  being the diffusion coefficient, defined as:

$$D = \frac{kT}{e} \mu, \quad (7.2)$$

where  $k$  is the Boltzmann constant,  $T$  the temperature,  $e$  the elementary charge and  $\mu$  the charge carrier mobility. This means that the signal can spread over more strips. Also the change in probability for increasing angles are depicted. It clearly indicates that the cluster width is increasing with growing incident angle.

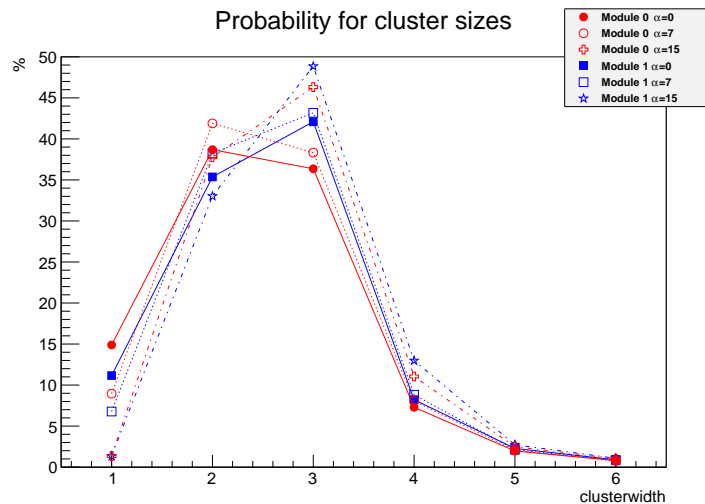


Figure 7.5.: Cluster width probability.

Regarding the angle dependency figure 7.6 indicates that the S/N ratio is decreasing slightly for higher angles. In contrast to the ratio for the highest strip in the cluster (figure 7.7 ) which decreases more profoundly. This could be a problem for strongly inclined beams as the strips in a cluster fall below the neighbouring threshold which leads to cluster splitting thereby distorting the measurement.

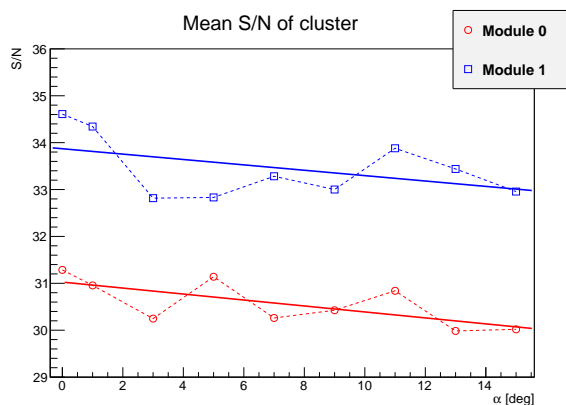


Figure 7.6.: S/N ratio for different incident angles. To depict the tendency the measured data is fitted with a linear function (continuous line).

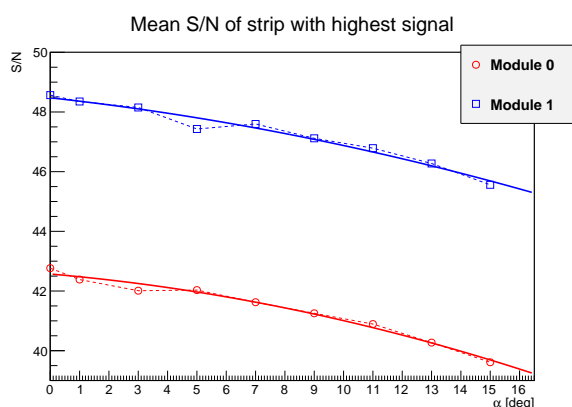


Figure 7.7.: S/N ratio of strip with highest signal in cluster. To depict the tendency the measured data is fitted polynomially (continuous line).

### 7.1.2. Charge Sharing & Capacitive Coupling

One aspect for good spatial resolution of silicon strip sensors is the ability to share charge between strips. The distribution of the charge allows to discern the more precise position of the particle hit. This can be achieved by using certain algorithms to determine the charge barycenter, namely

$\eta$ -algorithms. The one used to analyse the data in this thesis is called Center of Gravity position finding algorithm (CoG PFA) [38]. It is based on the following formula:

$$x_{cog} = \frac{\sum_{i=0}^l S_i x_i}{\sum_{i=0}^l S_i}, \quad (7.3)$$

where  $x_i$  is the position of the  $i$ th strip included in the cluster and  $S_i$  the signal on that strip. Improving position resolution is only possible if there are cluster widths greater than 1. The best resolution that can be achieved if the charge is collected by only one strip, on a sensor with read-out pitch  $p$ , is [38]:

$$\sigma_x \approx \frac{p}{\sqrt{12}} \quad (7.4)$$

In figure 7.8a the CoG distribution for perpendicular incident angle is depicted for cluster widths from 1 to 4. It can be seen that it is highly non-linear. This indicates that an over proportional amount of charge is collected by the strip nearer to the hit. Charge sharing happens in a very narrow area between the strips with a size of the RMS (see equation 7.1) of the charge cloud. Assuming linear charge sharing the CoG-positions should be uniformly distributed. This can be seen in figure 7.8c for cluster width 2 also indicating that the spatial resolution improving with higher incident angles.

At steep angles the capacitive coupling between strips becomes more pronounced compared to charge sharing. Capacitive coupling is when a fixed fraction of the signal collected by a strip is transferred to the neighbour. This happens due to electronics coupling. The amount of capacitive coupling can also be seen nicely in the  $\eta$ -distributions 7.8, especially for cluster width 2, where the peaks are shifted towards the middle and are not exactly at 0 and 1. The width of the peaks is determined by fluctuations due to noise. Figure 7.9 marks the different areas of the distribution for better understanding.

To get an estimate of the value for capacitive coupling the mean signal of neighbouring strips and the cluster's seed strip is well qualified [39]. It resembles the eta function for two strip clusters but uses both neighbouring strips. Taking into account only the strip with the highest signal would introduce a bias. This results in:

$$\eta_{symm} = \frac{S_{left} + S_{right}}{2 S_{seed}}, \quad (7.5)$$

whereas the capacitive coupling in % is represented by

$$cc = 100 \frac{\eta_{symm}}{1 + 2 \eta_{symm}}. \quad (7.6)$$

The overall capacitive coupling stays relatively constant for both sensors and varying angles.

Using the integrals  $H(x_{cog})$  of CoG-distributions, it is possible to correct the positions. It results in a uniform hit distribution and can be applied on the hit coordinates ( $x_{cog}$ ).

$$x_{corr} = |x_{cog}| + \int_0^1 \eta_{cog}(x') dx', \quad (7.7)$$

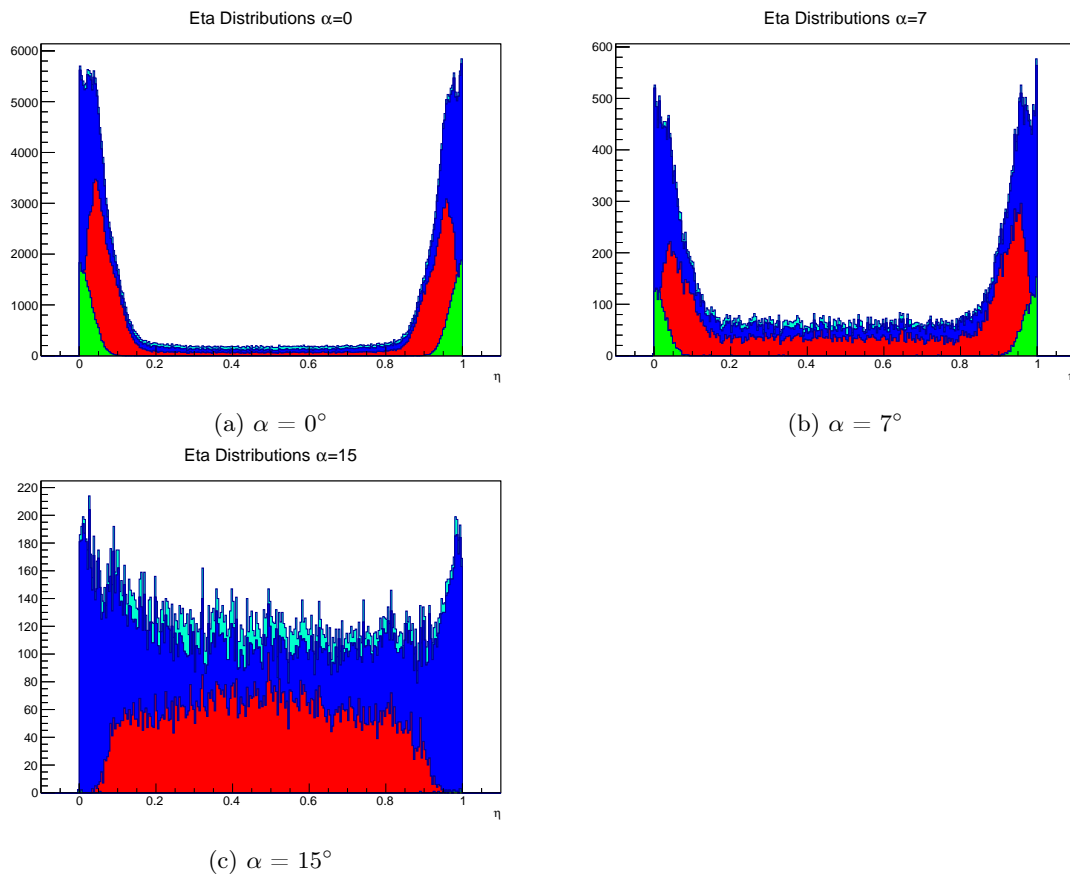


Figure 7.8.: The  $\eta$ -distributions at several incident angles for different cluster widths (green=1, red=2, darkblue=3, ...).

where  $x_{corr}$  and  $x_{cog}$  are in fractional strip numbers. This results in a stochastic correction assuming a uniform hit distribution.



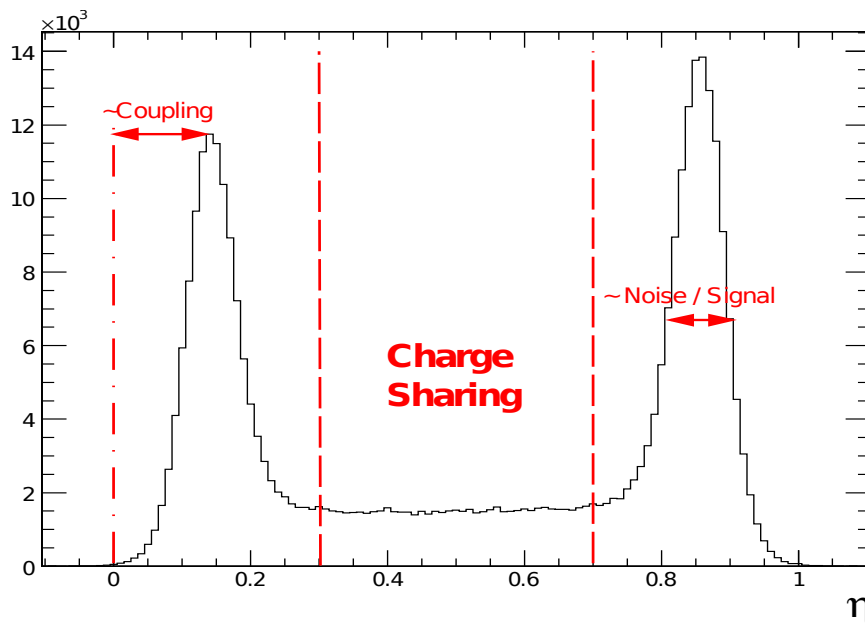


Figure 7.9.: The areas depicting the different properties. [39]

## 7.2. Angle Resolution Properties

### 7.2.1. Full Analogue Calculation Angle Resolution

In order to gain information regarding the angle resolution properties of the modules under test the strip displacement between the two sensor planes was calculated using the full clustering algorithm from chapter 6.2.1 using the eta correction as described in equation 7.7. The areas below the gauss fitted histograms are normalised to 1. The distribution at perpendicular beam can be seen in figure 7.10. It shows that the peak of gauss function is shifted to right for about  $66 \mu m$ . This displacement indicates that the strips from one plane are shifted approximately half the pitch in regard to the strips of the second plane. This was mentioned in chapter 5.2. All following plots are corrected for this value, accordingly. In figure 7.11 the distributions for all measured angles are depicted. They are gaussian as expected. It can be seen that the width of the gauss function is getting more narrow up to angle 13 and grows again afterwards. This means that the displacement can be determined more and more precisely up to mentioned angle, resulting in a better resolution. This is dependant on the read-out pitch and the thickness of the sensor and can be explained with charge sharing mentioned in chapter 7.1.2. Following [38] the best spatial resolution can be found at an angle

$$\alpha_{opt} \approx \tan^{-1}\left(\frac{p}{t}\right), \quad (7.8)$$

where  $p$  is the pitch and  $t$  the thickness of the sensor. At this angle charge sharing is almost completely linear. For the modules under test this results in an  $\alpha_{opt}$  of about 13.7 degrees. This is well reflected in the experimental data.

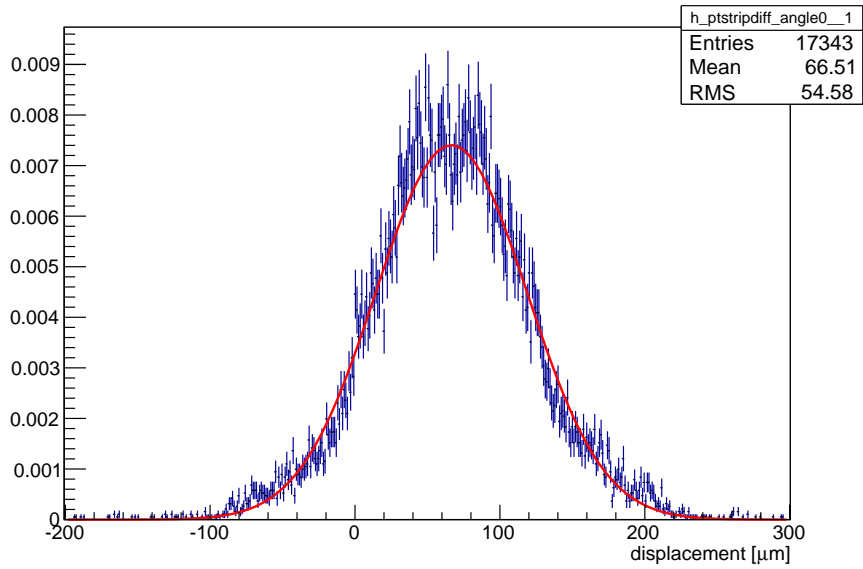


Figure 7.10.: Strip displacement at incident angle  $\alpha = 0$ .

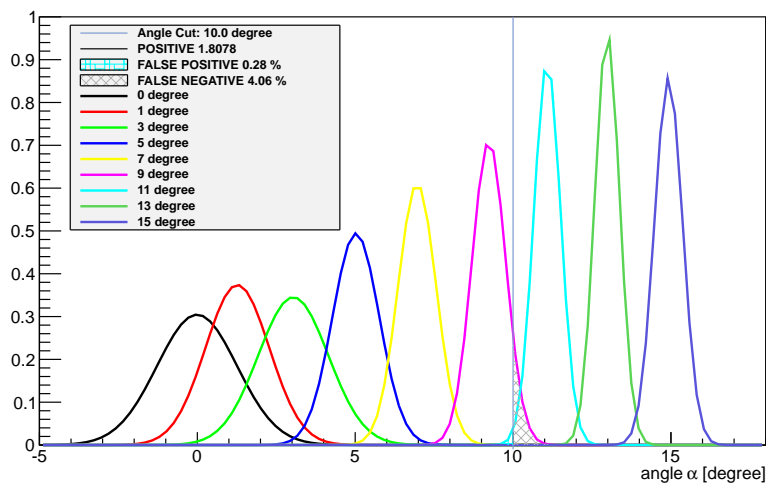


Figure 7.11.: Full analogue calculation angle distributions. The line shows an angle cut at 10 degrees.

The strip displacement can be calculated via

$$\Delta x = d \tan(\alpha) , \tag{7.9}$$

with the inter-plane separation  $d$  and the incident angle  $\alpha$ . In figure 7.12 the theoretical displacement is compared to the measured one. The experimental results are well within the boundaries of the expected values.

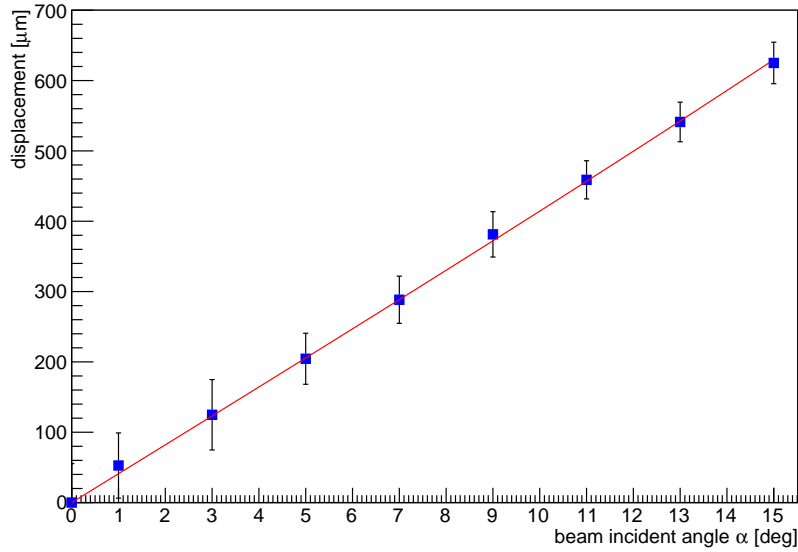


Figure 7.12.: Comparison of the measured values (blue dots) for the hit displacement to the theory (red line). The error is the root mean square.

According to [37] the mean spatial resolution  $\sigma_x$  of the sensor is about  $38 \mu\text{m}$ . An error propagation calculation for  $\Delta x = x_1 - x_2$  at angle  $\alpha = 0$  with an error of  $\sqrt{\sigma_x^2 + \sigma_x^2} \approx 54 \mu\text{m}$  shows again satisfying results compared to the standard deviation  $\sigma = 54.58 \mu\text{m}$  of the experimental data for a perpendicular beam.

In figure 7.11 an angle cut at 10 degrees was chosen which, following equation 3.3, would represent a momentum cut at approximately  $1.1 \text{ GeV}/c$  at a distance of  $30 \text{ cm}$  from the interaction point. It can be seen that the distributions overlap and therefore produce 0.28% false positive and 4.06% false negative results. Unfortunately it is not possible to derive genuine efficiencies from this data because it does not follow a realistic angle distribution as seen by the CMS detector. Figure 7.13 shows an angle cut at  $3.5^\circ$ . At a distance of  $100 \text{ cm}$  from the interaction point, this describes an energy cut of  $\approx 10 \text{ GeV}/c$ . The angle resolution is worse at steeper angles with 0.72% false positive and 13.47% false negative results.

### 7.2.2. Digital Angle Resolution

To investigate the possibility for an on-module trigger decision logic a more primitive hit finding algorithm was introduced. It uses only one fixed subevent of the six time samples described in 5.3.1. Adjacent strips are compared to a second threshold (20000 electrons) and if they exceed it, they attributed to the same cluster. The location of the passage of the particle is then estimated as the center of all strips within a cluster. The algorithm does not use any kind of  $\eta$ -distribution, nor advanced cluster finding procedures. This of course reduces precision but could be a feasible solution for implementation as an application-specific integrated circuit (ASIC). Figure 7.14 depicts the angle distributions gained with this primitive decision logic.

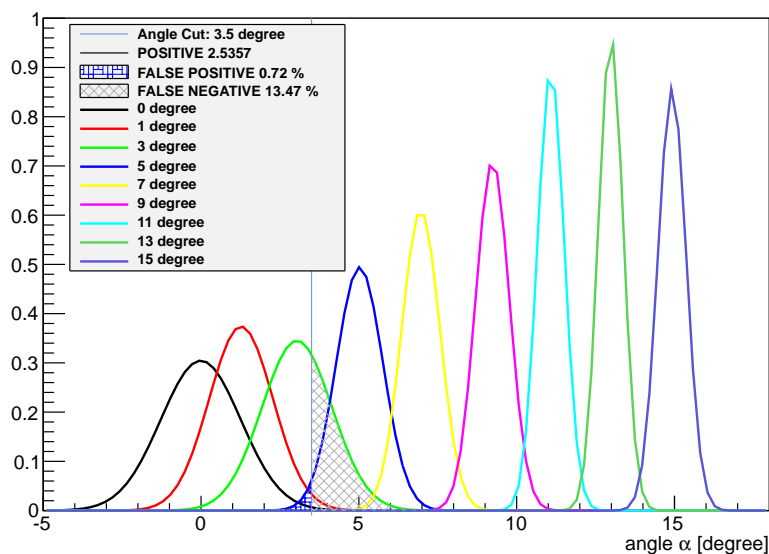


Figure 7.13.: Full analogue calculation angle distributions. The line shows an angle cut at 3.5 degrees.

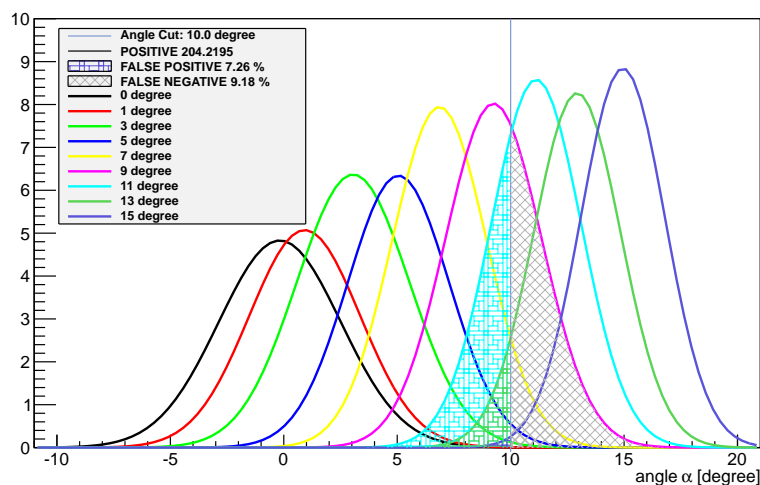


Figure 7.14.: Digital angle distributions. The line shows an angle cut at 10 degrees.

At the mentioned distance of 30 cm from the interaction point  $10^\circ$  amounts to  $\approx 1.1$  GeV/c and  $15^\circ$  corresponds to  $\approx 0.7$  GeV/c. Looking at the overlap of the distribution for  $15^\circ$  with the angle cut at  $10^\circ$ , it can be seen that even in the digital decision case a successful energy cut with a precision of about  $0.4 : 1$  GeV/c = 0.4 can be obtained.

At a distance of 100 cm  $3.5^\circ$  corresponds to  $\approx 10$  GeV/c and  $11^\circ$  represents  $\approx 3$  GeV/c. In the case of an angle cut at  $3.5^\circ$  the precision is  $7 : 10$  GeV/c  $\approx 0.7$  as can be seen in figure 7.15.

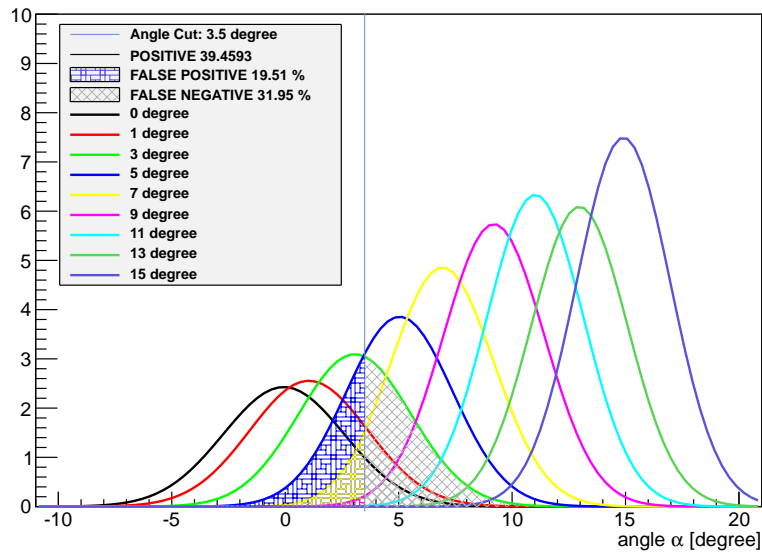


Figure 7.15.: Digital angle distributions. The line shows an angle cut at 3.5 degrees.

### 7.3. Conclusion

The efficiency of stacked track-trigger modules is highly dependant on the intrinsic properties of the sensors and the geometry of the modules, as well as their position relative to the interaction point inside the detector. In any case good spatial resolution is crucial. This could be obtained by reducing the pitch of read-out strips and introducing intermediate strips to enhance linear charge sharing [38]. Following the geometrical calculations also increasing the distance between the two sensor planes should be beneficial. This of course is only feasible up to a certain point as the communication between the sensor planes has to be maintained. Furthermore the ratio between the thickness and the strip pitch has to be considered carefully as it defines the best resolution for distinct angles. The incident angle of interest should not be too flat as this could lead to cluster splitting thereby distorting the measurement.

It has been shown that the full analogue calculation angle distributions of the given geometry are within expected values and make a fine resolution of angles possible. In case of the digital algorithm the resolution worsens but the angles are still sufficiently discriminable.

The offline analysis of the experimental data shows that stacked track-trigger modules are a suitable option for improving Level 1 trigger decisions in an upgraded CMS Tracker. It has been shown that the cut on the transverse momentum can be achieved with a very simple algorithm which could be implemented on-module level.



## 8. Acknowledgements

First and foremost, I would like to express my thanks to my supervisor *Manfred Krammer* for giving me the opportunity to work in such an interesting field and for his patience and support.

A very special thanks goes to *Marko Dragicevic* for proof-reading my thesis and listening to me endlessly, helping a lot with much appreciated input and discussions even if being fully immersed in work.

A lot of gratitude goes to *Edmund Widl* without whom the software development would have been a nearly impossible task.

Special thanks to *Thomas Bergauer, Markus Friedl, Christian Irmeler, Wolfgang Kiesenhofer* and *Manfred Valentan* for a lot of fruitful discussions and support while my work at HEPHY and the resulting thesis.

Furthermore I would like to thank all people at HEPHY for being great colleagues, always helpful and open minded.

Many thanks to the *Fachschaft Physik* at the Vienna University of Technology. I have spent plenty delightful time learning, working, discussing, playing and having some drinks there. Without this community I probably never would have managed the "perils" of studying. Special kudos to my small circle of roleplaying buddies.

Big thanks goes to all my long-time friends for being who they are and for always encouraging me.

An extra special thanks to my parents *Sigrid* and *Peter Huemer* for their financial support during my studies and for always believing in me.

Danke, dass ihr immer für mich da wart!

Finally I give all my gratitude to my beloved wife *Birgit Huemer-Pokorny* without I never would have accomplished a lot of things in my life. Your support gave me the strength and confidence I needed.

Danke für alles!





# Appendix A.

## Convolutated Landau and Gaussian Fitting Function

```
//-----  
//  
// Convolutated Landau and Gaussian Fitting Function  
//      (using ROOT's Landau and Gauss functions)  
//  
// Based on a Fortran code by R.Fruehwirth (fruehwirth@hephy.oeaw.ac.at)  
// Adapted for C++/ROOT by H.Pernegger (Heinz.Pernegger@cern.ch) and  
// Markus Friedl (Markus.Friedl@cern.ch)  
//  
// to execute this example, do:  
// root > .x langaus.C  
// or  
// root > .x langaus.C++  
//  
//-----  
  
#include "TH1.h"  
#include "TF1.h"  
#include "TROOT.h"  
#include "TStyle.h"  
#include "TMath.h"  
  
Double_t langaufun(Double_t *x, Double_t *par) {  
  
    //Fit parameters:  
    //par[0]=Width (scale) parameter of Landau density  
    //par[1]=Most Probable (MP, location) parameter of Landau density  
    //par[2]=Total area (integral -inf to inf, normalization constant)  
    //par[3]=Width (sigma) of convolutated Gaussian function  
    //  
    //In the Landau distribution (represented by the CERNLIB approximation),  
    //the maximum is located at x=-0.22278298 with the location parameter=0.  
    //This shift is corrected within this function, so that the actual  
    //maximum is identical to the MP parameter.  
  
    // Numeric constants  
    Double_t invsq2pi = 0.3989422804014;    // (2 pi)^(-1/2)  
    Double_t mpshift = -0.22278298;        // Landau maximum location  
  
    // Control constants  
    Double_t np = 100.0;                    // number of convolution steps  
    Double_t sc = 5.0;                      // convolution extends to +-sc Gaussian sigmas  
  
    // Variables  
    Double_t xx;  
    Double_t mpc;
```

```

Double_t fland;
Double_t sum = 0.0;
Double_t xlow,xupp;
Double_t step;
Double_t i;

// MP shift correction
mpc = par[1] - mpshift * par[0];

// Range of convolution integral
xlow = x[0] - sc * par[3];
xupp = x[0] + sc * par[3];

step = (xupp-xlow) / np;

// Convolution integral of Landau and Gaussian by sum
for(i=1.0; i<=np/2; i++) {
    xx = xlow + (i-.5) * step;
    fland = TMath::Landau(xx,mpc,par[0]) / par[0];
    sum += fland * TMath::Gaus(x[0],xx,par[3]);

    xx = xupp - (i-.5) * step;
    fland = TMath::Landau(xx,mpc,par[0]) / par[0];
    sum += fland * TMath::Gaus(x[0],xx,par[3]);
}

return (par[2] * step * sum * invsq2pi / par[3]);
}

TF1 *languafit(TH1F *his, Double_t *fitrange, Double_t *startvalues, Double_t *parlimitslo,
Double_t *parlimitshi, Double_t *fitparams, Double_t *fiterrors, Double_t *ChiSqr, Int_t *NDF)
{
// Once again, here are the Landau * Gaussian parameters:
// par[0]=Width (scale) parameter of Landau density
// par[1]=Most Probable (MP, location) parameter of Landau density
// par[2]=Total area (integral -inf to inf, normalization constant)
// par[3]=Width (sigma) of convoluted Gaussian function
//
// Variables for languafit call:
// his          histogram to fit
// fitrange[2]  lo and hi boundaries of fit range
// startvalues[4] reasonable start values for the fit
// parlimitslo[4] lower parameter limits
// parlimitshi[4] upper parameter limits
// fitparams[4] returns the final fit parameters
// fiterrors[4] returns the final fit errors
// ChiSqr      returns the chi square
// NDF         returns ndf

Int_t i;
Char_t FunName[100];

sprintf(FunName,"Fitfcn_%s",his->GetName());

TF1 *ffitold = (TF1*)gROOT->GetListOfFunctions()->FindObject(FunName);
if (ffitold) delete ffitold;

TF1 *ffit = new TF1(FunName,languafun,fitrange[0],fitrange[1],4);
ffit->SetParameters(startvalues);
ffit->SetParNames("Width","MP","Area","GSigma");

```

---

```

for (i=0; i<4; i++) {
    ffit->SetParLimits(i, parlimitslo[i], parlimitshi[i]);
}

his->Fit(FunName,"RBO"); // fit within specified range, use ParLimits, do not plot

ffit->GetParameters(fitparams); // obtain fit parameters
for (i=0; i<4; i++) {
    fiterrors[i] = ffit->GetParError(i); // obtain fit parameter errors
}
ChiSqr[0] = ffit->GetChisquare(); // obtain chi^2
NDF[0] = ffit->GetNDF(); // obtain ndf

return (ffit); // return fit function
}

Int_t langaupro(Double_t *params, Double_t &maxx, Double_t &FWHM) {

    // Seaches for the location (x value) at the maximum of the
    // Landau-Gaussian convolute and its full width at half-maximum.
    //
    // The search is probably not very efficient, but it's a first try.

    Double_t p,x,fy,fxr,fxl;
    Double_t step;
    Double_t l,lold;
    Int_t i = 0;
    Int_t MAXCALLS = 10000;

    // Search for maximum

    p = params[1] - 0.1 * params[0];
    step = 0.05 * params[0];
    lold = -2.0;
    l = -1.0;

    while ( ( l != lold) && ( i < MAXCALLS) ) {
        i++;

        lold = l;
        x = p + step;
        l = langaufun(&x,params);

        if ( l < lold)
            step = -step/10;

        p += step;
    }

    if ( i == MAXCALLS)
        return (-1);

    maxx = x;

    fy = l/2;

    // Search for right x location of fy

    p = maxx + params[0];

```

```

step = params[0];
lold = -2.0;
l = -1e300;
i = 0;

while ( ( l != lold) && ( i < MAXCALLS) ) {
    i++;

    lold = l;
    x = p + step;
    l = TMath::Abs(langaufun(&x,params) - fy);

    if ( l > lold)
        step = -step/10;

    p += step;
}

if ( i == MAXCALLS)
    return (-2);

fxr = x;

// Search for left x location of fy

p = maxx - 0.5 * params[0];
step = -params[0];
lold = -2.0;
l = -1e300;
i = 0;

while ( ( l != lold) && ( i < MAXCALLS) ) {
    i++;

    lold = l;
    x = p + step;
    l = TMath::Abs(langaufun(&x,params) - fy);

    if ( l > lold)
        step = -step/10;

    p += step;
}

if ( i == MAXCALLS)
    return (-3);

fxl = x;

FWHM = fxr - fxl;
return (0);
}

void langaus() {
    // Fill Histogram
    Int_t data[100] = {0,0,0,0,0,0,2,6,11,18,18,55,90,141,255,323,454,563,681,
        737,821,796,832,720,637,558,519,460,357,291,279,241,212,
        153,164,139,106,95,91,76,80,80,59,58,51,30,49,23,35,28,23,
        22,27,27,24,20,16,17,14,20,12,12,13,10,17,7,6,12,6,12,4,
        9,9,10,3,4,5,2,4,1,5,5,1,7,1,6,3,3,3,4,5,4,4,2,2,7,2,4};
    TH1F *hSNR = new TH1F("snr","Signal-to-noise",400,0,400);
}

```

---

```

for (Int_t i=0; i<100; i++) hSNR->Fill(i,data[i]);

// Fitting SNR histo
printf("Fitting...\n");

// Setting fit range and start values
Double_t fr[2];
Double_t sv[4], pllo[4], plhi[4], fp[4], fpe[4];
fr[0]=0.3*hSNR->GetMean();
fr[1]=3.0*hSNR->GetMean();

pllo[0]=0.5; pllo[1]=5.0; pllo[2]=1.0; pllo[3]=0.4;
plhi[0]=5.0; plhi[1]=50.0; plhi[2]=1000000.0; plhi[3]=5.0;
sv[0]=1.8; sv[1]=20.0; sv[2]=50000.0; sv[3]=3.0;

Double_t chisqr;
Int_t    ndf;
TF1 *fitsnr = langaufit(hSNR,fr,sv,pllo,plhi,fp,fpe,&chisqr,&ndf);

Double_t SNRPeak, SNRFWHM;
langapro(fp,SNRPeak,SNRFWHM);

printf("Fitting done\nPlotting results...\n");

// Global style settings
gStyle->SetOptStat(1111);
gStyle->SetOptFit(111);
gStyle->SetLabelSize(0.03,"x");
gStyle->SetLabelSize(0.03,"y");

hSNR->GetXaxis()->SetRange(0,70);
hSNR->Draw();
fitsnr->Draw("lsame");
}

```



# Bibliography

- [1] G. Rajasekaran. “Are Neutrinos Majorana Particles?” In: *arXiv.org* physics.pop-ph (2008), all. eprint: 0803.4387. URL: <http://arxiv.org/abs/0803.4387v1>.
- [2] InverseHypercube. *Standard Model of Elementary Particles*. July 2012. URL: [http://upload.wikimedia.org/wikipedia/commons/archive/0/00/20130221160757!Standard\\_Model\\_of\\_Elementary\\_Particles.svg](http://upload.wikimedia.org/wikipedia/commons/archive/0/00/20130221160757!Standard_Model_of_Elementary_Particles.svg).
- [3] Steven Weinberg. “A Model of Leptons”. In: *Phys.Rev.Lett.* 19 (1967), pp. 1264–1266. DOI: 10.1103/PhysRevLett.19.1264.
- [4] P.W. Higgs. “Spontaneous Symmetry Breakdown without Massless Bosons”. In: *Phys.Rev.* 145 (1966), pp. 1156–1163. DOI: 10.1103/PhysRev.145.1156.
- [5] Lev Okun. “Mirror particles and mirror matter: 50 years of speculation and search”. In: *arXiv.org* hep-ph (2006), all. URL: <http://arxiv.org/abs/hep-ph/0606202v2>.
- [6] U.W. Heinz. “Concepts of Heavy-Ion Physics”. In: *arXiv.org* hep-ph (2004), all. URL: <http://arxiv.org/abs/hep-ph/0407360v1>.
- [7] P. Bryant L. Evans. “LHC Machine”. In: *JINST* 3 (2008), all. DOI: 10.1088/1748-0221/3/08/S08001. URL: [http://iopscience.iop.org/1748-0221/3/08/S08001/pdf/1748-0221\\_3\\_08\\_S08001.pdf](http://iopscience.iop.org/1748-0221/3/08/S08001/pdf/1748-0221_3_08_S08001.pdf).
- [8] T. Junk, J. Hays, and W. Fisher. “Combined CDF and D0 Upper Limits on Standard Model Higgs Boson Production with up to 8.6 fb<sup>-1</sup> of Data”. In: *arXiv.org* hep-ex (2011), all. URL: <http://arxiv.org/abs/1107.5518>.
- [9] M.W. Gruenewald. “Precision Electroweak Measurements and Constraints on the Standard Model”. In: *arXiv.org* hep-ex (2011), all. URL: <http://arxiv.org/abs/1012.2367>.
- [10] F. Zimmermann Y. Papaphilippou. “Estimates of Diffusion due to Long-range Beam-beam Collisions”. In: *Phys. Rev. Spec. Top. Accel. Beams* 5 (2002), p. 074001. URL: <http://prst-ab.aps.org/abstract/PRSTAB/v5/i7/e074001>.
- [11] LHC Study Group. *The Large Hadron Collider : conceptual design*. Ed. by P. Lefèvre T. S. Pettersson. CERN. Geneva, 1995. URL: <http://cdsweb.cern.ch/record/291782>.
- [12] P. Sphicas D. Froidevaux. “General-Purpose Detectors for the Large Hadron Collider”. In: *Annual Review of Nuclear and Particle Science* 56 (2006), pp. 375–440. DOI: 10.1146/annurev.nucl.54.070103.181209. URL: <http://www.annualreviews.org/doi/abs/10.1146/annurev.nucl.54.070103.181209>.
- [13] CERN. Geneva. LHC Experiments Committee. *LHCb : Technical Proposal*. CERN. Geneva, 1998. URL: <http://cdsweb.cern.ch/record/622031>.

- [14] CERN. Geneva. LHC Experiments Committee. *ALICE : Technical proposal for a Large Ion collider Experiment at the CERN LHC*. CERN. Geneva, 1995. URL: <http://cdsweb.cern.ch/record/293391>.
- [15] Tejinder S. Virdee. “Detectors at LHC”. In: *Physics Reports* 403-404 (2004), pp. 401–434. DOI: 10.1016/j.physrep.2004.08.026.
- [16] CMS Collaboration. *CMS Physics Technical Design Report Volume I : Detector Performance and Software*. Ed. by CERN. Geneva. LHC Experiments Committee ; LHCC. CERN. Geneva, 2006. URL: <http://cdsweb.cern.ch/record/922757>.
- [17] CMS Collaboration. *The CMS magnet project : Technical Design Report*. Ed. by CERN. Geneva. LHC Experiments Committee ; LHCC. CERN. Geneva, 1997. URL: <http://cdsweb.cern.ch/record/331056>.
- [18] F. Gianotti M.L. Mangano T. Virdee. “Physics potential and experimental challenges of the LHC luminosity up- grade”. In: *arXiv.org hep-ph* (2002), all. URL: <http://arxiv.org/abs/hep-ph/0204087>.
- [19] J. Kerby, P. Pfund, and R. Ostojic. *Inner Triplet Systems at IR1,2,5 and 8*. Tech. rep. FNAL, 2000. URL: [http://www-td.fnal.gov/LHC/Us1hc\\_accel\\_docs/MQXB/](http://www-td.fnal.gov/LHC/Us1hc_accel_docs/MQXB/).
- [20] G. Blair. “FP7 High Luminosity Large Hadron Collider Design Study”. Version date: 2011-07-12.
- [21] L. Arnaudon et al. *Linac4 Technical Design Report*. Ed. by M. Vretenar F. Gerigk. CERN - AB Department, 2006. URL: <http://doc.cern.ch/archive/electronic/cern/preprints/ab/ab-2006-084.pdf>.
- [22] Lombardi A. et al., eds. *End-To-End Beam Dynamics for CERN LINAC4*. 2006. URL: <http://epaper.kek.jp/abdwhb06/PAPERS/TUAY02.PDF>.
- [23] O Rossi L Brüning. *High Luminosity Large Hadron Collider A description for the European Strategy Preparatory Group*. Tech. rep. CERN-ATS-2012-236. HL LHC, 2012. URL: <http://cdsweb.cern.ch/record/1471000?ln=en>.
- [24] CMS Collaboration. *Technical Proposal for the Upgrade of the CMS detector through 2020*. Tech. rep. CERN-LHCC-2011-006. LHCC-P-004. CERN, June 2011. URL: <http://cdsweb.cern.ch/record/1355706/>.
- [25] J. Beringer et al. “Review of Particle Physics – Passage of particles through matter”. In: *Physical Review D* 86 (2012), pp. 323–338. DOI: 10.1103/PhysRevD.86.010001.
- [26] H. Bichsel. “Stragglings in thin silicon detectors”. In: *Rev. Mod. Phys.* 60 (1988), pp. 663–699. DOI: 10.1103/RevModPhys.60.663.
- [27] S. Ramo, ed. *Currents Induced by Electron Motion*. Vol. 27. Proceedings of the IRE 9. 1939. DOI: 10.1109/JRPROC.1939.228757.
- [28] F. Hartmann; T. Bergauer; J.-C. Fontaine; M. Frey; A. Furgeri; M. Krammer. “Corrosion on silicon sensors”. In: *Nuclear Inst. and Methods in Physics Research, A* 569(1) (2006), 80–83.



- 
- [29] T. Bergauer. “Design, Construction and Commissioning of the CMS Tracker at CERN and Proposed Improvements for Detectors at the Future International Linear Collider”. PhD thesis. Vienna University of Technology, 2008. URL: [http://www.hephy.at/forschung/alle/publikationen/dissertationen/?no\\_cache=1&user\\_publicationen\\_pi1\[item\]=42](http://www.hephy.at/forschung/alle/publikationen/dissertationen/?no_cache=1&user_publicationen_pi1[item]=42).
- [30] Raymond M. et al. “The CMS Tracker APV25 0.25  $\mu\text{m}$  CMOS Readout Chip”. In: *Nuclear Science Symposium Conference Record 2* (2000), pp. 113–118.
- [31] C. Irmeler. “Upgrade studies for the Belle silicon vertex detector”. MA thesis. Technische Universität Wien, 2008.
- [32] T. Haas. *A Pixel Telescope for Detector R&D for an International Linear Collider*. Tech. rep. Deutsches Elektronensynchrotron, 2006.
- [33] CERN. *ROOT, An Object-Oriented Data Analysis Framework*. URL: <http://root.cern.ch>.
- [34] C. Irmeler et al. “Efficient signal conditioning by a FIR filter for analog signal transmission over long lines”. In: *JINST* 7 (2012), p. C01082. DOI: [doi:10.1088/1748-0221/7/01/C01082](https://doi.org/10.1088/1748-0221/7/01/C01082).
- [35] Heinz Pernegger. “The Silicon Ministrip Detector of the DELPHI Very Forward Tracker”. PhD thesis. Vienna University of Technology, Feb. 1996.
- [36] D. Bassignana et al. “First investigation of a novel 2D position-sensitive semiconductor detector concept”. In: *arXiv.org physics.ins-det* (June 2011), all. eprint: 1106.5405. URL: <http://arxiv.org/abs/1106.5405>.
- [37] E. Butz. “Calibration, Alignment and Long-Term Performance of the CMS Silicon Tracking Detector”. PhD thesis. University of Hamburg, 2009.
- [38] R. Turchetta. “Spatial resolution of silicon microstrip detectors”. In: *Nuclear Inst. and Methods in Physics Research, A* 335 (1993), pp. 44–58. DOI: [10.1016/0168-9002\(93\)90255-G](https://doi.org/10.1016/0168-9002(93)90255-G).
- [39] C. Bloch. “Studies for the Commissioning of the CERN CMS Silicon Strip Tracker”. PhD thesis. Vienna University of Technology, 2007.